

**Computational Investigations of the Spectroscopy,
Vibronic Coupling, and Photo(stereo)chemistry
in Inorganic Systems**

Justyna M. Żurek

Submitted for the degree of Doctor of Philosophy (Chemistry)

Heriot-Watt University
School of Engineering and Physical Sciences

November 2011

The copyright in this thesis is owned by the author. Any quotation from the thesis or use of any of the information contained in it must acknowledge this thesis as the source of the quotation or information.

Abstract

This thesis focuses on the spectroscopy and photo-stereochemistry of relatively large closed-shell and open-shell transition metal complexes, investigated with an array of modern computational methodologies. The presence of the metal electrons/orbitals results in a greater number of low-lying excited states, and these states are vibronically coupled resulting in Jahn-Teller or pseudo-Jahn-Teller (pJT) effects, or general surface crossings. These features are very challenging to calculate but are vitally important to explain the observed behavior in such systems.

Computational investigations using the multiconfigurational CASSCF method on the pJT effect occurring in ammonia, and $\text{Mo}_2(\text{DXylF})_2(\text{O}_2\text{CCH}_3)_2(\mu_2\text{-O})_2$ complex are presented. These definitively show that in the latter case the experimentally observed structure is due to a vibronic coupling of the ground electronic state with that of a non-degenerate ${}^1\pi\delta^*$ state, resulting in a rhomboidal rather than square motif at the bimetallic centre.

The $(\text{BQA})\text{PtMe}_2\text{I}$ (BQA= bis(8-quinolinyl)amide) complex has been found to undergo unexpected *meridial* to *facial* isomerisation induced by light. The TD-DFT method was used to examine the spectroscopy of this system, and the CASSCF method was used to examine excited state relaxation pathways. The system relaxes on an excited state potential energy surface, of an essentially localised $\pi\pi^*$ excited state of the BQA ligand, and reaches a facial excited minimum that is located adjacent to a sloped conical intersection connecting the excited and ground electronic states.

Chromium (III) complexes have been investigated for many years and many aspects of their photochemistry are still not very well understood. The photochemistry of paradigm Cr (III) complexes, such as chromium oxalate $[\text{Cr}(\text{C}_2\text{O}_4)_3]^{3-}$, chromium tris-(1,3diaminopropane) $[\text{Cr}(\text{tn})_3]^{3+}$ and $\text{Cr}(\text{tn})_2(\text{CN})_2$, have been investigated using TD-DFT and CASSCF methods. Non-radiative relaxation pathways have been documented showing mechanism of both internal conversion in the quartet manifold, as well as inter-system crossing into the doublet manifold. The results explain photostereochemical features of the photo-induced racemization of $[\text{Cr}(\text{C}_2\text{O}_4)_3]^{3-}$ and the photoaquation of $[\text{Cr}(\text{tn})_3]^{3+}$ and $\text{Cr}(\text{tn})_2(\text{CN})_2$.

Acknowledgements

I would like to express my gratitude to all without whom this dissertation would not be possible.

First of all I would like to thank my supervisor Dr Martin Paterson for allowing me to join his team and guiding me through this project. His patience, enthusiasm and academic experience have been a great inspiration and were invaluable to me.

The encouragement and support of my close friends has been indispensable and I deeply appreciate their belief in me. Particularly, I would like to thank Natalia for helping me adapt in a new country and sharing important moments and Basia for always being there for me.

Working with the theoretical chemistry group of Heriot-Watt University was a pleasure and I thank them all for a wonderful atmosphere in the office, help and fruitful discussions.

I would also like to acknowledge the EPSRC for funding through grant number EP/F01709X.

Above all, I would like to thank my family and my husband Russell. With your love and support everything is achievable.

List of Papers

- [1] Żurek, J. M.; Paterson, M. J., Theoretical Study of the Pseudo-Jahn-Teller Effect in the Edge-Sharing Bioctahedral Complex $\text{Mo}_2(\text{DXylF})_2(\text{O}_2\text{CCH}_3)_2(\mu_2\text{-O})_2$, *Inorg. Chem.* **2009**, *48*, 10652–10657.
- [2] Żurek, J. M.; Paterson, M. J., Photoisomerization in a Platinum-Amido Pincer Complex: An Excited-State Reaction Pathway Controlled by Localized Ligand Photochemistry, *J. Phys. Chem. Lett.* **2010**, *1*, 1301–1306.
- [3] McKinlay, R. G.; Żurek, J. M.; Paterson, M. J., Vibronic Coupling in Inorganic Systems: Photochemistry, Conical Intersections and the Jahn-Teller and Pseudo-Jahn-Teller Effects, published in *Advances in Inorganic Chemistry - Theoretical and Computational Inorganic Chemistry* Vol. 62, **2010**, 351-390.
- [4] Żurek, J. M.; Paterson, M. J., Photoracemization and Excited State Relaxation Through Non-Adiabatic Pathways in Chromium (III) Oxalate Ions *Phys. Chem. Chem. Phys.* **2011**, *submitted*.
- [5] Żurek, J. M.; Paterson, M. J., Computational Studies on the Photochemistry of the Chromium (III) tris-1,3-diaminopropane $[\text{Cr}(\text{tn})_3]^{3+}$ Complex, the Mechanism of its Photoaquation and Formation of Photoproducts, *in preparation*.

List of Contents

CHAPTER 1 – Introduction	1
1.1. Transition metal complexes: structure, bonding, stereochemistry and applications.	3
1.2. Review of some recent work done in the area of inorganic computational photochemistry.	10
1.3. List of references.	16
CHAPTER 2 – Theoretical Background	25
2.1. The wavefunction, Schrödinger equation and Born-Oppenheimer approximation.	27
2.2. Electronic structure methods.	34
2.2.1. Hartree-Fock theory.	34
2.2.2. Basis sets.	36
2.2.3. Multi-Configurational Self Consistent Field methods – MCSCF.	38
2.2.4. Density Functional Theory (DFT).	42
2.3. Closed vs open shell configurations.	48
2.4. Potential Energy Surface (PES) crossings.	53
2.4.1. Conical intersections.	53
2.4.2. Intersystem crossings and spin-orbit coupling effects.	56
2.4.3. Jahn-Teller effects.	60
2.5. Geometry optimisations.	62
2.6. List of references.	65
CHAPTER 3 – The Pseudo-Jahn-Teller Effect in Inorganic Photochemistry	71
3.1. Ammonia.	78
3.1.1. Introduction.	78
3.1.2. Computational details.	79
3.1.3. Results and discussion.	79

3.2. The Pseudo-Jahn-Teller effect in $\text{Mo}_2(\text{DXylF})_2(\text{O}_2\text{CCH}_3)_2(\mu_2\text{-O})_2$.	83
3.2.1. Introduction.	83
3.2.2. Computational details.	87
3.2.3. Results and discussion.	87
3.3. List of references.	95
CHAPTER 4 - <i>Meridial to facial</i> photoisomerisation of the closed-shell Platinum-bis(8-quinolinyl)amido complex	99
4.1. Introduction.	100
4.2. Computational details.	101
4.3. Results and discussion.	102
4.4. List of references.	115
CHAPTER 5 - Photochemistry of Chromium Oxalate $[\text{Cr}(\text{C}_2\text{O}_4)_3]^{3-}$	119
5.1. Introduction.	122
5.2. Computational details.	125
5.3. Results and discussion.	128
5.4. List of references.	140
CHAPTER 6 - Photochemistry, spectroscopy and photoproducts of the aquation reaction of Chromium (III) tris-1,3-diaminopropane $[\text{Cr}(\text{tn})_3]^{3+}$ complex and its derivative <i>trans</i>-$[\text{Cr}(\text{tn})_2(\text{CN})_2]^+$	142
6.1. Photochemistry and photoaquation of $[\text{Cr}(\text{tn})_3]^{3+}$ complex.	144
6.1.1. Computational details.	146
6.1.2. Results and discussion.	150
6.2. Photochemistry and photoaquation of <i>trans</i> - $[\text{Cr}(\text{tn})_2(\text{CN})_2]^+$ complex.	156
6.2.1. Computational details.	157
6.2.2. Results and discussion.	159
6.3. List of references.	162
CHAPTER 7 – Conclusions	164

CHAPTER 1

Introduction

The electronically excited states of molecules are at the heart of photochemistry. The most important questions, which arise here are which excited electronic states are responsible for desired/observed outcomes and what is the chemical nature of these states? To answer such questions one has to be familiar with spectroscopic concepts such as absorption or emission by an atom or molecule. Knowing (and characterising) the electronic absorption spectrum of molecules is essential for the determination of the electronic configurations of photoactive excited states.

Photochemical processes may often occur on a very short timescale. Such reactions fall in the domain of ultrafast chemistry (i.e., chemistry occurring on a sub-picosecond timescale). Experimentally such processes are investigated by ultrafast (picosecond and femtosecond) spectroscopy. These experiments make it possible to follow chemical reactions in “real time” and offer unprecedented insight into the mechanisms of light-induced chemistry. There are still many unknowns and many unanswered questions in this field, mainly due to the complexity and intricacies of the chemistry being explored and the challenges in analysing complex experimental data sets. Since the growth of computational chemistry methods (in particular for excited electronic states) in the last decade or so, coupled with the concomitant development of hardware, it is now possible to explain and rationalise more and more experimental observations of complex photochemistry. Indeed it is now widely accepted that experiment and theory should go hand-in-hand in attempting to explain such complex phenomena. One of the primary subjects of investigations within this growing field of theoretical photochemistry has been biological systems, and it is now possible to describe some aspects of their photochemistry with very high accuracy (e.g. structure and dynamics) [1-7]. From a fundamental point of view there have been far fewer computational studies on light induced inorganic chemistry than their organic counterparts. The photochemistry of inorganic systems, especially where transition metals are involved, is very challenging and difficult to investigate. Computational difficulties are encountered often due to the sheer system size, which sometimes precludes highly accurate computation. Presence of metal electrons/orbitals results in greater density of excited electronic states, which can also be of different spin states. This can further complicate the whole picture and be very hard to model and treat computationally. It should be noted that this greater number of close-lying electronic states almost guarantees the importance of vibronic coupling effects, thus inorganic photochemistry will have many examples of ultrafast

photochemistry. Methods that are needed to treat those effects require significant computer resources. Nevertheless, in recent years there have been significant studies that have highlighted the importance of a computational rationalisation of experimental results in inorganic photochemistry [8-12].

For organic molecules usually small numbers of states are needed to describe the observed photochemistry of the system. However, as modern studies show, vibronic coupling effects are also ubiquitous in organic photochemistry [13-15]. The concept of vibronic coupling will be presented later in the theory chapter of this work.

Understanding the photochemistry of transition metal complexes is important because of the wide applications of these systems. They are very good catalysts for many reactions and industrial processes [16-23], C-H bond activation [24, 25], they are widely used in biochemistry [26, 27], and cell biology [28], in drug design [29], especially as anticancer agents [30-33], in semiconductor technology [34, 35], photonic and optoelectronic devices [36, 37] such as organic light emitting diodes (OLED) [38, 39] and many other areas of science and technology.

A general review of some recent experimental and theoretical work done in this area will be presented later in this chapter. The main work presented in this thesis focuses on the photochemistry of some of these important systems. By applying modern *ab-initio* methods, which will be described later, the aim is to obtain a good description of the nature and reactivity of excited states, which are crucial in photo-induced processes of transition metal systems and, in turn, to get a better understanding of these reactions.

1.1. Transition metal complexes: structure, bonding, stereochemistry and applications.

Transition metal complexes are systems consisting of a transition metal centre bonded to a particular number of ligands that can be of different types. The oldest transition metal complexes known are called Werner complexes or classical complexes, in which a metal atom binds to non-carbon ligands. In most cases the metal centre acts like a Lewis acid and the ligand as Lewis base. A Lewis acid is an atom, compound, or an ion that accepts an electron pair and Lewis base is an atom, compound, or an ion that

donates an electron pair. The bond formed between them is called coordinate bond or bipolar bond. Complexes in which the metal binds to the ligands through carbon or hydrogen atoms are called organometallic compounds and are characterised as being more covalent and having the metal centre more reduced in comparison with other classical complexes [40]. Ligands can be classified as L-type ligands, those that coordinate to metal through lone pair of electrons (CO, H₂O, NH₃ etc) or X-type ligands, those that donate to the metal centre one unpaired electron (alkyl radicals CR₃ etc.) and form with the metal a covalent bond. Metal atoms can be bound to a mixture of both, L and X type ligands that can donate different numbers of paired and unpaired electrons [41]. Ligands can be differentiated taking into account the number of atoms they use to bond to the metal centre, the so-called *hapticity*. Monodentate ligands are ligands attached to the metal centre through one atom (NO, H₂O, Cl⁻, OH⁻, etc.). Bidentate ligands are ligands attached by two atoms. Polydentate ligands are ligands, which are bonded to the metal centre through multiple atoms. Bidentate and polydentate ligands can also be called chelates as they enhance the stability of the complex by forming chelate rings with the metal atom. In chapter 3 of this thesis there are examples of mono and bidentate ligands. Chapter 4 of this thesis is focused on the work done on the photoisomerisation of (BQA)PtMe₂I complex where BQA - bis(8-quinoliny)amide belongs to the group of polydentate ligands. Chapters 5 and 6 contain work performed on the photochemistry of Cr (III) complexes with bidentate ligands such as oxalate – (C₂O₄)²⁻, and tn – 1,3-diaminopropane.

Transition metal complexes can have one or more metal centres [41]. Bonding between two metal atoms can occur directly by the overlap of pairs of d orbitals or through bridging ligands, which are ligands that are bonded simultaneously to both metal atoms. Depending on the type of coordination system, and the type of d overlap, different kinds of metal-metal bonds can be formed. σ -bonding occurs by the positive overlap of pairs of d_{z^2} orbitals, π -bonding occurs by the positive overlap of pairs of d_{xz} or d_{yz} orbitals and δ bonding occurs by the positive overlap of d_{xy} orbitals in this coordination system (Figure 1.1).

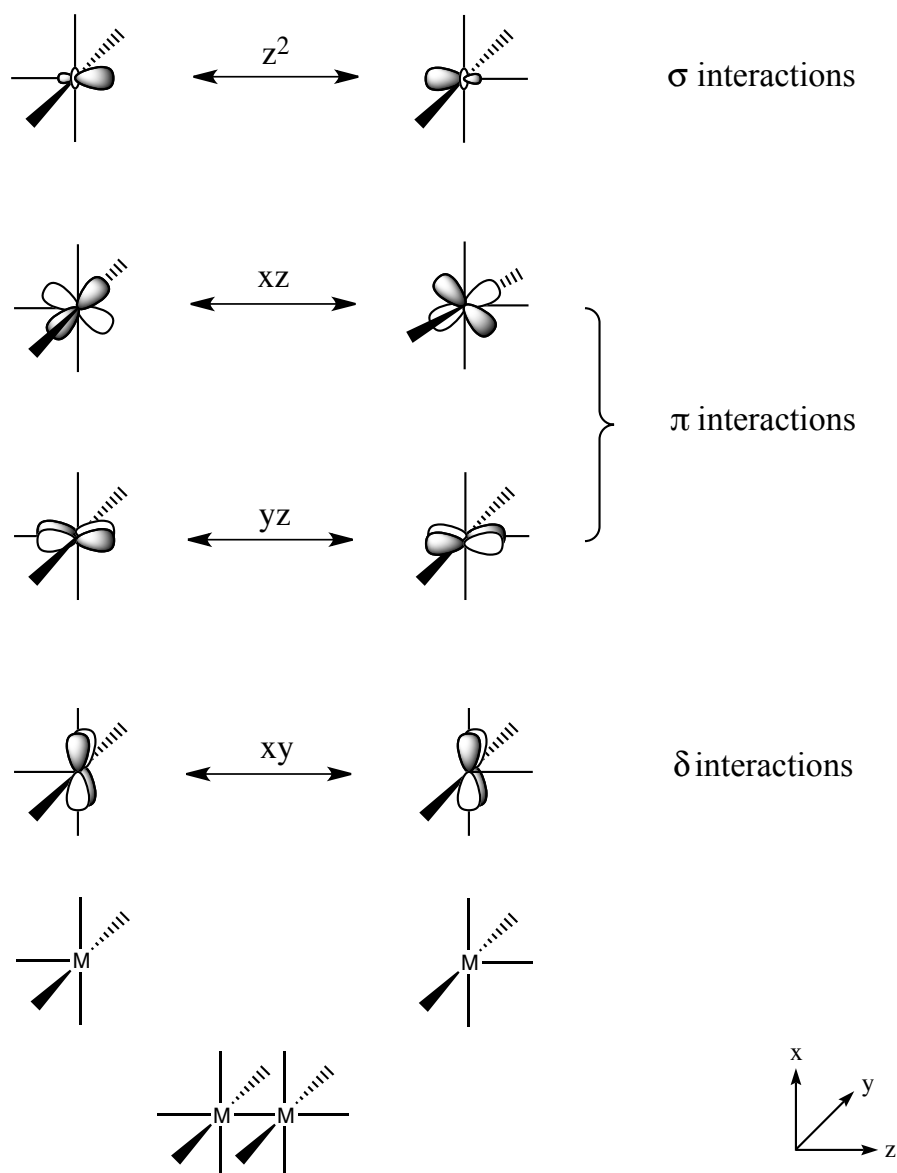


Figure. 1.1. Orbital interactions in M_2L_{10} bi-metallic complexes (picture adapted from Reference [41]).

Metal-metal systems can have different bond orders, a measure of the strength of the bond, which is the number of bonds formed between two metal atoms (bond order 0 = no bond; 1 = single bond; 2 = double bond etc.). It can qualitatively be calculated using following equation:

$$\text{bond order} = \frac{n_b - n_a}{2} \quad (1.1)$$

where n_b and n_a are numbers of occupied bonding and anti-bonding orbitals. However, as will be discussed later in section 3.2 of chapter 3 this is not necessarily a good indication of the bonding between two metal centres and quite sophisticated calculation can be required. This has been presented in the work of Roos and co-workers [42]. Using quantum chemical calculations on the uranium molecule U_2 they determine the bonding between two metal atoms as quintuple. They performed similar studies on the other actinides [43]. The high bond order between two metal atoms is also known for some bi-chromium systems, the vast majority of computational work on these systems has been done by the group of Roos and co-workers, who have shown that high level multiconfigurational/reference (see later) treatments are required to understand some metal-metal bonds [44-46].

In this thesis we will be looking at complexes containing only one or two metal centres. There are four main types of bi-metallic complexes: edge-sharing biooctahedra that can have bond orders from 1 to 3, face-sharing biooctahedra with bond orders of 2 or 3, tetragonal prismatic structures with bond orders from 1 to 4, and trigonal antiprismatic structures that favour bond orders of 3. The examples of structures and characteristics of the last 3 types of above will not be described here and can be found in many textbooks of inorganic chemistry [47]. Chapter 3 of this thesis focuses on the first type of those systems specifically the edge-sharing biooctahedral complex of molybdenum: $Mo_2(DXylF)_2(O_2CCH_3)_2(\mu_2-O)_2$ complex (where DXylF is N,N -bis(2,6-xylyl)formamidinate).

In order to describe the electronic structure of transition metal complexes there are three main theories that can be used: molecular orbital theory (MOT), crystal field theory (CFT) or ligand field theory (LFT) [41, 48]. In MOT, a transition metal complex is described using molecular orbitals, which are formed by the linear combination of the metal and ligand atomic orbitals of proper symmetry. The energetic order of these orbitals (bonding and anti-bonding) and their occupation can give a description about the chemical bonding of the system. In CFT, ligands are treated as negative point charges and the effect of the electric field formed by those charges on the metal is examined. Different orientation of the ligands, and so symmetry of the complex, can cause splitting of the metal d orbitals. The classical example here is an octahedral complex in which ligands are evenly spread to each corner of an octahedron, this causes

the metal d orbitals to split into two sets, a t_{2g} set of d_{xy} , d_{xz} and d_{yz} orbitals that is lower in energy and e_g set of d_{z^2} and $d_{x^2-y^2}$ orbitals that is higher in energy. The difference in energy between those two sets of orbitals is called crystal field splitting. Figure 1.2 presents the orbital splittings for octahedral ML_6 complexes.

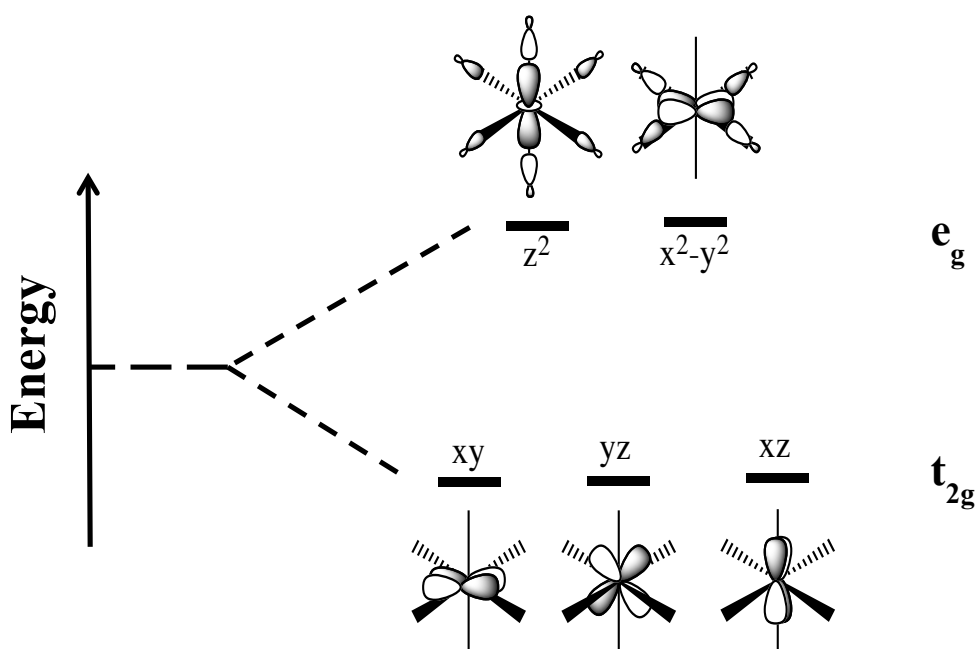


Figure 1.2. Orbital splittings for an Octahedral ML_6 complex (picture adapted from Reference [41]).

The splitting of the d orbitals is described by the Δ parameter and can be calculated using this electrostatic model. The size of this splitting indicates the wavelength of light absorption by the complex and so explains different colouring in metal systems. LFT is very closely related to CFT but also takes into account the covalent interactions between the atoms and the overlap of the metal and ligand molecular orbitals. The ordering of molecular orbitals (MOs) is predicted in the same way as in MOT. This theory has been extremely useful in spectroscopy of metal complexes [41]. Density Functional Theory (DFT) is an example of modern MOT, which gives very accurate descriptions of ground state properties of metal systems (as will be shown later). However, it is more approximate because there is no wavefunction. Thus for the excited state properties of such systems wavefunction methods, such as for example Configuration Interaction, need to be used. These are presented in the chapter 2 of this thesis.

Another very important aspect that needs to be looked at to determine electronic structure of given transition metal complex is the count of the total number of valence electrons around the metal centre. To calculate it, we need to sum up the number of valence electrons coming from the metal, all the L and X type ligands, each giving 2 or 1 electrons respectively, and subtract from the sum total charge of the complex. The number of valence electrons allows us to determine the electronic structure of the system.

Each transition metal valence shell consists of one s orbital, three p orbitals and five d orbitals which, when filled, give 18 valence electrons all together. Similar as the octet rule for the main group elements that tend to have 8 valence electrons (configuration of the closest noble gas), transition metals tend to 18 valence electrons to obtain a stable structure (e.g. most of the first row carbonyl complexes). For complexes with a large splitting parameter (containing high-field ligands) the rule works really well. The examples of such complexes are hydrides or carbonyls that are sterically small and form a bond to have the required 18 electrons. However, there are many exceptions to the rule. Square planar d^8 complexes such as $[\text{PtCl}_4]^{2-}$, $\text{IrCl}(\text{CO})(\text{PPh}_3)_2$ or $\text{PdCl}_2[(\text{PPh}_3)_2]$ tend to 16-electrons. The reason for this is that one of its nine valence orbitals (the $d_{x^2-y^2}$ orbital in this square planar arrangement of ligands around the metal) is usually very high in energy thus tends to be empty. Metal complexes containing hexaaqua ions $[\text{M}(\text{H}_2\text{O})_6]^+$ (M=V, Cr, Mn, Fe, Co, Ni) tend to have more than 18 electrons. This means that some anti-bonding MO would then have to be low in energy thus available for filling (complexes with weak field ligands) [41, 47].

One of the most challenging parts in this field is dealing with open shell configurations - in which the metal valence orbitals are not completely filled. The presence of single electrons in the frontier molecular orbitals of transition metal complexes presents additional challenges to the theoretical chemist, due to the possible involvement of higher multiplicity states (spin-orbit coupled states) such as doublet, triplet or quartet electronic states or, indeed, a mixture of these in the photochemistry of these complexes. State mixing causes problems even for the most successful computational methods. Some recent work on the photochemistry of transition metal complexes involving both closed and open shell systems will be presented later in this chapter.

Transition metal complexes can adopt a variety of structures. The most common systems are the complexes where metal centre adopts an octahedral geometry (examples include ML_6 complexes such as Group VI metal carbonyls or other ML_6 metal complexes such as $[Fe(CN)_6]^{4-}$, $[Cr(NH_3)_6]^{3+}$ etc.) but also trigonal bipyramidal ($Fe(CO)_5$ etc.), tetrahedral (CrO_4^{2-} , $Ni(CO)_4$ etc.) or square planar ($(Ni(CN)_4)^{2-}$, $[Pt(H_2O)_4]^{2+}$ etc.). Depending on the electronic structure of the central metal, the geometry of the system may be distorted from the ideal one (e.g. due to Jahn-Teller effects – which will be explained later in the theory chapter of this thesis). Isomers of those complexes are very common. There are two types of isomers: structural isomers and stereoisomers. Structural isomers have the same empirical formula but the ligands can be bonded in a different way, and differ in bond order. Stereoisomers have the same empirical formula but differ in the spatial arrangement of the ligands. Work presented later in this thesis concerns only stereoisomers so only this type of isomerisation will be discussed. There are two types of stereoisomers depending on their behaviour under the influence of polarized light: geometric isomers or optical isomers. Geometric isomers differ in positioning of the atoms, do not have a mirror plane of symmetry, and can have different physical and chemical properties (e.g. *cis* to *trans*, *meridional (mer)* to *facial (fac)* isomerisation). Chapter 4 of this thesis contains an example of *mer* to *fac* isomerisation of a (BQA)PtMe₂I complex under the influence of light and will be described in more detail later. Optical isomers are isomers that rotate plane-polarised light in two directions forming two optical isomers (right or left hand screw). They are very common for systems of type ML_3 where L is a chelate ligand, and such examples are discussed in chapter 5 namely $[Cr(C_2O_4)]^{3-}$ complex and in chapter 6 $[Cr(tn)_3]^{3+}$ complex.

The electronic spectroscopy of metal complexes is far more complex than the electronic spectroscopy of smaller non-metallic and organic systems [49, 50]. The excited electronic states, their reactivity and electronic structure can be very diverse [49, 51]. Electronic states can have different chemical character: ligand field states (LF), charge transfer states (CT), intra-ligand states (IL) and metal-centred states (MC). LF states are states characterised as d-d states and arise due to the splitting effect of the ligand on the d shell of the metal centre. CT states involve a transfer of electron density, be it from metal to ligand, ligand to metal or between ligands or parts of ligands, and generally

occur over longer distances than LF states. There are also CT states possible from ligand or from full complex to solvent. CT states are very common in transition metal complexes and are very important in many biological and industrial processes. They appear at higher energies and are usually more intense than the LF states because via the spectroscopic selection rules, they are formally allowed, whereas LF states are not [52]. IL states are very common in the photochemistry of organometallic complexes and involve a CT between two parts of the same ligand and are also formally allowed.

1.2. Review of some recent work done in the area of inorganic computational photochemistry.

While the field of inorganic photochemistry is not new, recent experimental work has begun to elucidate the nature of some fundamental photochemical reactions. One of the most studied parts of the field of inorganic photochemistry includes the transition metal carbonyls [53-57]. As mentioned previously, systems with transition metals possess many different electronic states with specific character and reactivity, which results in unexpected photochemical properties and can lead to vibronic coupling effects such as isomerisation through conical intersections (accidental or symmetry imposed - Jahn-Teller conical intersections), pseudo-Jahn-Teller distortions etc. (described later). In the past few decades a lot of experimental work on the dynamics and spectroscopy was performed in order to try to understand metal carbonyl photochemical dynamics. However, it is not always possible to define the exact nature of different states by experimental methods. An example is the assignment of the UV/Vis spectrum of $\text{Cr}(\text{CO})_6$, which is still the subject of some controversy some 45 years after it was first measured [58, 59]. Recent time-resolved spectroscopy has encouraged computational chemists to begin to tackle such challenging problems.

Paterson and co-workers studied the dynamics of chromium hexacarbonyl $\text{Cr}(\text{CO})_6$ photodissociation [11]. To define the mechanism of this reaction they used the Complete Active Space Self-Consistent Field (CASSCF) level of theory, which will be described in more detail in the next chapter. The results obtained were consistent with the experimental work done by the Fuß group [57]. They showed that a CO ligand dissociates within 100 fs, followed by radiationless decay via a Jahn-Teller conical

intersection. To describe the dynamics through this region they generated a model trajectory for it using surface hopping techniques. These results explained nicely previously puzzling features of vibrational coherence observed experimentally and encouraged full quantum wavepacket dynamics simulations of this process [12]. Other investigations on such systems were performed by Daniel and co-workers [60, 61]. They carried out calculations on the electronic spectroscopy of Cr(CO)₆ using different theoretical methods [61]. Given the comparison of the calculations with the experimental values, it was possible to determine the most accurate method, which in this case was Multi-State Complete Active Space 2nd order Perturbation Theory (MS-CASPT2). The main limitation of this approach is to build the wavefunction that will be able to describe in a correct way not only the ground state of a system but also excited states, thus the choice of the active space in the initial CASSCF calculation is important. The accuracy of other methods used such as Single Double Configuration Interaction (CISD), Equation-of-Motion Coupled Cluster Single and Double (EOM-CCSD), and Time Dependent Density Functional Theory (TD-DFT) was not very good from a quantitative point of view. Transition energies using CISD calculations were overestimated by around 40 eV but after adding (SD)² correction, the final values were then underestimated showing that this method is not very accurate and treats the states in an unbalanced way. EOM-CCSD calculations were overestimating the transition energies by approximately 0.5 eV. TD-DFT calculations were highly dependent on the functional used and the results were accurate only for the low energy part of the spectrum. However, qualitative comparison of all the methods confirmed experimental studies and gave insight into the nature of electronic states, while highlighting the challenges of applying standard excited state methodologies to TM complexes. These results show the efficiency of this approach applied to transition metal photochemistry.

The group of Daniel and co-workers is one the most active in the area of inorganic photochemistry and spectroscopy of transition metal systems [8]. Using state-of-the-art methodologies including multiconfigurational *ab-initio* wavefunction methods, density functional, and *ab-initio* response methods, together with wavepacket dynamics, they have achieved a large number of very important results in this area with a predominant number of studies focused on the transition metal systems containing carbonyl ligands [8, 60-77]. Some recent work in this group will be now reviewed. One paper [78] introduces the computational studies on the mechanism of photoisomerisation of Re (I)

carbonyl-diimine complex, $[\text{Re}(\text{CO})_3(\text{bpy})(\text{t-stpy})]^+$ (where stpy is 4-styrylpyridine and bpy is 2,2'-bipyridine) which has potential applications in optical data storage devices. Calculations were done using State-Averaged Complete Active Space (SA-CAS) and Multi-State 2nd order Perturbation Theories (MS-PT2). The theoretical spectrum of the complex reproduces very well the experimental one and the main absorption band at 332 nm is characterised as IL_{stpy} state. Excited states that have the biggest influence on the photoisomerisation process of this system have metal to ligand charge transfer (MLCT_{bpy}) character. The main structural deformations of the complex that lead to photoisomerisation are the torsion of the ethylenic carbon-carbon bond and also, as described in the paper, the Q_6 coordinate that includes six internal degrees of freedom and involves angle opening around the ethylenic C-C bond and rotations of the aromatic rings. The mechanism of the isomerisation process includes the absorption of singlet MLCT_{bpy} state, then very fast intersystem crossing (ISC) to the triplet MLCT_{bpy} state that is caused by large spin orbit coupling between those states. Another step of the photoisomerisation process is energy transfer from triplet MLCT_{bpy} state to long lived triplet IL_{stpy} and then slow decay to the ground state (*cis* or *trans* form of the molecule). In this study states with open-shell character are very important. Thanks to the multiconfigurational methods used it is possible to deal with them and understand the photoreaction in more detail. Another important study in this group involved electronic absorption spectroscopy of two Ru (II) polypyridyl complexes $[\text{Ru}(\text{phen})_2(\text{dppz})]^{2+}$ and $[\text{Ru}(\text{tap})_2(\text{dppz})]^{2+}$ (where phen=1,10-phenanthroline; tap=1,4,5,8-tetraazaphenanthrene; dppz=dipyridophenazine), that are good DNA intercalators and used in the cancer treatment as inhibitors of DNA replication, was presented in reference [79]. Two enantiomers of both systems were looked at alone and as intercalated into guanine-cytosine base pairs to form model systems for structural and spectroscopic properties. TD-DFT calculations (discussed later) in different environments were used to obtain the electronic spectra of these molecules. It was found that intercalation of Λ -enantiomers in DNA is less stabilised compared to Δ -enantiomers because of the presence of bending modes in the dppz ligands that causes their destabilisation. Calculations of bonding and spectral properties using solvation models reproduced experimental findings very well. However, calculations in vacuum were unreliable. MLCT_{tap} states are responsible for the main spectral properties of the $[\text{Ru}(\text{tap})_2(\text{dppz})]^{2+}$ system in water, acetonitrile or bases pair. For the $[\text{Ru}(\text{phen})_2(\text{dppz})]^{2+}$ system visible absorption spectrum in water and acetonitrile was dependent on $\text{MLCT}_{\text{dppz}}$ states. However the

absorption spectrum for the same system but intercalated in the guanine-cytosine bases pair is governed by $MLCT_{phen}$ states. The authors state that the enhanced π -character of the tap ligand in comparison with phen ligand is the reason of this behaviour. Important IL_{dppz} states for both systems are very sensitive to the environment and so in vacuum, water and acetonitrile have significant oscillator strengths and positions of the bands in vacuum moving to the spectra in the solutions is blue shifted of about 80 nm. These studies show that TD-DFT approach to spectroscopy of transition metal complexes can be very accurate and also computationally not too expensive.

The group of Baerends and co-workers has done a lot of work in the area of theoretical spectroscopy of transition metal systems using DFT methods [80-84]. Van Gisbergen et al have performed the first TD-DFT spectroscopic studies on systems containing transition metals including $(MnO_4)^-$, $Ni(CO)_4$, and $Mn_2(CO)_{10}$ [81]. Depending on the system and its geometry there were some discrepancies involving the ordering of electronic states, their relative energies, character and oscillator strengths for TD-DFT and some *ab-initio* and semi-empirical methods. It was especially prominent for the $(MnO_4)^-$ system, which involves very high mixing of close lying configurations. Nevertheless, the TD-DFT method in most cases obtained very accurate results comparable with other high level *ab-initio* methods and can be a good and much cheaper alternative for spectroscopic studies on large systems.

There has been a fair amount of work done in the area of spectroscopy of transition metal complexes using TD-DFT by Ziegler and co-workers [85-87]. Recent studies in this group involve mainly studies on the circular dichroism of different transition metal systems [88-95]. Circular dichroism (CD) spectroscopy measures the difference in absorption between the right and left hand circularly polarized light (R-CPL, L-CPL) for systems that contain chiral chromophores. The CD is measured over a range of wavelengths of such system and its signal will be non-zero if one of the circularly polarised light states will be stronger than the other. Whether the CD signal will be positive or negative depends which type of the circularly polarised light state will be absorbed to greater extent. CD is very useful for the determination of protein folding, assignment of electronic states and structure of chiral transition metal compounds. In the reference [92], CD spectroscopy studies on the iron group of complexes with tris-bidentate ligands $[M(L-L)_3]^{2+}$ (where M is Fe, Ru, Os and L-L is 2,2'-bipyridine) has

been presented. Results show good agreement of the CD simulated spectra with experiment. It was found that transitions in the low-energy region of the CD spectra for all the systems involve MLCT states coming from metals t_{2g} to the ligands lowest unoccupied molecular orbitals (LUMOs). For the iron complex it was earlier thought that those states are mainly metal centred d-d transitions. There are two main transitions in the high-energy region of the CD spectra, with high intensities and opposite signs with the positive one at the lower energy. These states involve mainly π to π^* transitions located on the ligands and are polarized along the axis connecting two N atoms. The difference in energies of particular LUMO orbitals that take part in the excitations causes the trigonal splitting of the bands. Similar studies, but using magnetic circular dichroism (MCD), were performed on the group of molybdenyl complexes [88]. MCD is induced by a strong magnetic field and it is very useful in the identification of excitations that are usually very hard to assign from the absorption spectrum. The method used in these studies is also based on TD-DFT and includes additional spin-orbit perturbation parameters.

The TD-DFT approach was also used in the studies of Si-H-M bridging interactions in the transition metal hydrosilane complexes and turned out to be successful in their explanation. Paterson and co-workers performed studies on the model system of $(\text{Cp}(\text{CO})_2\text{Mn}(\text{SiH}_4))$, where $\text{Cp} = \eta^5\text{-C}_5\text{H}_5$ [96]. They have used DFT with the B3LYP functional, in order to examine how the structure of the given complex changes, going from a regular trigonal bipyramid geometry (TBP) at Si to its distorted ground state minimum. The TD formulation of DFT was employed in order to characterise the lowest lying excited states for both structures. The authors correlated different electronic states of both structures along the distortion coordinate by looking at their Kohn-Sham orbitals and reported that the distortion of the regular TBP coordinated structure is followed by the migration of equatorial hydrogen along the Si-Mn bond. The hydrogen then adopts the bridging position between the Si and the metal atom. The authors explain and prove that this happens due to the pseudo-Jahn Teller distortion caused by the interaction of excited states. The distortion coordinate here is the antisymmetric bending vibration of Si-H_{eq} ligands.

As mentioned before, an important problem in the area of transition metal photochemistry is open-shell configurations. However, they are very challenging to

investigate especially for such large systems, and hence why there has not been much work done in this field. Ziegler and co-workers have performed TD-DFT studies on some open shell d^1 MLX_4 complexes [97]. Their results have shown that the TD-DFT method on these systems gives good comparison of excitation energies with experimental ones, with error only around 0.3-0.5 eV. There have been attempts to study circular dichroism spectroscopy using a spin-unrestricted version of TD-DFT. Fan and co-workers [98] performed those studies on different Cr (III) complexes $[Cr(L-L)_3]^{n+}$ with open-shell ground states where L-L are different saturated and unsaturated ligands: en(ethylenediamine), acac(acetylacetonate), ox(oxalate), mal(malonate), thiox(dithiooxalate)). Results show that this method can be used as a very useful tool in the assignment of CD spectra of complexes with unsaturated ligands. For complexes with saturated ligands CD spectra can be used only if their geometric parameters are known.

There has been a lot of experimental work done in the area of inorganic photochemistry. However, because it is very challenging to examine computationally, due to the reasons mentioned previously, there is still very little theoretical work done, unlike the area of organic photochemistry, in which experimental observations are widely supported by computational results.

This thesis will thus focus on the explanation of some important experimental observations in photo-stereochemistry and spectroscopy of TM complexes, using theoretical methodologies hence adding a novel, meaningful contribution to this field.

Chapter 2 of this work will present the main theoretical methods used in this thesis. Chapters 3-6 will present the results on photochemistry and spectroscopy of different types of TM complexes mentioned previously, including closed and open shell systems.

1.3. List of references.

- [1] Vreven, T.; Bernardi, F.; Garavelli, M.; Olivucci, M.; Robb, M. A.; Schlegel, H. B., *Ab initio* Photoisomerization Dynamics of a Simple Retinal Chromophore Model. *J. Am. Chem. Soc.* **1997**, 119, 12687-12688.
- [2] Groenhof, G.; Bouxin-Cademartory, M.; Hess, B.; De Visser, S. P.; Berendsen, H. J. C.; Olivucci, M.; Mark, A. E.; Robb, M. A., Photoactivation of the Photoactive Yellow Protein: Why Photon Absorption Triggers a *trans*-to-*cis* Isomerization of the Chromophore in the Protein. *J. Am. Chem. Soc.* **2004**, 126, 4228-4233.
- [3] Groenhof, G.; Schafer, L. V.; Boggio-Pasqua, M.; Grubmuller, H.; Robb, M. A., Arginine52 Controls the Photoisomerization Process in Photoactive Yellow Protein. *J. Am. Chem. Soc.* **2008**, 130, 3250-3251.
- [4] Barbatti, M.; Lischka, H., Nonadiabatic Deactivation of 9 H-Adenine: A Comprehensive Picture Based on Mixed Quantum-Classical Dynamics. *J. Am. Chem. Soc.* **2008**, 130, 6831-6839.
- [5] Blancafort, L.; Cohen, B.; Hare, P. M.; Kohler, B.; Robb, M. A., Singlet Excited-State Dynamics of 5-Fluorocytosine and Cytosine: An Experimental and Computational Study. *J. Phys. Chem. A* **2005**, 109, 4431-4436.
- [6] Harańczyk, M.; Gutowski, M.; Li, X. A.; Bowen, K. H., Adiabatically Bound Valence Anions of Guanine. *J. Phys. Chem. B* **2007**, 111, 14073-14076.
- [7] Li, X.; Bowen, K. H.; Harańczyk, M.; Bachorz, R. A.; Mazurkiewicz, K.; Rak, J.; Gutowski, M., Photoelectron Spectroscopy of Adiabatically Bound Valence Anions of Rare Tautomers of the Nucleic Acid Bases. *J. Chem. Phys.* **2007**, 127, 174309.
- [8] Daniel, C., Electronic Spectroscopy and Photoreactivity in Transition Metal Complexes. *Coord. Chem. Rev.* **2003**, 238, 143-166.
- [9] Daniel, C., Electronic Spectroscopy and Photoreactivity of Transition Metal Complexes: Quantum Chemistry and Wave Packet Dynamics *Top. Curr. Chem.* **2004**, 241, 119-165.
- [10] Paterson, M. J.; Blancafort, L.; Wilsey, S.; Robb, M. A., Photoinduced Electron Transfer in Squaraine Dyes: Sensitization of Large Band Gap Semiconductors. *J. Phys. Chem. A* **2002**, 106, 11431-11439.

- [11] Paterson, M. J.; Hunt, P. A.; Robb, M. A.; Takahashi, O., Non-adiabatic Direct Dynamics Study of Chromium Hexacarbonyl Photodissociation. *J. Phys. Chem. A* **2002**, 106, 10494-10504.
- [12] Worth, G. A.; Welch, G.; Paterson, M. J., Wavepacket Dynamics Study of Cr(CO)₅ after Formation by Photodissociation: Relaxation through an (E ⊕ A) ⊕ e Jahn-Teller Conical Intersection. *Mol. Phys.* **2006**, 104, 1095-1105.
- [13] Scaiano, J. C.; Ramamurthy, V.; Turro, N. J., *Modern Molecular Photochemistry of Organic Molecules*. University Science Books: Sausalito, California, 2009.
- [14] Garavelli, M., Computational Organic Photochemistry: Strategy, Achievements and Perspectives. *Theor. Chem. Acc.* **2006**, 116, 87-105.
- [15] Robb, M. A.; Garavelli, M.; Olivucci, M.; Bernardi, F., A Computational Strategy for Organic Photochemistry. *Rev. Comp. Chem.* **2000**, 15, 87-146.
- [16] Gupta, K. C.; Sutar, A. K., Catalytic Activities of Schiff Base Transition Metal Complexes. *Coord. Chem. Rev.* **2008**, 252, 1420-1450.
- [17] Marciniak, B.; Maciejewski, H., Transition Metal-Siloxide Complexes; Synthesis, Structure and Application to Catalysis. *Coord. Chem. Rev.* **2001**, 223, 301-335.
- [18] Carmona, D.; Lamata, M. P.; Oro, L. A., Recent Advances in Homogeneous Enantioselective Diels-Alder Reactions Catalyzed by Chiral Transition-Metal Complexes. *Coord. Chem. Rev.* **2000**, 200, 717-772.
- [19] Wong, K. Y.; Cheung, K. C.; Wong, W. L.; Ma, D. L.; Lai, T. S., Transition Metal Complexes as Electrocatalysts - Development and Applications in Electro-Oxidation Reactions. *Coord. Chem. Rev.* **2007**, 251, 2367-2385.
- [20] Verpoort, F.; Drozdak, R.; Allaert, B.; Ledoux, N.; Dragutan, I.; Dragutan, V., Ruthenium Complexes Bearing Bidentate Schiff Base Ligands as Efficient Catalysts for Organic and Polymer Syntheses. *Coord. Chem. Rev.* **2005**, 249, 3055-3074.
- [21] Hennig, H., Homogeneous Photo Catalysis by Transition Metal Complexes. *Coord. Chem. Rev.* **1999**, 182, 101-123.
- [22] Troegel, D.; Stohrer, J., Recent Advances and Actual Challenges in Late Transition Metal Catalyzed Hydrosilylation of Olefins from an Industrial Point of View. *Coord. Chem. Rev.* **2011**, 255, 1440-1459.

- [23] Stiefel, E. I., Transition Metal Sulfur Chemistry: Biological and Industrial Significance and Key Trends. In *ACS Symposium Series*, American Chemical Society: Washington, 1996; Vol. 653, pp 2-38.
- [24] Gunay, A.; Theopold, K. H., C-H Bond Activations by Metal Oxo Compounds. *Chem. Rev.* **2010**, 110, 1060-1081.
- [25] Pitie, M.; Pratviel, G., Activation of DNA Carbon-Hydrogen Bonds by Metal Complexes. *Chem. Rev.* **2010**, 110, 1018-1059.
- [26] Szaciłowski, K.; Macyk, W.; Drzewiecka-Matuszek, A.; Brindell, M.; Stochel, G., Bioinorganic Photochemistry: Frontiers and Mechanisms. *Chem. Rev.* **2005**, 105, 2647-2694.
- [27] McMillin, D. R.; McNett, K. M., Photoprocesses of Copper Complexes That Bind to DNA. *Chem. Rev.* **1998**, 98, 1202-1219.
- [28] Haas, K. L.; Franz, K. J., Application of Metal Coordination Chemistry To Explore and Manipulate Cell Biology. *Chem. Rev.* **2009**, 109, 4921-4960.
- [29] Orvig, C.; Thompson, K. H., Boon and Bane of Metal Ions in Medicine. *Science* **2003**, 300, 936-939.
- [30] Sun, R. W. Y.; Ma, D. L.; Wong, E. L. M.; Che, C. M., Some Uses of Transition Metal Complexes as anti-Cancer and anti-HIV Agents. *Dalton Trans.* **2007**, 4884-4892.
- [31] Rafique, S.; Idrees, M.; Nasim, A.; Akbar, H.; Athar, A., Transition Metal Complexes as Potential Therapeutic Agents. *Biotechnol. Mol. Biol. Rev.* **2010**, 5, 38-45.
- [32] Guo, Z. J.; Zhang, J. Y.; Liu, Q.; Duan, C. Y.; Shao, Y.; Ding, J.; Miao, Z. H.; You, X. Z., Structural Evidence for the Facile Chelate-ring Opening Reactions of Novel Platinum(II)-Pyridine Carboxamide Complexes. *J. Chem. Soc.: Dalton Trans.* **2002**, 591-597.
- [33] Wong, E.; Giandomenico, C. M., Current Status of Platinum Based Antitumor Drugs. *Chem. Rev.* **1999**, 99, 2451-2466.
- [34] Hoffman, M. R.; Martin, S. T.; Choi, W.; Bahnemann, D. W., Environmental Applications of Semiconductor Photocatalysis. *Chem. Rev.* **1995**, 95, 69-96.
- [35] Potje-Kamloth, K., Semiconductor Junction Gas Sensors. *Chem. Rev.* **2008**, 108, 367-399.

- [36] Kalyanasundaram, K.; Gratzel, M., Applications of Functionalized Transition Metal Complexes in Photonic and Optoelectronic Devices. *Coord. Chem. Rev.* **1998**, 177, 347-414.
- [37] Wagenknecht, P. S.; Ford, P. C., Metal Centered Ligand Field Excited States: Their Roles in the Design and Performance of Transition Metal Based Photochemical Molecular Devices. *Coord. Chem. Rev.* **2011**, 255, 591-616.
- [38] Chi, Y.; Chou, P. T., Transition-Metal Phosphors with Cyclometalating Ligands: Fundamentals and Applications. *Chem. Soc. Rev.* **2010**, 39, 638-655.
- [39] Van Veldhoven, E.; Zhang, H.; Glasbeek, M., (Sub)Picosecond Time-Resolved Fluorescence Depolarization of OLED Compounds Alq₃, Gaq₃, and Inq₃. In *Ultrafast Phenomena XII*, Springer, Ed. New York, 2001; pp 482-484.
- [40] Crabtree, R. H., *The Organometallic Chemistry of Transition Metals*. Fourth Edition ed.; Wiley-Interscience: Hoboken, New Jersey, 2005.
- [41] Jean, Y., *Molecular Orbitals of Transition Metal Complexes*. Oxford University Press Inc., New York: Oxford, 2005.
- [42] Gagliardi, L.; Roos, B. O., Quantum Chemical Calculations Show that the Uranium Molecule U₂ has a Quintuple Bond. *Nature* **2005**, 433, 848-851.
- [43] Roos, B. O.; Malmqvist, P. A.; Gagliardi, L., Exploring the Actinide-Actinide Bond: Theoretical Studies of the Chemical Bond in Ac₂, Th₂, Pa₂, and U₂. *J. Am. Chem. Soc.* **2006**, 128, 17000-17006.
- [44] Gagliardi, L.; La Macchia, G.; Manni, G. L.; Todorova, T. K.; Brynda, M.; Aquilante, F.; Roos, B. O., On the Analysis of the Cr-Cr Multiple Bond in Several Classes of Dichromium Compounds. *Inorg. Chem.* **2010**, 49, 5216-5222.
- [45] Brynda, M.; Gagliardi, L.; Widmark, P. O.; Power, P. P.; Roos, B. O., A Quantum Chemical Study of the Quintuple Bond Between Two Chromium Centers in [PhCrCrPh]: *Trans*-bent Versus Linear Geometry. *Angew. Chem. Int. Edit.* **2006**, 45, 3804-3807.
- [46] Gagliardi, L.; La Macchia, G.; Aquilante, F.; Veryazov, V.; Roos, B. O., Bond Length and Bond Order in One of the Shortest Cr-Cr Bonds. *Inorg. Chem.* **2008**, 47, 11455-11457.
- [47] Cotton, F. A.; Wilkinson, G.; Murillo, C. A.; Bochmann, M., *Advanced Inorganic Chemistry*. Sixth ed.; Wiley-Interscience: 1999.

- [48] Balzani, V., Photophysics of Transition Metal Complexes in Solution. In *Handbook of Photochemistry* Taylor & Francis Group, LLC: 2006; pp 49-82.
- [49] Adamson, A. W.; Fleischauer, P. D., *Concepts of Inorganic Photochemistry*. John Wiley & Sons, Inc.: New York, 1975.
- [50] Daniel, C., Photochemistry of Transition Metal Complexes: Theory. In *Encyclopedia of Inorganic Chemistry*, 2006.
- [51] Ferraudi, G. J., *Elements of Inorganic Photochemistry*. John Wiley & Sons, Inc.: New York, 1988.
- [52] Pierloot, K., Calculations of Electronic Spectra of Transition Metal Complexes. In *Computational Photochemistry*, Olivucci, M., Ed. Elsevier B. V.: 2005; Vol. 16.
- [53] Fuss, W.; Trushin, S. A.; Schmid, W. E., Ultrafast Photochemistry of Metal Carbonyls. *Res. Chem. Intermediat.* **2001**, *27*, 447-457.
- [54] Kim, S. K.; Pedersen, S.; Zewail, A. H., Femtochemistry of Organometallics - Dynamics of Metal-Metal and Metal-Ligand Bond-Cleavage in $M_2(CO)_{10}$. *Chem. Phys. Lett.* **1995**, *233*, 500-508.
- [55] Rubner, O.; Engel, V., Fragmentation Dynamics of $Fe(CO)_5$ upon Femtosecond Excitation: A Time-Dependent Statistical Description. *Chem. Phys. Lett.* **1998**, *293*, 485-490.
- [56] Trushin, S. A.; Kosma, K.; Fuss, W.; Schmid, W. E., Wavelength-Independent Ultrafast Dynamics and Coherent Oscillation of a Metal-Carbon Stretch Vibration in Photodissociation of $Cr(CO)_6$ in the Region of 270-345 nm. *Chem. Phys.* **2008**, *347*, 309-323.
- [57] Trushin, S. A.; Fuss, W.; Schmid, W. E., Conical Intersections, Pseudorotation and Coherent Oscillations in Ultrafast Photodissociation of Group-6 Metal Hexacarbonyls. *Chem. Phys.* **2000**, *259*, 313-330.
- [58] Gray, H. B.; Beach, N. A., The Electronic Structures of Octahedral Metal Complexes. I. Metal Hexacarbonyls and Hexacyanides. *J. Am. Chem. Soc.* **1963**, *85*, 2922-2927.
- [59] Sébastien Villaume; Alain Strich; Chantal Daniel; S. Ajith Perera; Bartlett, R. J., A Coupled Cluster Study of the Electronic Spectroscopy and Photochemistry of $Cr(CO)_6$. *Phys. Chem. Chem. Phys.* **2007**, *46*, 6115-6122.

- [60] Gonzalez, L.; Ambrosek, D.; Villaume, S.; Daniel, C., A Multi State-CASPT2 vs. TD-DFT Study of the Electronic Excited States of $\text{RCo}(\text{CO})_4$ ($\text{R} = \text{H}, \text{CH}_3$) Organometallic Complexes. *Chem. Phys. Lett.* **2006**, 417, 545-549.
- [61] Ben Amor, N.; Villaume, S.; Maynau, D.; Daniel, C., The Electronic Spectroscopy of Transition Metal Carbonyls: The Tough Case of $\text{Cr}(\text{CO})_6$. *Chem. Phys. Lett.* **2006**, 421, 378-382.
- [62] Daniel, C., The Photochemistry of Transition-Metal Hydrides - A CASSCF/CCI Study of the Photodissociation of $\text{HMn}(\text{CO})_5$. *J. Am. Chem. Soc.* **1992**, 114, 1625-1631.
- [63] Marquez, A.; Daniel, C.; Sanz, J. F., The Vacuum-Ultraviolet Spectrum of $\text{Fe}(\text{CO})_5$ - An Experimental-Analysis Supported by a CASSCF CCI Study of the Rydberg States. *J. Phys. Chem.* **1992**, 96, 121-123.
- [64] Daniel, C.; Heitz, M. C.; Lehr, L.; Manz, J.; Schroder, T., Polanyi Rules for Ultrafast Unimolecular Reactions - Simulations for $\text{HCo}(\text{CO})_4^1(\text{E}^*) - \text{H} + \text{CO}(\text{CO})_4$. *J. Phys. Chem.* **1993**, 97, 12485-12490.
- [65] Finger, K.; Daniel, C., Metal-to-Ligand Charge Transfer Photochemistry - Potential Energy Curves for the Photodissociation of $\text{HMn}(\text{CO})_3(\text{DAB})$. *J. Am. Chem. Soc.* **1995**, 117, 12322-12327.
- [66] Guillaumont, D.; Daniel, C., A CASSCF Study of the Relaxation Effects in the Lowest $^3\text{MLCT}$ Excited State of $\text{HMn}(\text{CO})_3(\text{dab})$. *Chem. Phys. Lett.* **1996**, 257, 1-7.
- [67] Heitz, M. C.; Ribbing, C.; Daniel, C., Spin-Orbit Induced Radiationless Transitions in Organometallics: Quantum Simulation of the Intersystem Crossing Processes in the Photodissociation of $\text{HCo}(\text{CO})_4$. *J. Chem. Phys.* **1997**, 106, 1421-1428.
- [68] Hachey, M. R. J.; Daniel, C., The Spectroscopy of $\text{HMn}(\text{CO})_5$: A CASSCF/MRCI and CASPT2 *Ab Initio* Study. *Inorg. Chem.* **1998**, 37, 1387-1391.
- [69] Guillaumont, D.; Daniel, C., Photodissociation and Electronic Spectroscopy of $\text{Mn}(\text{H})(\text{CO})_3(\text{H-DAB})$ ($\text{DAB} = 1,4\text{-diazabuta-1,3-diene}$): Quantum Wave Packet Dynamics Based on *Ab Initio* Potentials. *J. Am. Chem. Soc.* **1999**, 121, 11733-11743.
- [70] Rubner, O.; Engel, V.; Hachey, M. R.; Daniel, C., A CASSCF/MR-CCI Study of the Excited States of $\text{Fe}(\text{CO})_5$. *Chem. Phys. Lett.* **1999**, 302, 489-494.

- [71] Kuhn, O.; Hachey, M. R. D.; Rohmer, M. M.; Daniel, C., A CASSCF/CASPT2 Study of the Low-Lying Excited States of $\text{Mn}_2(\text{CO})_{10}$. *Chem. Phys. Lett.* **2000**, 322, 199-206.
- [72] Guillaumont, D.; Vlcek, A.; Daniel, C., Photoreactivity of $\text{Cr}(\text{CO})_4(2,2'$ -bipyridine): Quantum Chemistry and Photodissociation Dynamics. *J. Phys. Chem. A* **2001**, 105, 1107-1114.
- [73] Costa, P. J.; Calhorda, M. J.; Bossert, J.; Daniel, C.; Romao, C. C., Photochemistry of Methyltrioxorhenium Revisited: A DFT/TD-DFT and CASSCF/MS-CASPT2 Theoretical Study. *Organometallics* **2006**, 25, 5235-5241.
- [74] Gonzalez, L.; Daniel, C., Photochemistry of $\text{CH}_3\text{Mn}(\text{CO})_5$: A Multiconfigurational *Ab Initio* Study. *J. Comput. Chem.* **2006**, 27, 1781-1786.
- [75] Ambrosek, D.; Villaume, S.; Daniel, C.; Gonzalez, L., Photoactivity and UV Absorption Spectroscopy of $\text{RCo}(\text{CO})_4$ ($\text{R} = \text{H}, \text{CH}_3$) Organometallic Complexes. *J. Phys. Chem. A* **2007**, 111, 4737-4742.
- [76] Ben Amor, N.; Ambrosek, D.; Daniel, C.; Marquardt, R., Photodissociation Dynamics of Trimethyltin Iodide. *Chem. Phys.* **2007**, 338, 81-89.
- [77] Finger, K.; Daniel, C.; Saalfrank, P.; Schmidt, B., Nonadiabatic Effects in the Photodissociation and Electronic Spectroscopy of $\text{HMn}(\text{CO})_3(\text{dab})$: Quantum Wave Packet Dynamics Based on *Ab Initio* Potentials. *J. Phys. Chem.* **1996**, 100, 3368-3376.
- [78] Gindensperger, E.; Köppel, H.; Daniel, C., Mechanism of Visible-Light Photoisomerization of a Rhenium (I) Carbonyl-Diimine Complex. *Chem. Commun.* **2010**, 46, 8225-8227.
- [79] Daniel, C.; Ambrosek, D.; Loos, P. F.; Assfeld, X., A Theoretical Study of Ru(II) Polypyridyl DNA Intercalators. Structure and Electronic Absorption Spectroscopy of $[\text{Ru}(\text{phen})_2(\text{dppz})]^{2+}$ and $[\text{Ru}(\text{tap})_2(\text{dppz})]^{2+}$ Complexes Intercalated in Guanine-Cytosine Base Pairs. *J. Inorg. Biochem.* **2010**, 104, 893-901.
- [80] Aarnts, M. P.; Wilms, M. P.; Peelen, K.; Fraanje, J.; Goubitz, K.; Hartl, F.; Stufkens, D. J.; Baerends, E. J.; Vlcek, A., Bonding Properties of a Novel Inorganometallic Complex, $\text{Ru}(\text{SnPh}_3)_2(\text{CO})_2(\text{IPr-DAB})$ (IPr-DAB = N,N'-Diisopropyl-1,4-diaza-1,3-butadiene), and its Stable Radical-Anion, Studied by

- UV-Vis, IR, and EPR Spectroscopy, (Spectro-) Electrochemistry, and Density Functional Calculations. *Inorg. Chem.* **1996**, 35, 5468-5477.
- [81] van Gisbergen, S. J. A.; Groeneveld, J. A.; Rosa, A.; Snijders, J. G.; Baerends, E. J., Excitation Energies for Transition Metal Compounds from Time-Dependent Density Functional Theory. Applications to MnO_4^- , $\text{Ni}(\text{CO})_4$, and $\text{Mn}_2(\text{CO})_{10}$. *J. Phys. Chem. A* **1999**, 103, 6835-6844.
- [82] Baerends, E. J.; Hieringer, W., First Hyperpolarizability of a Sesquifulvalene Transition Metal Complex by Time-Dependent Density-Functional Theory. *J. Phys. Chem. A* **2006**, 110, 1014-1021.
- [83] Baerends, E. J.; Bouten, R.; van Lenthe, E.; Visscher, L.; Schreckenbach, G.; Ziegler, T., Relativistic Effects for NMR Shielding Constants in Transition Metal Oxides Using the zeroth-order Regular Approximation. *J. Phys. Chem. A* **2000**, 104, 5600-5611.
- [84] Ehlers, A. W.; RuizMorales, Y.; Baerends, E. J.; Ziegler, T., Dissociation Energies, Vibrational Frequencies, and ^{13}C NMR Chemical Shifts of the 18-electron Species $[\text{M}(\text{CO})_6]^n$ ($\text{M} = \text{Hf-Ir}, \text{Mo}, \text{Tc}, \text{Ru}, \text{Cr}, \text{Mn}, \text{Fe}$). A Density Functional Study. *Inorg. Chem.* **1997**, 36, 5031-5036.
- [85] Casarin, M.; Finetti, P.; Vittadini, A.; Wang, F.; Ziegler, T., Spin-Orbit Relativistic Time-Dependent Density Functional Calculations of the Metal and Ligand pre-edge XAS Intensities of Organotitanium Complexes: TiCl_4 , $\text{Ti}(\eta^5\text{-C}_5\text{H}_5)\text{Cl}_3$, and $\text{Ti}(\eta^5\text{-C}_5\text{H}_5)_2\text{Cl}_2$. *J. Phys. Chem. A* **2007**, 111, 5270-5279.
- [86] Fronzoni, G.; Stener, M.; Decleva, P.; Wang, F.; Ziegler, T.; van Lenthe, E.; Baerends, E. J., Spin-Orbit Relativistic Time Dependent Density Functional Theory Calculations for the Description of Core Electron Excitations: TiCl_4 Case Study. *Chem. Phys. Lett.* **2005**, 416, 56-63.
- [87] Seth, M.; Ziegler, T., Calculation of Excitation Energies of Open-Shell Molecules with Spatially Degenerate Ground States. I. Transformed Reference via an Intermediate Configuration Kohn-Sham Density-Functional Theory and Applications to d^1 and d^2 Systems with Octahedral and Tetrahedral Symmetries. *J. Chem. Phys.* **2005**, 123.
- [88] Ziegler, T.; Hernandez-Marin, E.; Seth, M., Density Functional Theory Study of the Magnetic Circular Dichroism Spectra of Molybdenyl Complexes. *Inorg. Chem.* **2010**, 49, 6066-6076.

- [89] Ziegler, T.; Hernandez-Marin, E.; Seth, M., A Theoretical Study of the Magnetic Circular Dichroism Spectrum for Sulfite Oxidase Based on Time-Dependent Density Functional Theory. *Inorg. Chem.* **2009**, 48, 2880-2886.
- [90] Ziegler, T.; Seth, M., Magnetic Circular Dichroism Spectrum of Plastocyanin by Calculation. *Inorg. Chem.* **2009**, 48, 1793-1795.
- [91] Von Zelewsky, A.; Ziegler, M., Charge-Transfer Excited State Properties of Chiral Transition Metal Coordination Compounds Studied by Chiroptical Spectroscopy. *Coord. Chem. Rev.* **1998**, 177, 257-300.
- [92] Ziegler, T.; Fan, J.; Autschbach, J., Electronic Structure and Circular Dichroism of Tris(bipyridyl) Metal Complexes within Density Functional Theory. *Inorg. Chem.* **2010**, 49, 1355-1362.
- [93] Ziegler, T.; Zhekova, H. R.; Seth, M., A Magnetic and Electronic Circular Dichroism Study of Azurin, Plastocyanin, Cucumber Basic Protein, and Nitrite Reductase Based on Time-Dependent Density Functional Theory Calculations. *J. Phys. Chem. A* **2010**, 114, 6308-6321.
- [94] Seth, M.; Krykunov, M.; Ziegler, T.; Autschbach, J.; Banerjee, A., Application of Magnetically Perturbed Time-Dependent Density Functional Theory to Magnetic Circular Dichroism: Calculation of *B* Terms. *J. Chem. Phys.* **2008**, 128, 144105.
- [95] Seth, M.; Ziegler, T.; Autschbach, J., Application of Magnetically Perturbed Time-Dependent Density Functional Theory to Magnetic Circular Dichroism. III. Temperature-Dependent Magnetic Circular Dichroism Induced by Spin-Orbit Coupling. *J. Chem. Phys.* **2008**, 129, 104105.
- [96] Paterson, M. J.; Chatterton, N. P.; McGrady, G. S., View from the Bridge: A Pseudo-Jahn-Teller Approach to Transition Metal Hydrosilane Complexes. *New J. Chem.* **2004**, 28, 1434-1436.
- [97] Ziegler, T.; Wang, F., Excitation Energies of some d^1 Systems Calculated using Time-Dependent Density Functional Theory: An Implementation of Open-Shell TDDFT Theory for Doublet-Doublet Excitations. *Mol. Phys.* **2004**, 102, 2585-2595.
- [98] Ziegler, T.; Fan, J.; Seth, M.; Autschbach, J., Circular Dichroism of Trigonal Dihedral Chromium (III) Complexes: A Theoretical Study based on Open-Shell Time-Dependent Density Functional Theory. *Inorg. Chem.* **2008**, 47, 11656-11668.

CHAPTER 2

Theoretical Background

To computationally describe a molecule one needs to characterise its potential energy surface (PES), which is a hypersurface with $3N-6$ degrees of freedom ($3N-5$ for linear molecules), where N is the number of atoms in a molecule. Defining the PES will give information about the possible structures of a given system, their relative energies and stability. The structure at a point on the PES at which the first derivative of the energy (gradient) with respect to geometry is equal to zero and all the second derivatives (Hessian eigenvalues) are positive is called a minimum. There can be two types of minima, a global minimum, which is a structure with the lowest possible energy and local minima that are structures of higher energies than the global minimum. First-order saddle points (maxima along one coordinate) are other important points on PESs at which the gradient is zero but one of the Hessian eigenvalues is negative, which means there is one vibrational mode that when followed will relax the system downhill to a minimum. These are also called transition states, which provide lowest energy barriers between two different minima. To locate a minimum on PES the process of structure optimisation needs to be performed i.e. locating the lowest energy of a system with respect to the change of structural coordinates. This is described later in section 2.5 of this chapter.

Chemistry that is not induced by light (i.e. thermochemistry) can be described by examining the ground state PES of a system. However, to describe the photochemistry of a given system, excited state PESs are also required. Unfortunately, accurate theoretical characterisation of PESs for larger systems is very challenging due to the presence of a large number of degrees of freedom; thus the surfaces become multidimensional and they can cross, allowing for phenomena such as conical intersections, intersystem and avoided crossings, which can be very hard to compute as well as to visualise. Such phenomena will be described later in this thesis. For illustrative purposes figure 2.1 represents a ground state and an excited state PES, with transition states and minima, and their crossing with each other.

To theoretically examine the chemistry of a system one can use computational methodologies based on quantum mechanics. This thesis will be focused mainly on the theoretical methods that can be used to describe photochemistry i.e. chemistry in electronically excited states. Such methods can be used to accurately study both the electronic spectroscopy as well as reactive multi-state potential energy surfaces,

although it should be noted that these methods tend to be complementary to one-another and have different domains of applicability.

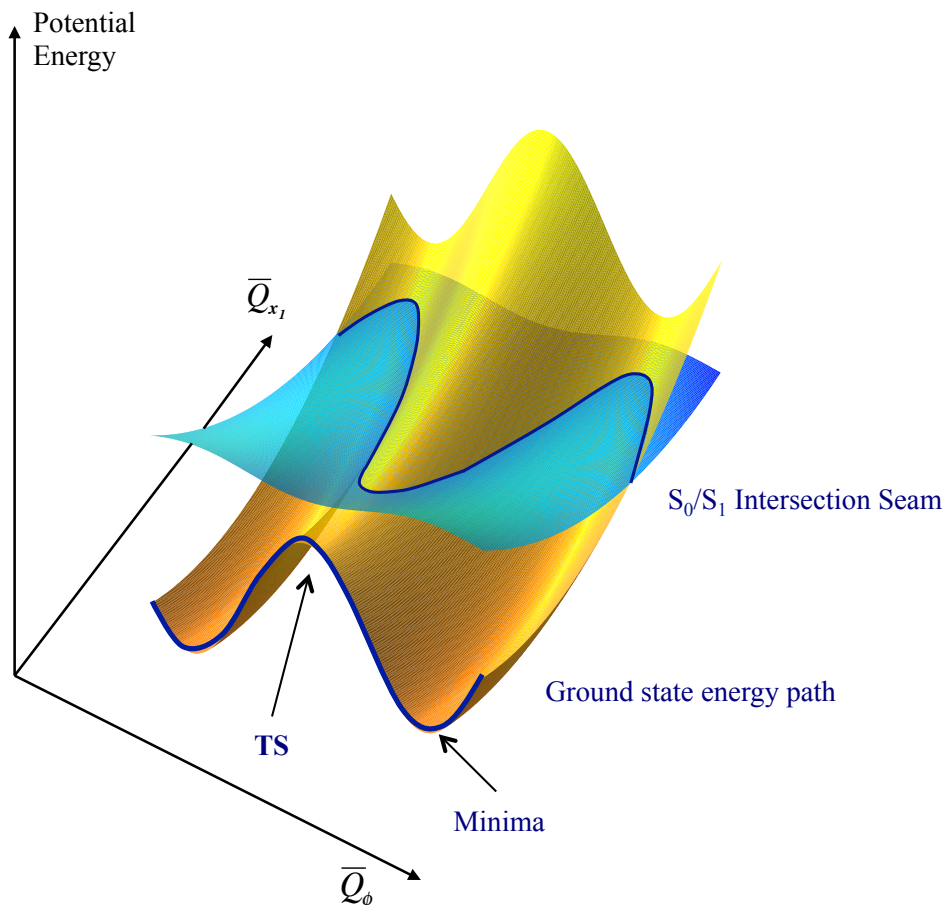


Figure 2.1. Schematic representation of the ground state PES reaction path and its crossing with PES of first excited state (picture adapted from Reference [1]).

2.1. The wavefunction, Schrödinger equation and Born-Oppenheimer approximation.

To be able to treat electronically excited state one has to be familiar with the central concept of quantum mechanics such as the “duality of matter”. De Broglie’s discovery, that light can have particle-like character and that particles can have wave-like character changed dramatically the way we think about chemical systems and their interaction with light. This was crucial to the evolution of modern quantum mechanics.

The duality of matter allowed the idea of a wavefunction to be developed in which a wavefunction can theoretically describe any physical eigenstate of the system and when operated upon by suitable operator $\hat{\Omega}$ it will return any property of the system it describes. A wavefunction is denoted as $\Psi(r,t)$ in the case of a time-dependent wavefunction or as $\psi(r)$ in the case of a time-independent wavefunction, where r corresponds to spatial coordinate(s) of particle(s). To describe a required property of the system under study there are some requirements that need to be met. Wavefunction must be the eigenfunction of given operator $\hat{\Omega}$. The operator working on the wavefunction results in the observable that represents the property that is sought. The eigenvalue ω will be the result of this operator working on the wavefunction [2].

Max Born introduced an interpretation of the wavefunction which is now commonly used in quantum mechanics, and which states that the probability of finding a particle in a volume of space $d\tau$ at the point r is proportional to the square of the wavefunction and is called probability density $|\psi(r)|^2$. The wavefunction is considered as an amplitude of this probability and has to be square integrable so that the probability of finding an electron in the volume of infinite space is equal to unity (normalization condition), continuous and single-valued.

Time evolution of the wavefunction $\Psi(r,t)$ is described by the Schrödinger equation one of the most important equations in quantum mechanics:

$$i\hbar \frac{\partial \Psi}{\partial t} = \hat{H} \Psi \quad (2.1)$$

The operator \hat{H} is the Hamiltonian operator of the total energy of a system. The Schrödinger equation can be written also as:

$$E\Psi = \hat{H}\Psi \quad (2.2)$$

where E represents the total energy of the system and is the eigenvalue of the eigenfunction Ψ . The typical Hamiltonian operator for all electrons and nuclei has following energy contributions:

$$\hat{H} = T_e + T_N + V_{eN} + V_{ee} + V_{NN} \quad (2.3)$$

where:

T_e - the kinetic energy of the electrons

T_N - the kinetic energy of the nuclei

V_{eN} – the Coulomb attraction between electrons and nuclei

V_{ee} – repulsion between electrons

V_{NN} – repulsion between nuclei

To obtain the energy of a system corresponding to its given wavefunction Ψ , one needs to calculate the expectation value of its Hamiltonian and divide it by its norm:

$$E = \frac{\langle \Psi | \hat{H} | \Psi \rangle}{\langle \Psi | \Psi \rangle} \quad (2.4)$$

As the wavefunction must be normalized, the denominator becomes one so $E = \langle \Psi | \hat{H} | \Psi \rangle$. The expectation value of the Hamiltonian for Ψ_0 is called the ground state energy of the system E_0 . If the wavefunction used to describe the system is exact the value of E is also exact and the lowest possible. However, for approximated wavefunctions, values of E will be always higher. The more accurate wavefunction is used, the lower and more accurate energy can be achieved (moving towards the exact value of the energy). The quality of the wavefunction will be the limiting factor for the obtained energies. This theorem is one of the central postulates in quantum mechanics and it is called the variational theorem. The proof of this theorem is widely presented in the literature and will not be described here [3].

The total electronic wavefunction Ψ also has to be antisymmetric with respect to the change of coordinates of any two electrons, which means that the probability of finding an electron should remain the same due to the normalisation condition of the wavefunction [4]. Antisymmetry can be achieved by constructing the wavefunction as a Slater Determinant (SD):

$$\Psi = N!^{-\frac{1}{2}} \begin{pmatrix} \phi_1(1) & \phi_2(1) & \dots & \phi_N(1) \\ \phi_1(2) & \phi_2(2) & \dots & \phi_N(2) \\ \vdots & \vdots & \ddots & \vdots \\ \phi_1(N) & \phi_2(N) & \dots & \phi_N(N) \end{pmatrix} \quad (2.5)$$

where N is the number of electrons and ϕ is a spin-orbital.

The antisymmetrized product of a SD can also be represented as:

$$\Psi = N!^{-\frac{1}{2}} A\phi_1(1)\phi_2(2)\dots\phi_N(N) \quad (2.6)$$

where:

The antisymmetrizer, A , is:

$$A = \frac{1}{N!} \sum_{\hat{\pi} \in S_N} \varepsilon_{\pi} \hat{\pi} \quad (2.7)$$

ε_{π} - sign of permutation

π - permutation operator

S_N - symmetric group

Even though the Schrödinger equation can be used to calculate almost every property of a given system, solving it can be very complex. It can be solved exactly only for 2 particles (hydrogen atom) and certain potentials such as the particle in a box problem. Every system has a different Hamiltonian so the Schrödinger equation will be unique for different systems. To calculate a required property, the equation has to be divided into smaller ones dependent on only one dimension, and solved separately. The final wavefunction of the system can be obtained by direct product of the wavefunctions obtained from these smaller equations. However, apart from the small systems mentioned before, the Schrödinger equation for most systems can get very complex and cannot be separated into decoupled equations thus one needs to use some approximations.

The time-independent version of Schrödinger equation is crucial for the Born-Oppenheimer approximation which is one of the most important approximations in computational chemistry and is applied for the description of the wavefunction for many molecules [3, 4]. However, for systems in which nuclear and electronic motions couple it fails. Such phenomena occur very often in the photochemistry of polyatomic molecules especially involving transition metal atoms due to a large number of energetically close-lying electronic states and the surface crossings or conical intersections between them and will have crucial consequences in the photochemistry of such systems. Examples of which will be presented in this thesis. In the modern derivation of the BO approximation the coupling between the nuclei and electrons depends not only on the mass-difference, but also crucially on the energy difference between electronic states. At points of exact degeneracy the approximation completely breaks down.

Because the nuclei are much bigger than electrons (about 1832 times for the lightest nucleus, i.e., the proton) they move much more slowly. That is why the motion of nuclei can be considered as separate from the motion of electrons. The Born-Oppenheimer approximation keeps the nuclei fixed on the time scale of electron movement so electronic motion is not affected by nuclear motion.

The BO approximation is very well described in the literature [2-5]. To outline its concept one has to solve the time-independent Schrödinger equation.

$$E\psi = \hat{H}\psi \quad (2.8)$$

In the first step of the Born-Oppenheimer approximation the kinetic energy operator for the nuclei is neglected and the repulsion between the nuclei is considered as a constant, which has no effect on the operator eigenfunctions because it adds only a constant value to the eigenvalues of the operator. So after the introduction of the approximation the electronic Hamiltonian operator becomes:

$$\hat{H}_e = T_e + V_{eN} + V_{ee} \quad (2.9)$$

The full solutions of the so-called electronic Schrödinger equation ($\hat{H}_e\psi_e^i = E_e^i\psi_e^i$) are the electronic wavefunctions:

$$\psi_e^i = \psi_e^i(r_i; R_A) \quad (2.10)$$

which depends explicitly on the position vector of electrons and parametrically (as the electronic energy $E_e^i = E_e^i(r_i; R_A)$) on the position vector of nuclei, r_i and R_A respectively.

The total energy E_T for fixed nuclei includes the electronic part of the energy, and the (constant) potential energy of nuclear-nuclear repulsion [2]:

$$E_T = E_e + V_{NN} \quad (2.11)$$

If the nuclear configuration varies over some range of coordinates R , and the electronic Schrödinger equation is solved at each geometry for the electronic wave function, one obtains the potential energy surface on which the nuclei move. The nuclear Hamiltonian for motion in the field of electrons is then:

$$\hat{H}_N = T_N + \langle T_e + V_{eN} + V_{ee} \rangle + V_{NN} \quad (2.12)$$

$$\hat{H}_N = T_N + E_e(R) + V_{NN} \quad (2.13)$$

$$\hat{H}_N = T_N + E_T(R) \quad (2.14)$$

and the solution to the nuclear Schrödinger equation describing the vibrational, rotational and translational states of a molecule is:

$$\hat{H}_N \psi_N = E \psi_N \quad (2.15)$$

$$\psi_N = \psi_N(R) \quad (2.16)$$

So the total wave function for BO approximation can be written as a product of nuclear and electronic terms:

$$\psi(r; R) = \psi_e(r; R) \psi_N(R) \quad (2.17)$$

The Born-Oppenheimer approximation is valid for many chemical processes but as mentioned before there are some important cases when it breaks down. The coupling between electrons and nuclei is one such cause. In the modern mathematical derivation of the BO approximation the total wavefunction is written as a linear combination of the products of electronic and nuclear functions (rather than the single term in equation 2.17 above). This leads to the standard BO equations, plus terms which couple the electronic states via the nuclear momentum. Such derivative coupling can be expressed by the so-called nonadiabatic coupling operators $\hat{\Lambda}_{ij}$, which are mass dependent [6]:

$$\hat{\Lambda}_{ji} = \delta_{ji} \hat{T}_N - \langle \psi_j | \hat{T}_N | \psi_i \rangle \quad (2.18)$$

$$\hat{T}_N = -\frac{1}{2M} \nabla^2 \quad (2.19)$$

where:

$\nabla^2 = \nabla \cdot \nabla$ - Laplacian operator

M - suitable mass-scale.

The derivative coupling vector depends on the energy gap between the states:

$$\hat{\Lambda}_{ij} = \langle \psi_i | \nabla \psi_j \rangle = \frac{\langle \psi_i | (\nabla \hat{H}_e) | \psi_j \rangle}{V_j - V_i} \quad \text{for } i \neq j \quad (2.20)$$

where i, j label electronic states, V_i and V_j is the electronic energy of the i -th and j -th state, respectively. The derivative coupling vector together with the gradient difference vector create the ‘branching space’ around the point of a conical intersection, which will be described later on. If the difference in energy between the electronic states of a given molecule is very small or 0 (they lie very close to each other or are degenerate) they can couple (i.e., the RHS of equation 2.20 is large, (infinite at a degeneracy)), one can no longer describe the motion of nuclei and electrons separately. The BO approximation therefore breaks down and this coupling is called vibronic coupling. Such strong coupling therefore occurs near crossings between potential energy surfaces, i.e., conical intersections and it is these that provide a pathway for ultrafast interstate crossing and Jahn-Teller distortions, which will be described later in this chapter. The theory behind vibronic coupling is very complex and its description can be found in the literature [7, 8].

2.2. Electronic structure methods.

This section will introduce the main computational methods used in this thesis. Electronic structure methods can be divided into *ab initio* methods (from the beginning), semi-empirical methods, and density functional theory [3, 5]. Their basic concept is to describe the motion of electrons in atoms and molecules.

2.2.1. Hartree-Fock theory.

A central method in *ab-initio* quantum chemistry, which was developed to solve the electronic Schrödinger equation, is Hartree-Fock theory. It uses the Born-Oppenheimer approximation discussed before and states that the motion of each electron can be described by a single electron wavefunction called a molecular orbital (MO), which is a product of a spatial orbital and its spin function (spin-orbital). It describes how an electron behaves in the mean field of the other electrons. A molecular spin-orbital can be written as a linear combination of the atomic orbitals (AOs) φ_i (also called basis functions and referred to as the one-electron basis set):

$$\psi_{\mu} = \sum_i c_{\mu i} \varphi_i \quad (2.21)$$

Hartree-Fock theory assumes that the electronic wavefunction can be written as an antisymmetrized product of MOs. Applying the variational principle to the Hartree-Fock wavefunction, the Hartree-Fock energy E_{HF} is minimised with respect to changes of spin-orbitals (optimization of the orbitals), which are used to build the Slater determinant (SD). The number of MOs x depends on the number of electrons present in the molecule (x MOs correspond to at least $2x$ electrons in the case of closed-shell molecules - molecules with a completely filled valence shell). The Hamiltonian operator becomes the Fock operator \hat{F} and it depends on the solutions of the single electron wavefunction:

$$\hat{F}\varphi_i = E_i\varphi_i \quad (2.22)$$

where E_i is the spin-orbital energy. Roothaan and Hall in 1951 introduced the basis set to make the integral differential Hartree-Fock equations more easily solvable for many electron systems as the Roothaan-Hall idea of a basis set involves matrixes and these can be solved by using linear algebra [3]. In the Roothaan-Hall scheme expansion

coefficients of the AOs in equation 2.21 are obtained variationally. To calculate these coefficients and energies of each MO one needs to diagonalize the Fock matrix. This requires the presence of initial guess MO coefficients because the Fock matrix must be known. After diagonalisation of the Fock matrix containing an initial guess of orbitals, a new set of coefficients is generated and the whole procedure is repeated until the obtained coefficients are the same as the coefficients obtained after diagonalisation. The whole iterative procedure is called the Self Consistent Field (SCF) procedure and the obtained orbitals are known as SCF orbitals. S.F Boys in 1953 introduced Gaussian Type Orbitals as a factor to further reduce the cost of calculation at the basis set step. These are discussed in the next subsection.

To obtain a complete basis set (the highest accuracy basis set) an infinite number of basis functions needs to be used. However, a complete basis set is not very practical as it is too computationally expensive so mainly incomplete basis sets are being used in computational chemistry. The choice of which depends on the type of atoms forming a particular system and the property that needs to be described. Examples of basis sets commonly used in this thesis will be presented in the next section of this chapter. The Hartree-Fock wavefunction described by a complete basis set is the most accurate wavefunction one can obtain from Hartree-Fock calculations and is called the 'Hartree-Fock limit' [3].

In Hartree-Fock theory instantaneous repulsions between the electrons are ignored so that each electron only feels an average charge distribution due to other electrons. Thus the Hartree-Fock energies are not the exact energies of the system because this method neglects dynamic electron correlation i.e., the instantaneous correlated motion of every electron arising from the exact Coulomb repulsion. Since each electron experiences a mean-field rather than the true repulsion, electron pairs can on average get too close together and consequently the Hartree-Fock energy is too high. The correlation energy (E_{corr}) is often defined as the difference between the exact energy and the Hartree-Fock limit energy,

$$E_{corr} = E_{exact} - E_{HF} \quad (2.23)$$

The way to improve the Hartree-Fock method is to add terms, which allow a correlation between the motions of electrons, i.e., allow electrons to partially occupy other orbitals.

Despite its deficiencies however, the HF method is a good starting point for the development of other *ab-initio* methods. Post HF methods that include correlation are for example Møller-Plesset perturbation theory (MPn, where n is the order of correction), multi-configurational self consistent field (MCSCF), configuration interaction (CI), multi-reference configuration interaction (MRCI) and coupled cluster theory (CC). CC theory has not been one of the main methods used in this thesis, it has only been used sparingly, MRCI and MP perturbation theories have not been used at all so these methods will not be discussed further here. MCSCF and CI methods will be described later in this chapter.

2.2.2. Basis sets.

As mentioned before a basis set (linear combination of AOs) is a set of basis functions, which are used to form the wavefunction of the system. The number of available basis sets has significantly increased over the past few decades thanks to the development of increased computer power. However, one has to be very careful while choosing the proper basis set for a system. Choosing a too small basis set can result in an inaccurately described wavefunction. On the other hand a too big basis set can dramatically increase the cost of calculations and possibly put excessive strain on computational resources. This is why commonly used basis sets nowadays are built up from sets of *primitive* basis functions that are contracted to lower the computational expense (Gaussian type orbitals – GTOs). A more accurate type of basis functions is called a Slater type orbital (STO). Unlike the GTOs, STOs have the correct radial shape but they become very complex and expensive for atoms/molecules with several electrons. Linear combinations of *primitive* GTO basis functions can form an approximation to any STO. This procedure is called basis set contraction and resulting functions are called a contracted GTOs [5]. A number of primitive GTOs included in the contracted GTOs is called the degree of contraction.

An example of a classical minimal basis set (uses the smallest number of basis functions needed to describe an atom) developed by Pople and co-workers is the STO-3G basis in which three Gaussian basis functions are singly contracted to form an approximate STO. What this means is that for each orbital in an atom there is only one basis function, so only the minimum number of basis functions is required (single zeta basis

set). The number of G functions can vary but adding more G functions gives usually very little improvement. An STO basis with 3 Gaussian functions has been a good starting point for most of the elements from the periodic table. To improve the basis set one can double, triple and so on the number of all the basis functions (double zeta basis set, triple zeta basis set, etc.). Doubling the number of basis functions for only valence orbitals is called split valence basis (or sometimes valence double zeta VDZ). The other types of basis sets introduced by Pople and co-workers are k-nlmG basis sets (for example: 3-21G, 4-21G, 6-31G, 6-311G basis sets). The first number k stands for the number of *primitive* GTOs that are used to represent core orbitals. The nml represent the type of splitting of valence functions (nl, for split valence, nlm for triple split valence) and the number of *primitive* GTOs, which represent each splitting. So for example the 6-31G basis is a split valence basis where the core orbitals are a contraction of six *primitive* GTOs and the valence orbitals split into 3 *primitive* GTOs for the inner part of the valence orbitals and 1 primitive GTO for outer part of the valence orbitals.

If a given basis set is supplemented by one or two ‘plus’ signs (usually added before G), it means that there are diffuse functions added (one plus stands for an extra s and p diffuse function for heavy elements, two pluses means a extra s function on hydrogen). These basis sets can be also supplemented with one or two asterisks that are called polarization functions (usually added after G). Polarization functions allow the wavefunction for more flexibility and can be written in brackets instead of asterisks in the following way: 4-31G(d), 4-31G(d, p) meaning extra set of d functions on heavy atoms, or extra set of d functions for all the atoms excluding hydrogen and extra set of p functions for hydrogen respectively.

The development of correlation consistent basis sets has had a crucial impact on modern computational chemistry and has allowed for moving closer towards the basis set limit (complete basis set). There are split-valence basis sets i.e. cc-pVDZ, cc-pVTZ..., developed by Dunning and co-workers (correlation consistent polarized Valence Double/Triple/...) in which the valence orbitals are described by two or more contractions. These basis functions are especially popular with methods that include electron correlation. If one needs to include diffuse functions, the prefix “aug-“ has to be added. There is also a large number of correlation consisted basis sets introduced by

Peterson and co-workers [9] including all-electron correlation consistent basis sets for first row transition metals [10].

There are also basis sets implemented specially for heavy atoms and they are called Effective Core Potential basis sets (ECP) [5]. Due to the high number of electrons and so number of functions needed to describe those elements the core electrons and their basis functions are replaced with a pseudo potential. Only the valence orbitals are treated at a high level. Core orbitals are replaced by the approximate functions, very cheap to compute. They can be used to describe the relativistic effects in the heavy atom, which are connected with the core electrons. Examples of such basis sets are the LANL2DZ basis set also called Los Alamos National Laboratory 2-double zeta basis set and its variations, the Stuttgart-Dresden pseudopotentials (SDD), and the Stuttgart relativistic large or small core ECP basis sets due to Preuss (STRLC, STRSC). SDD basis sets will be used very often in this thesis due to its suitability for transition metal atoms and other heavy element problems.

2.2.3. Multi-Configurational Self Consistent Field methods – MCSCF.

As mentioned before the Hartree-Fock method neglects the instantaneous correlation between all the electrons that comes from the Coulombic repulsion between electrons. Instead, each electron is treated as if it was moving in a mean field of other electrons and the repulsion between them is averaged. The energy of the system will then be too high because the electrons are able to move to close than they should to each other. However, to obtain a lower energy of the system dynamic electron correlation needs to be included. It is especially important for the transition metal systems, which usually require correlation for qualitative results due to the large number of close lying excited states and for the systems that exhibit Jahn-Teller distortions. Jahn-Teller distortions will be described later in this chapter. The Hartree-Fock wavefunction is constructed as a single SD containing a set of one electron MOs and it can describe only a single configuration within a basis set. One way to describe the energy of the system better is for all possible configurations to be included thus the wavefunction needs to be represented as a linear combination of multiple SD as in equation below [5]:

$$\Psi = c_0\Psi_{HF} + c_1\Psi_1 + c_2\Psi_2 + \dots \quad (2.24)$$

One of the common extensions of Hartree-Fock theory that does this is configuration interaction (CI). The wavefunction is built as a linear combination of many Slater determinants, and is created by the mixing of many-electron wave functions obtained from different electronic configurations, generated by exciting electrons from occupied orbitals to virtual orbitals. A viable CI model can be obtained by limiting the CI expansion to only specific excitation levels (single excitations – CIS, single and double excitations – CISD...) as a full CI (FCI) is too expensive for all but the smallest of systems. CI method includes so called non-dynamic (static) correlation, which is a common feature of MCSCF methods and accounts for more than one electronic configuration at the same time in a balanced manner.

By including all possible N-electron excitations one obtains the Full-Configuration Interaction (Full-CI) method, which is the best calculation possible in a given basis set. However, this method is very expensive and the total number of possible SD is given by the binomial coefficient [3]:

$$\binom{K}{N} \equiv \frac{(K)!}{(K-N)!N!} \quad (2.25)$$

where:

K – total number of Hartree-Fock spin-orbitals

N – number of electrons

Full CI calculations can be performed only for small systems. For larger systems calculations can get extremely expensive and not practical because of the high number of determinants that need to be generated.

In the CI method discussed above the initial HF orbitals are kept fixed in the CI expansion, however a class of methods have been developed where the orbitals are optimized for the CI wavefunction rather than the HF one. The most popular variant of the MCSCF method that does this is the Complete Active Space Self Consistent Field method (CASSCF). Molecular orbitals which build the wavefunction are optimized in addition to the CI expansion coefficients. Hartree-Fock orbitals can be taken as an initial guess, but will invariably be different after convergence of the wavefunction. Here the molecular orbitals which build the wave function are divided into active and inactive ones and are chosen manually, dependent on the studied system. CASSCF

introduces the correlation between the active electrons in active orbitals by performing a Full CI amongst them (Figure 2.2.). It is necessary in CASSCF to optimize AO coefficients because the CI is performed only in the active space. By doing this one can be sure that the obtained energy will be the lowest possible for a given active space, and also ensures that the optimized molecular orbitals are flexible enough to describe the entire potential energy surface.

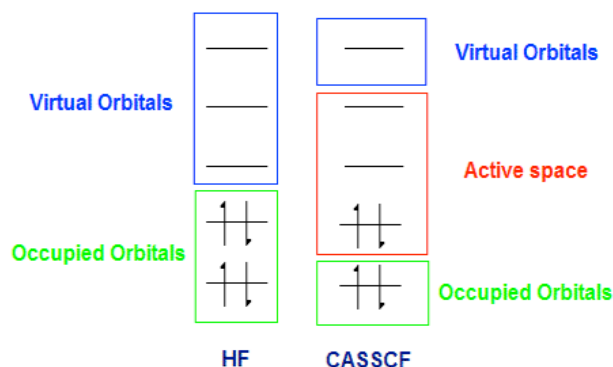


Figure 2.2. Comparison of the molecular orbital partitions in the single-configurational Hartree-Fock method and multi-configurational CASSCF [5].

For systems in which the multi-configurational character of the wavefunction is crucial (systems included in this thesis), HF theory guess orbitals may not be accurate enough. Building the CASSCF wavefunction starting from an incorrect wavefunction may give false or inaccurate results. Thus, the most efficient way to get the multideterminantal nature of the wavefunction is to use so called natural orbitals (NO) that diagonalize the density matrix and its eigenvalues are the occupation numbers of the orbitals. The occupation number is the number of electrons in each natural orbital and it is a real number between 0 and 2. For occupied orbitals occupation numbers are usually close to 1 or 2 and for unoccupied orbitals close to 0. The occupation numbers of orbitals that have to be included in the active space need to be different from exactly 0 or 2. An RHF wavefunction gives occupations of exactly 0 or 2 because of the lack of the electron correlation. UHF natural orbitals can be used as an alternative because they provide fractional occupation numbers [3].

In the case when all valence electrons will be chosen for the active space one can obtain an extremely accurate description of the wave function. However it is possible only for small systems for the same reason as Full CI computations. For large molecules (e.g.,

coordination compounds) where the active space may only contain some of the valence electrons the CASSCF method can overestimate the properties of the system studied; that is why the choice of correct orbitals is crucial for this method. The most important advantage of this method is that it can be used to describe conical intersections, and any multi-configurational states involved. The only limitation of this method is the number of the active space. The maximum active space one can be routinely applied nowadays is around 15 electrons in 15 orbitals (about 1.5 billion different configurations).

There is also a variation of the CASSCF method called Restricted Active Space Self Consistent Field (RASSCF). The orbitals are divided in three spaces RAS1, RAS2 and RAS3 (Figure 2.3) [11]. They have a restricted number of allowed excitations. RAS1 corresponds to doubly occupied orbitals and the RAS3 consists of empty orbitals. There is a full CI performed in the RAS2 space. Additional configurations can be generated by allowing for example a maximum of 2 electrons to be excited from the RAS1 space, and maximum 2 electrons to be excited into the RAS3 space, from the RAS2 space. The main concept of the RASSCF method is to generate configurations by combination of full CI, but in a small space RAS2 (which reduces the cost of calculations), and CISD in a larger space (RAS1, RAS3).

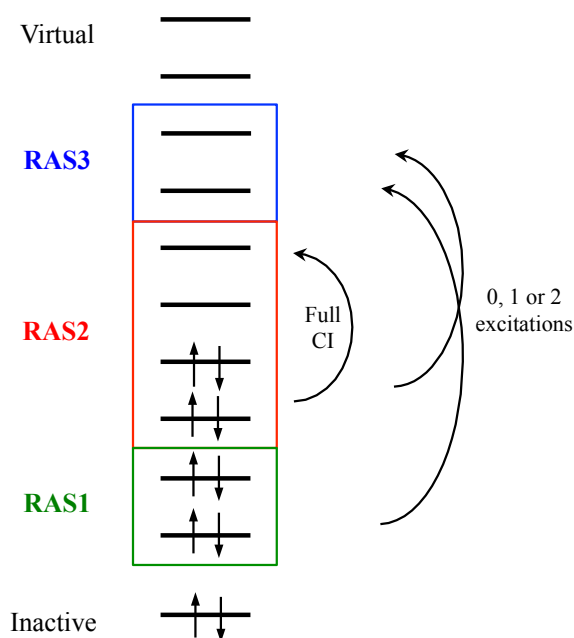


Figure 2.3. Orbital partitions in RASSCF method (picture reproduced from Reference [3]).

2.2.4. Density Functional Theory (DFT).

A wavefunction is dependent on three spatial and one-spin variables for each electron ($4N$ variables where N is the number of electrons), and its complexity increases exponentially with the number of electrons in the system. This puts pressure on the development of alternative methods that would be computationally less demanding than wavefunction methods. DFT theory describes an interacting system via its electronic density rather than a many-body wavefunction [3, 5, 12]. The electrons interact with each other and are influenced also by the external potential. Unlike the wavefunction, the electronic density $\rho(r)$ is a measurable quantity (X-ray diffraction) and it is dependent only on three spatial variables. Integrated over all space gives the total number of the electrons in the system:

$$N = \int \rho(r) dr \quad (2.26)$$

The electron density is independent of the size of the system, which makes it much less expensive and still very accurate. The electronic density also determines the positions of the nuclei, which are the cusps in the density, and the heights of these cusps correspond to the nuclear charges. The main obstacle in DFT is to connect the electronic density with the energy it represents. This is done by the design of a proper electronic density *functional*, which obtains the energy from a function that represents the electron density (a function of a function). Unfortunately, it is not that trivial and the *functional* that would represent the exact energy of the ground state is still unknown. The first attempts to design the correct functionals were in the early nineteen twenties (Thomas-Fermi DFT) and failed to an extent. In 1964 Hohenberg and Kohn, through their existence and variational theorems helped to develop DFT into the form it is used today. They proved that the wavefunction can be replaced by an electronic density and that the variational principle can also be applied in DFT. A breakthrough occurred in 1965 when Kohn and Sham suggested considering the system of electrons as non-interacting. The Hamiltonian operator would then be represented by sum of one-electron operators whose eigenfunctions are Slater determinants. The ground state electronic energy of the real system E_R is the sum of the electron kinetic energies of the system T , the nucleus-electron attraction potential energies V_{eN} and the electron-electron Coulombic repulsion energies (Equation 2.27).

$$E_R = T + V_{eN} + J \quad (2.27)$$

The total energy of the system is then a sum of E_R and E_{xc} . The exchange correlation energy term E_{xc} accounts for the difference in kinetic energy of the real (interacting electrons) and fictitious (non-interacting electrons) systems and contribution from instantaneous electron-electron interactions:

$$E_{xc} = (T - T_S) + (E_{ee} + J) \quad (2.28)$$

$$E_{DFT} = T_S + E_{Ne} + J + E_{xc} \quad (2.29)$$

where:

T_S - kinetic energy of non-interacting system

T - exact kinetic energy

E_{Ne} - Coulombic attraction between the nuclei and electrons

J - Coulombic repulsion between electrons

E_{ee} - repulsion between electrons

Orbitals in the Kohn-Sham approach need to be reintroduced, thus the number of variables increases to $3N$ rather than only 3. The electron density can then be determined from the Kohn-Sham orbitals. They are represented by one-electron spin orbitals, and allow for mapping the kinetic energy and density.

$$\rho(r) = \sum_{i=1}^N |\psi_i|^2 \quad (2.30)$$

The wavefunction then can be described by the Kohn-Sham equations, which are as follows:

$$\{T_S + E_{Ne} + J + V_{xc}\} \psi_i(r_i) = \varepsilon_i \psi_i(r_i) \quad (2.31)$$

where ε_i is the energy of i^{th} Kohn-Sham orbital and the exchange correlation potential V_{xc} is a derivative of the exchange correlation energy mentioned before:

$$V_{xc}(\rho) = \frac{\delta E_{xc}(\rho)}{\delta \rho} \quad (2.32)$$

To solve the Kohn-Sham equations an iterative SCF procedure as previously described for HF theory needs to be applied. Kohn-Sham orbitals obtained in this way are used to determine the electronic density and then the energy. DFT is an exact theory, however because the form of the exchange-correlation term is not known exactly approximate functionals are used to obtain the approximate energy of the system. There are different ways to account for the exchange correlation term but there is no systematic way to improve one functional over another. This is unlike wavefunction-based methods where one can improve the method systematically so it approaches the full CI limit. For DFT this is not the case and some functionals commonly used will be presented below.

In the Local Density Approximation (LDA) to the exchange-correlation energy functional, the density is treated locally as an uniform electron gas – a local dependence of the correlation functional on the density. Popular functionals include VWN (Vosko, Wilk and Nusair), VWN5, or SVWN (including Slater exchange) [13]. These methods will not be described here in more detail because they were not used in this work.

In the Density Gradient approach, the correlation functional is dependent on the local value of the density and also its gradient. This approximation is called generalized gradient approximation (GGA) and common exchange functionals are B (Becke) [14], PBE (Perdew, Burke and Ernzerhof) [15, 16], S (Slater exchange) [17-19], O [20, 21], mPW (Perdew and Wang) [22], G96 [23, 24] and the correlation functionals P86 (Perdew 86) [25], PW91 (Perdew and Wang 91) [26-28], LYP (Lee, Yang, and Parr) [29, 30], and PBE [15, 16]. A very common functional that connects GGA exchange and GGA correlation is BLYP, a combination of Becke's exchange with the correct asymptotic behavior of the density at long range and Lee, Yang and Parr correlation in which the correlation energy is computed entirely. The BP86 functional has the same exchange correction as BLYP and uses the Perdew86 correlation functional.

Hybrid methods called also adiabatic connection methods (ACM) are very common and they incorporate different kinds of methods as LDA, GGA and also HF exchange. They include, apart from a big fraction of total exchange energy, the difference in total and exact HF exchange. Hybrid functionals used in this research will be briefly presented. B3LYP (Becke 3-parameter Lee Yang Parr) is perhaps one of the most commonly used functionals because of high accuracy (1.3 kcal mol⁻¹) of the results compared with

experiment [31]. It uses the non-local correlation of LYP, and local correlation of the VWN functional III. The B3PW91 is a variation of B3LYP and includes non-local correlation by Perdew and Wang 91. The PBE1PBE functional implemented by Adamo and co-workers includes 25% exchange and 75% correlation [32]. The M06 functional (parametrized for both nonmetals and transition metals) and its variations M062HF (with HF exchange) [33], M06-2X (double amount of exchange 20% HF) were implemented by Truhlar and Zhao [34]. The HCTH group of functionals developed by Handy and co-workers include gradient-corrected correlation (HCTH93, HCTH147 etc.) [35-37].

Long-range corrected functionals are very popular for spectroscopic studies because they involve long-range correction to the energy allowing excitations of the electrons to the high lying orbitals. The CAM-B3LYP functional implemented by Handy and co-workers [38] is one of them, specially designed for charge transfer excited states and used with time dependent DFT (TD-DFT) that will be described below. Other examples of such functionals involve LC-wPBE [39-42], wB97XD [43], wB97 [44] and their variations. Long-range corrections can also be added to pure functionals.

An extension of DFT that can be used for excited state determination is called Time-Dependent Density Functional Theory (TD-DFT). No one has yet developed a functional for TD-DFT (i.e., a functional of both the density and the time). Thus TD-DFT currently uses the stationary density (temporally adiabatic approximation), and instantaneously switches on a time dependent field as a perturbation, then uses methods of response theory to determine the first-order response of the density matrix to the perturbation [45]. The TD-DFT eigenvalue equation is in the form:

$$\begin{pmatrix} \mathbf{A} & \mathbf{B} \\ \mathbf{B} & \mathbf{A} \end{pmatrix} \begin{pmatrix} \mathbf{X} \\ \mathbf{Y} \end{pmatrix} = \omega \begin{pmatrix} 1 & 0 \\ 0 & -1 \end{pmatrix} \begin{pmatrix} \mathbf{X} \\ \mathbf{Y} \end{pmatrix} \quad (2.33)$$

where:

\mathbf{X}, \mathbf{Y} – first order change of the density matrix, essentially the perturbed density in terms of mixing of occupied and unoccupied MOs; excitation vectors

- A** – essentially orbital energy differences, plus an exchange integral between occupied and unoccupied MOs
- B** – coupling matrix
- ω – frequency of the perturbation

A and **B** are called orbital rotation Hessians and the vectors **X** and **Y** are defined in the Hilbert space of occupied and unoccupied MOs. These MOs are solutions of Kohn-Sham equations described above and give the importance of single-particle hole excitation/de-excitation to the perturbed density. Geometrical properties of excited electronic states are characterised as derivatives of the excited state energy with respect to an external perturbation [46]. TD-DFT is a good alternative to perturbation theory for systems with between 20 to 200 atoms. Analytical gradients are now possible using the TD-DFT method allowing for a description of excitation and relaxation of two different isomers on particular excited electronic potential energy surfaces (PES) [46, 47]. Note that such optimisation is only appropriate when the ground state reference can be written as a single Kohn-Sham determinant i.e. not near points of degeneracy.

The excitations, which are printed in a TD-DFT calculation, are so called vertical excitations, which are described by the Franck-Condon principle (Figure 2.4) that estimates the probabilities of electronic transitions of different vibrational levels. The system is excited from the lowest vibrational level of its lowest electronic state. Since the nuclear masses are much higher than electronic masses (as described for the Born-Oppenheimer approximation in chapter 2) it is assumed that the system does not change very much during this absorption process and the electronic excitation happens within the nuclear configuration of the molecule (without a nuclear change). Thus the most probable excitations are vertical excitations and the resulting state is called a Franck-Condon state [2]. In the quantum mechanical picture the intensity of the vibronic transition will be proportional to the square of the overlap integral between the vibrational wavefunctions of the two states involved in this transition.

After the transition the system may access different vibrational levels on the excited PES due to the fact that it starts to vibrate. The energy difference between the lowest vibrational level on the ground state PES and the lowest vibrational level on the excited PES is called the adiabatic excitation energy (Figure 2.4).

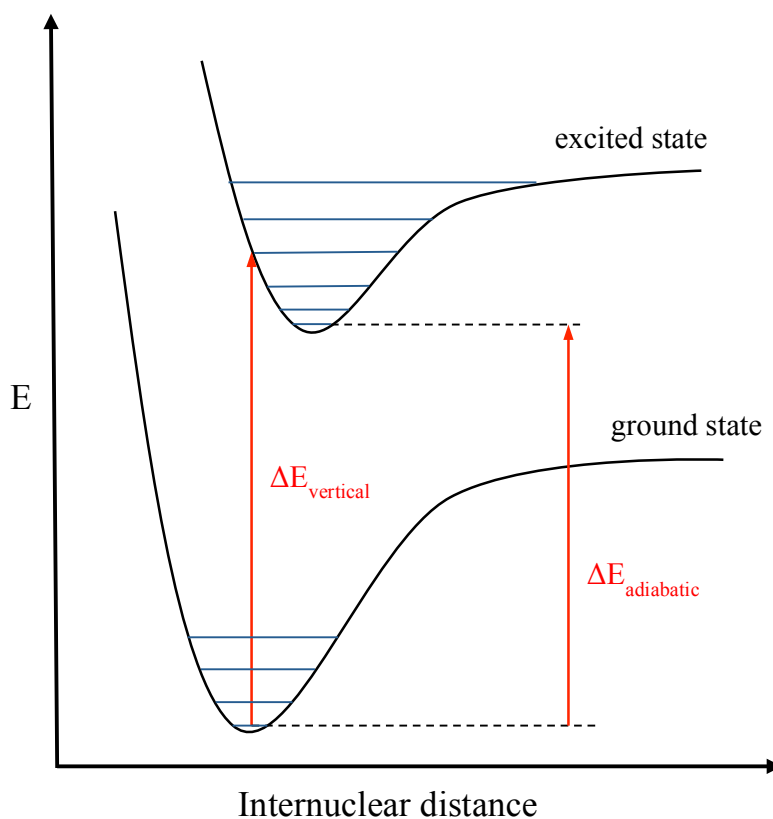


Figure 2.4. The Franck-Condon principle and the relation between vertical and adiabatic excitation energies.

There are many ways to simulate and represent the spectra from computational results. One can use the idea of stick spectra to represent pure electronic transitions. This is perhaps the most honest representation of spectral data but comparison with experiment is more difficult. Although vibronic resolution is neglected here (which would require Franck-Condon factors) the effects of spectral broadening can be simulated. Spectral broadening is a well-known physical phenomena occurring from a variety of sources, including Heisenberg lifetime broadening, collision broadening, Doppler broadening amongst other factors (see reference [48] for details). In this research homogeneous Gaussian broadening was used to generate a continuous spectrum. Each peak in the stick spectra is multiplied by a Gaussian function. Spectral intensity is obtained using the following formula:

$$I(\lambda) = \sum_i f_i e^{\left(-\frac{1}{2} \left(\frac{\lambda - \lambda_i}{\sigma}\right)^2\right)} \quad (2.34)$$

where:

f_i - oscillator strength for different excitations.

λ - particular wavelength from wavelength range

λ_i - wavelength of the transition.

σ - width of the Gaussian, which determines the broadening of spectra, here this is the same for each excitation, thus the broadening is homogeneous.

The oscillator strength is given by [49],

$$f = \frac{2}{3} \omega_{ov} \left| \langle o | \vec{\mu} | v \rangle \right|^2 \quad (2.35)$$

where:

ω_{ov} - frequency of a transition

$\langle o | \vec{\mu} | v \rangle$ transition dipole moment

2.3. Closed vs open shell configurations.

This section is a brief introduction to the concepts of closed and open shell configurations. Thanks to the development of modern hardware and software packages the calculation of the chemical properties of closed shell molecules is now very common. In closed shell systems each molecular orbital (MO) contains a pair of electrons, one spin up α and one spin down β , and the determinant of such MOs is a pure singlet spin function. The wave function represents the ground state of a closed-shell molecule. The spin term describes the intrinsic angular momentum of electrons, α and β are the eigenfunctions of the operator \hat{S}_z [4]:

$$\hat{S}_z \alpha = \frac{1}{2} \hbar \alpha \quad (2.36)$$

$$\hat{S}_z \beta = -\frac{1}{2} \hbar \beta \quad (2.37)$$

where: $\hbar = 1$ au, so the eigenvalues of α and β (s) are equal to $\frac{1}{2}$ and $-\frac{1}{2}$. In a many electron system the maximum value of $\langle \hat{S}_z \rangle = s$, and the possible eigenvalues (M_s) can be written as:

$$M_s = s, s-1, s-2, \dots, -s \quad (2.38)$$

The corresponding spin operator is then defined as having the following expectation value:

$$\langle \hat{S}^2 \rangle = s(s+1) \quad (2.39)$$

In closed shell systems all electron spins are paired so $\langle \hat{S}^2 \rangle = 0$ and the spin state is a singlet. The simplest method for such calculations is Restricted Hartree-Fock theory (RHF), which restricts each spatial orbital to only two electrons, one spin up and one spin down. In open shell systems determinants are eigenfunctions of $\langle \hat{S}^2 \rangle$ only in the case where all paired electrons share the same spatial function (known as restricted open-shell Hartree-Fock (ROHF)). Otherwise the determinants may not be pure spin states. To become eigenvalues of $\langle \hat{S}^2 \rangle$, appropriate linear combinations of these determinants have to be formed.

The other method that deals with open shell configurations is Unrestricted Hartree-Fock (UHF). This uses different spatial orbitals for different spins. The UHF energy is usually lower than ROHF. The advantage of UHF is that it allows for modeling of spin polarization in open-shell molecules, i.e., for a pair of α and β electrons in an orbital, and an unpaired electron in another orbital, the α and β electrons will respond differently to the unpaired electron (manifested in the spatial distribution of the electrons). One of the problems which arise here is spin contamination. This increases with an increasing amount of spin polarization. The $\langle \hat{S}^2 \rangle$ operator evaluates the value of the total electron spin squared, which means that the wave function can also have contributions from the higher spin states that have the same M_S value. To calculate the amount of spin contamination in a system one has to find the expectation value of the $\langle \hat{S}^2 \rangle$ operator, which depends on the spatial overlap between all pairs of α and β spin-orbitals [50]:

$$\langle \hat{S}^2 \rangle = S_z(S_z + 1) + N_\beta - \sum_{ij}^{MO} \langle \psi_i^\alpha | \psi_j^\beta \rangle^2 \quad (2.40)$$

Because of the problems mentioned above for ROHF and UHF methods, which consist of a single electron configuration, they do not give very accurate results for open-shell

problems. Thus, a single configuration description of an open shell state will always have one problem: no spin-polarization for ROHF, and spin-contamination for UHF.

The restricted and unrestricted variants of DFT work a quite similar way but not exactly the same as their HF variants. Restricted DFT is called restricted open-shell Kohn-Sham (ROKS) and unrestricted DFT is called unrestricted Kohn-Sham (UKS). The UKS method is more often used due to the presence of molecules that exhibit spin-polarisation in some regions of space, and ROKS does not reproduce these observations in the same way that ROHF does not [51]. Similarly as in UHF $\langle \hat{S}^2 \rangle$ is calculated for the single Kohn-Sham determinant. The equation for $\langle \hat{S}^2 \rangle$ is exactly the same as in equation 2.40, however it represents the $\langle \hat{S}^2 \rangle_{NI}$ of the non-interacting system. There have been approximations developed to calculate $\langle \hat{S}^2 \rangle$ as an explicit functional of the density such as the exchange local spin density approximation (XLDS) by Wang, Becke and Smith (WBS) [52]. Handy and co-workers presented an alternative way to evaluate $\langle \hat{S}^2 \rangle$ based on a generalized gradient approximation using a formula for $\langle \hat{S}^2 \rangle_{XLDS}$, which turned out to give much lower spin contamination than its analog [51]. It should be noted that this most recent work [51] shows that the spin-state for open-shell DFT is not exactly analogous to HF theory and that further work is required in this area.

MCSCF methods have also found application in this field. One of the best methods here is the CASSCF described above. It provides a good way of dealing with radicals, and by using a multi-configurational wave function it is a good solution for modeling open shell configurations of molecules. By introducing electron correlation between specified active electrons it guarantees that the obtained wave functions are eigenfunctions of \hat{S}^2 . One may build the initial configurations to be eigenfunctions of \hat{S}^2 by taking fixed linear combinations of determinants.

These linear combinations of determinants are called Spin Adapted Configurations. The possible number of such configurations is given by the binomial coefficient below (Equation 2.41).

$$D^{CSF} = \frac{2S+1}{K+1} \binom{K+1}{N/2-S} \binom{K+1}{N/2+S+1} \quad (2.41)$$

where:

K – number of orbitals

N – number of electrons

S - spin

i.e. the number of possible singlet configurations of N electrons in K orbitals will be then determined as:

$$\frac{K!(K+1)!}{(N/2)!(N/2+1)!(K-N/2)!(K-N/2+1)!} \quad (2.42)$$

Let us consider doublet and quartet states of a molecule, which will be important in this research. Taking as an example $\langle \hat{S}_z \rangle = +\frac{1}{2}$, we can form 3 different configurations shown in figure 2.5:

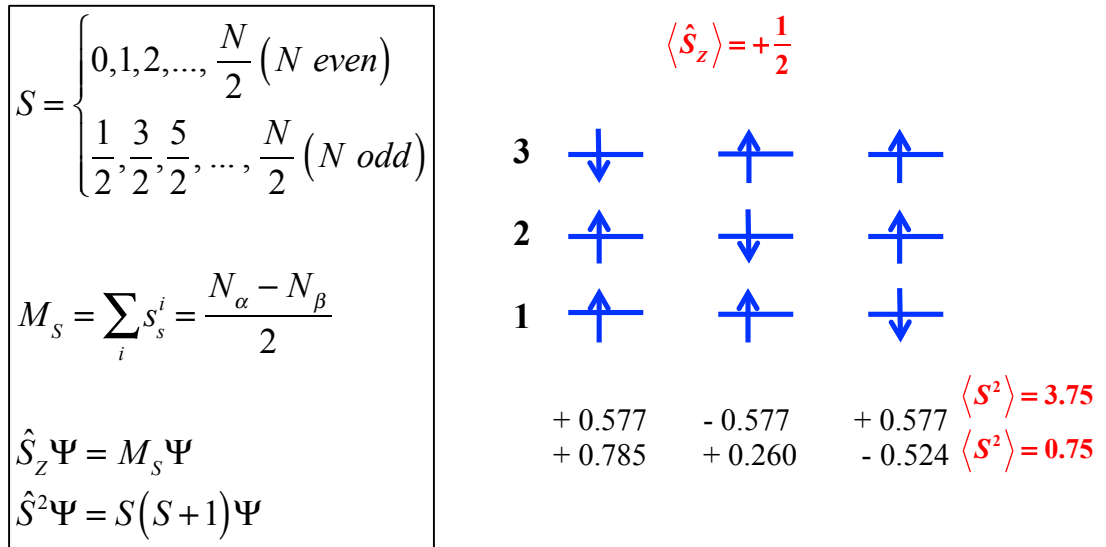


Figure 2.5. 3 electron, 3 orbital Configuration State Functions (CSF) in an $\langle \hat{S}_z \rangle = +\frac{1}{2}$ basis showing both doublet and quartet contributions.

The eigenvalues of the spin angular momentum \hat{S}_z for a the doublet state are $\left(M_s = -\frac{1}{2}, \frac{1}{2}\right)$ and for the quartet state $\left(M_s = -\frac{3}{2}, -\frac{1}{2}, \frac{1}{2}, \frac{3}{2}\right)$. They have common values of $M_s = -\frac{1}{2}, \frac{1}{2}$ thus both states can mix together. Therefore in a single-configuration unrestricted treatment the wavefunction for the doublet would be contaminated with quartet states. In a multi-configurational treatment the resulting eigenfunctions are automatically also eigenfunctions of \hat{S}^2 . If we use determinants, then all determinants of a given M_s can combine to generate the total wavefunction for the correct spin-state, that is the same configurations above can combine to give a doublet state or a quartet state depending on the mixing coefficients. We can however generate a spin-adapted many-electron basis by taking their fixed combinations at the outset. Looking at figure 2.5, we can fix 3 different configurations for the doublet state and treat them as a one-spin adapted-function (CSF), or with differing coefficients we can fix them as a quartet CSF. Note that the computational effort is reduced since the linear expansion coefficients are fixed, and do not need to be variationally optimized. The downside is that we often need to use advanced mathematical methods to build CSFs from a set a determinants. A comparison of both CSFs and SDs in treating an open-shell configuration is presented in table 2.1.

CSF's		Slater Determinants	
Spin-adapted	✓	Not spin-eigenfunctions	✗
Smaller CI expansions	✓	Larger CI expansions	✗
Spin-adaption may be very complex (e.g., Unitary group algebras)	✗	Modern CI codes use Slater Det. Expansions	✓
No interaction between states of different S	✗	States of different S are treated together – prelude for spin-orbit coupling treatment	✓

Table 2.1. Configuration State Functions vs. Slater Determinants - advantages and disadvantages.

The understanding of chemistry of open shell systems is very important in the field of organic chemistry. Mechanisms of many chemical reactions like radical additions,

substitutions or isomerisations, involve the movement of single electrons. The products of such reactions like radical ions are the subjects of many experimental and computational report [53, 54]. This research is focused on the area of chemistry that is dominated by open-shell states which is transition metal chemistry, on which we shall focus on later.

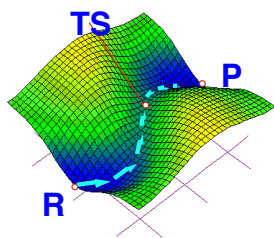
2.4. Potential Energy Surface (PES) crossings.

2.4.1. Conical intersections.

Conical intersections are the subject of many studies in the last 2 decades [55]. They are the crossings between two or more potential energy surfaces of a molecule which provide radiationless decay channels between these surfaces and in turn cause the formation of photoproducts [1]. The determination of excited electronic states nature, mechanisms of photoreaction paths and the molecular structure of the decay is now possible by combining experimental methods like laser spectroscopy with theory. The crucial aspect of conical intersections is that they occur between degenerate states. The degeneracy means that the one eigenvalue is associated with two or more independent eigenfunctions of the Schrödinger equation. It implies Jahn-Teller effects in high-symmetry molecular systems [56], which will be described later.

It was suggested by the Teller, Zimmerman and Milch, that many photochemical reactions can occur through a conical intersection rather than a transition state [57]. The main difference between the two is that a transition state connects the reactants with a single product (Figure 2.6 a)) in a single reaction path (motion along transition vector x_1 (Figure 2.6 b)):

a)



b)

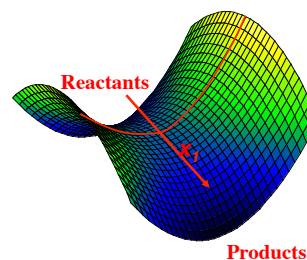


Figure 2.6. Photochemical reaction path through transition state.

A conical intersection can connect the reactants with one or more products on the ground state via many reaction paths (branching of the reaction path in the plane x_1 and x_2 – double cone nature of a CI). The graphical representation of such crossing is presented in figure 2.7:

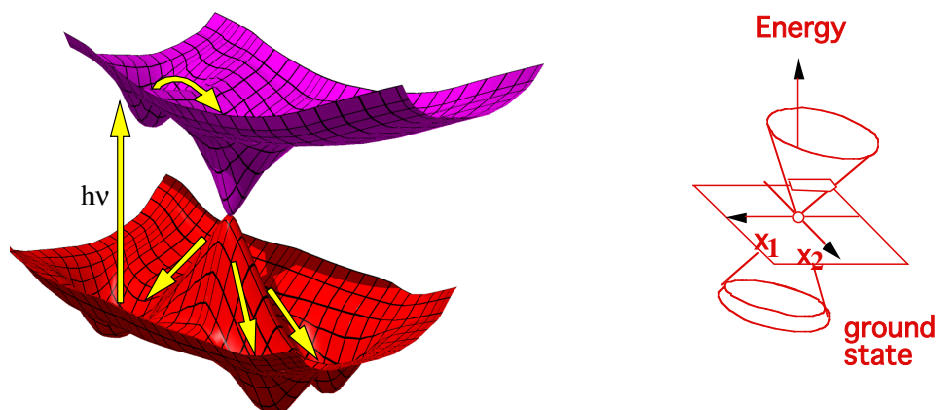


Figure 2.7. Photochemical reaction paths through conical intersection (picture adapted from Reference [55]).

x_1 and x_2 (Figure 2.7) are the gradient difference and gradient of the interstate coupling vectors. They are special internal coordinates which lift the degeneracy:

$$x_1 = \frac{\partial(E_j - E_i)}{\partial q} \quad (2.43)$$

$$x_2 = \left\langle C_1 \left(\frac{\partial \hat{H}}{\partial q} \right) C_2 \right\rangle \quad (2.44)$$

where:

E_j, E_i – energies of states j and i

C_1, C_2 – configuration interaction (CI) eigenvectors

H – CI Hamiltonian

q is a vector of Cartesian displacements.

Thus, x_2 is related to the derivative coupling vector (Equation 2.20). The remaining $n-2$ internal coordinates ($n=3N-6$ – number of vibrational degrees of freedom of a molecule) do not lift the degeneracy, and they are called intersection space, which is a hyperline consisting of an infinite number of conical intersection points (the so-called intersection seam). The photochemical reactivity of a molecule depends on the position and local topology of a conical intersection. A peaked conical intersection happens when both

PES have non-parallel gradients near the intersection (Figure 2.8). A sloped conical intersection occurs when both PES have almost parallel gradients near the intersection (Figure 2.8).

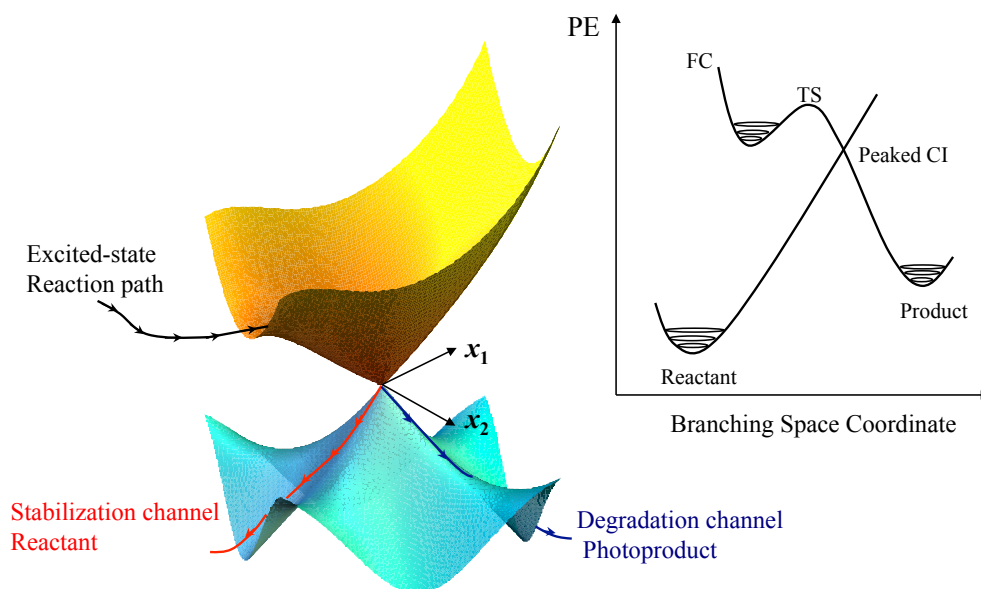


Figure 2.8. Relaxation through a peaked intersection (picture reproduced from Reference [58]).

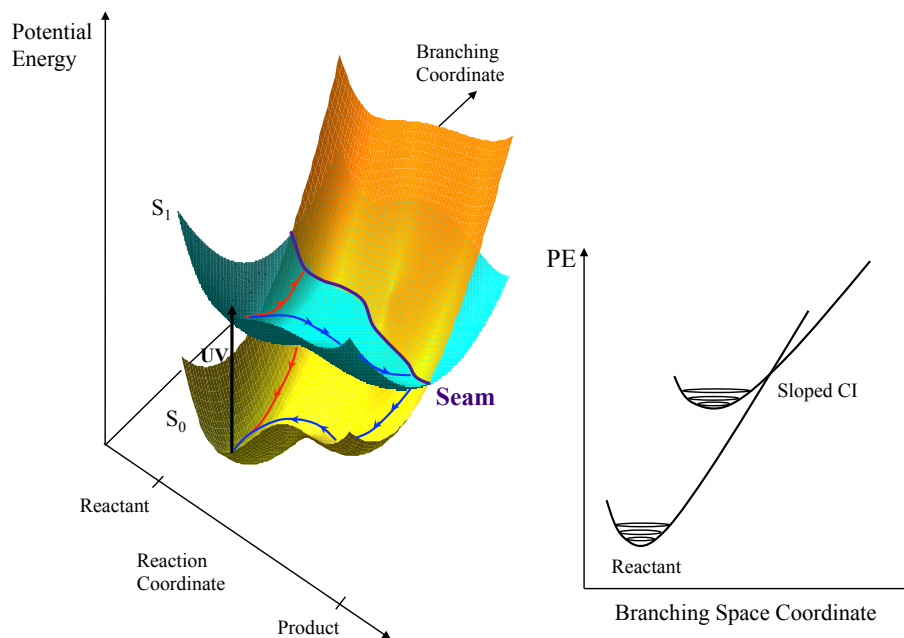


Figure 2.9. Relaxation through a seam of sloped conical intersection (picture reproduced from Reference [58]).

In the case of diatomic molecules two potential energy surfaces can only cross if the states have different symmetries. If they have the same symmetry they rather undergo an avoided crossing (Figure 2.10.).

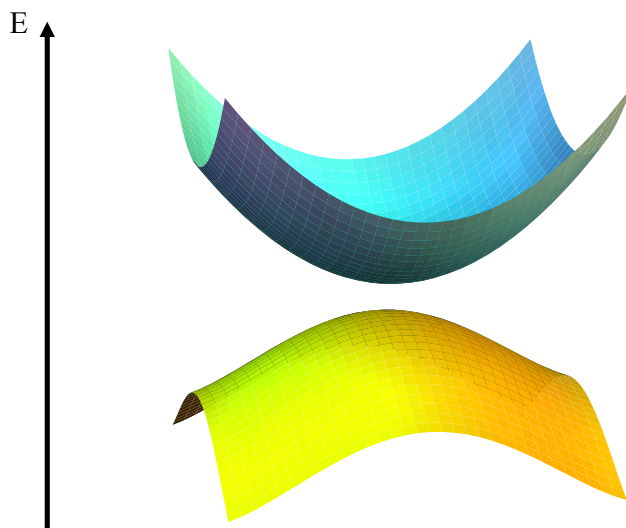


Figure 2.10. Avoided crossing between two electronic PESs.

It is different for polyatomic molecules, the PESs can cross even if they have the same symmetry (a real surface crossing).

2.4.2. Intersystem crossings and spin-orbit coupling effects.

An intersystem crossing is a type of crossing that can occur between two PESs of different spin state. When two electronic states have differing spin-multiplicities the derivative coupling term is zero by symmetry. Therefore the PES cross in a single coordinate, i.e. the gradient difference coordinate ($gd - x_1$). Thus, when the PES are plotted along the gd and any other coordinate they have the appearance of a one-dimensional seam (Figure 2.11).

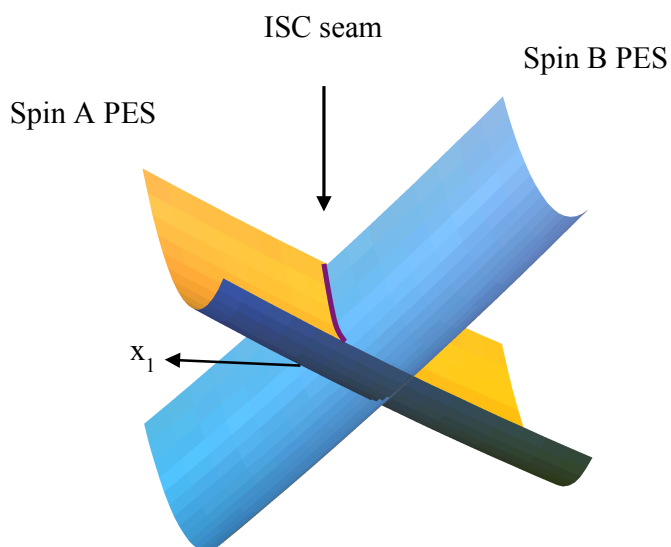


Figure 2.11. Relaxation through an intersystem crossing.

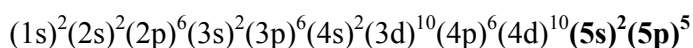
Rather than the non-adiabatic terms coupling different electronic states, here the spin-orbit interaction, which is the coupling between electron spin S and orbital angular momentum L , governs the strength of the coupling. SOC is formally a relativistic phenomenon arising from the Dirac equation of quantum mechanics [3]. The Dirac equation differs from Schrödinger equation in the form of their Hamiltonians, which in the former is much more complicated:

$$H_{Dirac} = (c\alpha \cdot p + \beta mc^2) + V \quad (2.45)$$

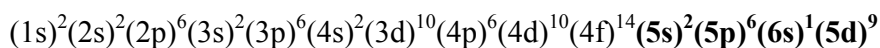
where α and β are 4×4 matrices, that represent large and small components of a wavefunction including α and β spin functions and V is the electric potential. The large component corresponds to a normal non-relativistic wavefunction. The small components correspond to a coupling with positronic states. When the speed of light c goes to infinity these become decoupled and the Schrödinger equation, is returned. The Schrödinger equation is not relativistically correct and for many electron systems a Dirac-Coulomb Hamiltonian may need to be constructed [3].

In the many-electron extensions of the Dirac equation each electron can be described as $(c\alpha \cdot p + \beta mc^2)$ and so additional terms arise which can include the spin-other-orbit, spin-spin, and orbit-orbit interactions. Spin-other-orbit terms describe the interaction of

an electron spin with the magnetic field generated by the movement of the other electrons. Spin-spin and orbit-orbit terms describe additional magnetic interactions [3]. The magnitude of these relativistic effects scales with nuclear charge so that they are extremely important for heavy elements and as such cannot be treated as a perturbation on the non-relativistic wavefunctions and energies. The scalar one-electron relativistic effects on the core orbitals for heavy atoms are most often accounted for using a pseudo-potential, which accounts for the shape and energetics of the core electrons, as obtained from relativistic calculations, but the orbitals and electrons are replaced by a smooth potential in the non-relativistic framework [3, 59-62]. The number of electrons that can be represented as a pseudo-potential can vary. It is common to treat valence electrons explicitly and the remaining core as a pseudo-potential, however, for better results one can also include orbitals from the next lower shell and treat them explicitly. The Stuttgart-Dresden (SDD) pseudo-potential mentioned previously in subsection 2.2.2 of this chapter is an example of such a pseudo-potential and will be used for some calculations in the following chapters. In the chapter 4, for the iodine atom that contains 53 electrons, the SDD potential represents the 46 core electrons, and the 7 remaining valence electrons are treated explicitly.



In the case of the platinum atom that contains 78 electrons, the SDD potential represents 60 core electrons, and 18 valence electrons are treated explicitly.



It should be noted that a pseudo-potential deals with the large magnitude of relativistic effects for the core electrons, while the SOC type of effects important in the case of intersystem crossings deal with much, much weaker interactions coming from the valence electrons. For the first three rows in the periodic table relativistic effects such as valence SOC are usually quite weak.

For lighter elements (including the first row of the periodic table) a perturbative treatment of these relatively weak interactions is most appropriate. The wavefunction of

the state m , that can be perturbed due to the effect of SOC as it mixes with state k , can be written as:

$$\psi_m = \Phi_m + \sum_{k \neq m} a_k \Phi_k \quad (2.46)$$

where Φ_m is pure-spin zero-order wave function for state m , Φ_k pure-spin wavefunction of perturbing state k , and a_k are coefficients that represent the contribution of the individual pure spin-perturbing states to the ground state wavefunction, treated by perturbation theory. Equation 2.47 gives the expression for these coefficients, where $\hat{\mathbf{H}}_{\text{SO}}$ is for example a Breit-Pauli spin-orbit operator, that allows for the mixing of pure spin states (Equation 2.47) [63].

$$a_k = \frac{\langle \Phi_k | \hat{\mathbf{H}}_{\text{SO}} | \Phi_m \rangle}{E_m - E_k} \quad (2.47)$$

E_m and E_k are energies of the states m and k respectively. These terms (Equation 2.46, 2.47) arise from the CI treatment of states described in subsection 2.2.3 of this chapter.

In organic chemistry a further approximation is often invoked whereby the spin-orbit coupling is based upon an empirically scaled one-electron term that for example can give a reasonable description of the mixing of singlet and triplet states of organic molecules. This empirically scaled model has not been extended to the first transition metal series and any evaluation of SOC needs to use the full perturbative model. We note here that when SOC is weak the position of the crossing seams as shown in figure 2.10 is the most important factor in determining whether or not a system changes spin state. For such weak coupling the pure spin-states are valid and the crossing region determines the geometries where the system can change from one spin state to another (i.e. when the denominator in equation 2.47 tends to zero). Thus the SOC can be expected to be reasonably constant over a small geometrical change. For the systems studied later, i.e. open-shell doublet and quartet states, whose photochemistry sometimes involves a spin-state change we will be concerned only with these ISC crossing regions between the pure spin-states. We do not evaluate any SOC as the full perturbative treatment is too expensive for these systems, and also as discussed we expect the SOC to be quite weak and relatively insensitive to geometry, therefore for the

non-radiative spin-changing transition the low energy crossing seams take on the same importance as conical intersections do for spin-conserving radiationless transitions.

One of the manifestations of intersystem crossing can be the radiative process called phosphorescence, which in this thesis will be considered as any general radiative non-spin conserving transition. Thus phosphorescence occurs following a non-radiative ISC from one spin-state to another on a relatively fast time scale, and the phosphorescence is the radiative return to the original spin state on a much larger time scale.

2.4.3. Jahn-Teller effects.

Jahn-Teller effects are closely related to conical intersections. They are molecular distortions of systems which can occur between two or more degenerate electronic states due to some vibronic instabilities [64]. One of the most common Jahn-Teller distortions happens when a doubly degenerate state E , couples with doubly degenerate vibrational mode e (Figure 2.12. a)):

$$E \otimes e \quad (2.48)$$

In the $E \otimes e$ case the gradient difference (x_1) and interstate coupling (x_2) together have e symmetry, Another case of Jahn-Teller distortions happen when doubly degenerate state E is coupled with 2 nondegenerate vibrational modes of b_1 and b_2 symmetry (Figure 2.12. b)):

$$E \otimes (b_1 + b_2) \quad (2.49)$$

In the $E \otimes (b_1 + b_2)$ case the gradient difference (x_1) has b_1 symmetry, and the interstate coupling (x_2) has b_2 symmetry.

Thus, Jahn-Teller PESs are highly symmetrical conical intersection surfaces, and the general case can be thought of as a complete reduction of the Jahn-Teller symmetry relating the vectors of the branching space.

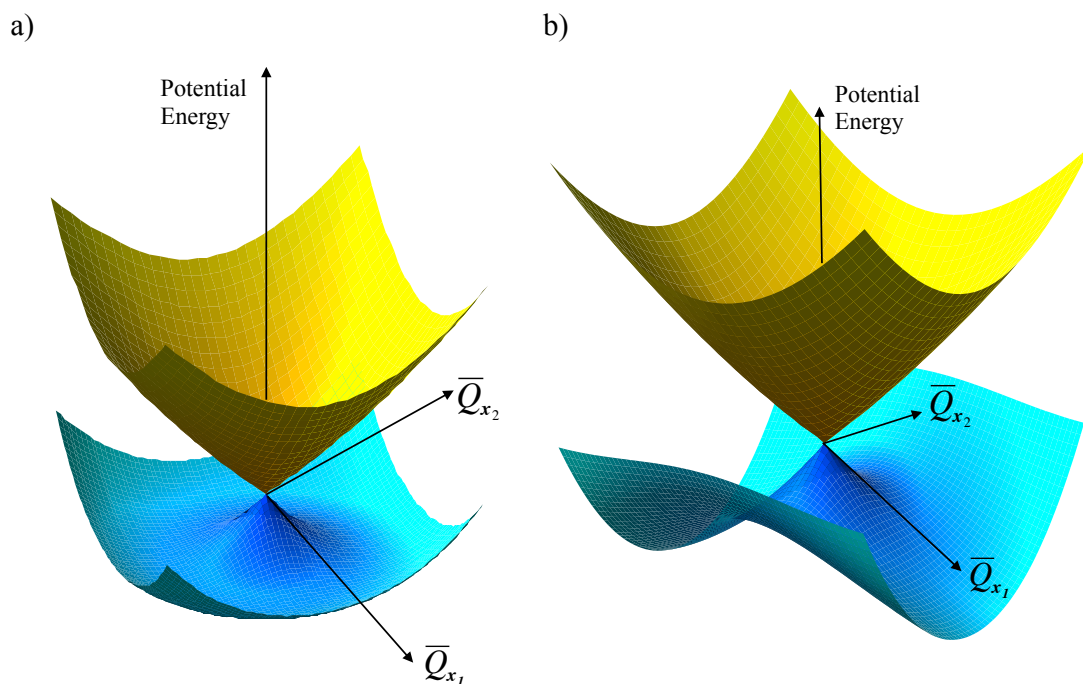


Figure 2.12. Potential energy surfaces shapes in Jahn-Teller distortions (picture reproduced from reference [1]). a) $E \otimes e$ case b) $E \otimes (b_1 \otimes b_2)$

The pseudo Jahn-Teller (pJT) effect is caused by vibronic mixing of the ground state PES with nearby excited states. As a result the geometry at higher symmetry is a saddle point rather than a minimum. It may be accompanied by orbital disproportionation, and the formation of a global minimum can be caused by spin crossover. Orbital disproportionation means that the system leads to lower symmetry by occupying one of the orbitals with two electrons rather than populate all of them with one electron per orbital (Hund's rule for highest spin charge distributions in a half-closed shell) [65]. This aspect of the pJT effect has recently been taken up by Bersuker [66]. The pJT effect will be described in more detail in chapter 3 concerning distortion in the ammonia molecule and the main structural motif of an edge-sharing molybdenum complex.

Understanding the nature of conical intersections and Jahn-Teller effects is crucial in inorganic photochemistry. It is very difficult to determine the geometry of a molecule at the region of a conical intersection by experiment because it spends very little time there. The only way to examine its nature and dynamics is by treating the problem with computational methods and compare the results with experimental findings and this is

addressed in this thesis for some selected TM systems. The process of conical intersection optimisations will be described next.

2.5. Geometry optimisations.

As mentioned in the beginning of this chapter, to locate different stationary points (points at which the first-order derivative is zero i.e. minima, transition states, higher-order saddle points) on PESs, a process of geometry optimisation needs to be performed. To locate a minimum on the PES, the energy and gradients (first-order derivatives – which point in the negative direction to the forces on the atomic nuclei) for initial positions of the atoms of a given system are calculated. Then, the positions of the atoms are moved slightly in the direction of the forces, and the energy calculated again. This step is repeated until the program finds the lowest possible energy for the given system. When this happens the optimisation process is complete. Methods that find the directions in which the gradient is reduced are as follows: steepest descent, which is the easiest to implement and the most popular, conjugate gradient, or Newton-Raphson methods. These methods will not be discussed further here [3, 5]. Unfortunately, stationary points cannot be located exactly, because the gradient can be reduced only to a certain value, which can cause some numerical inaccuracies. In practice for all computational methods the system will be considered as optimised under some convergence limit.

To characterise a stationary point one needs to calculate the Hessian i.e. the matrix of second derivatives. For polyatomic molecules there are $3N-6$ possible vibrational degrees of freedom (normal modes). As mentioned in the beginning of this chapter, at a minimum, all the normal modes of the system which are eigenvectors of the Hessian, have positive eigenvalues. The Hessian eigenvalue is related to the harmonic vibrational frequency for the normal mode. For a first order saddle point i.e. a transition state, there is one negative eigenvalue of a Hessian matrix and for the n -th order saddle point there are n number of negative eigenvalues. Calculating the Hessian can be very expensive for certain electronic structure methods [3] and is discussed later for the CASSCF method in chapter 3.

To locate a transition state (TS) i.e., the maximum energy point along the path on the PES connecting reactants and products, the energy needs to be maximised in the direction of the transition vector (one of the n orthogonal directions – Figure 2.6) and minimised in the remaining $n-1$ directions [55]. Algorithms exist for TS optimisation, but unlike minima, convergence to a saddle-point cannot be sure. These algorithms often require many Hessian calculations making them expensive for correlated methods.

To optimise a conical intersection (i.e., the lowest energy intersection point), the energy needs to be minimised in the $n-2$ directions of the intersection space (x_3, x_4, \dots, x_n) to preserve the degeneracy (Equation 2.50). The two remaining directions, the gradient difference (x_1) and derivative coupling (x_2) vectors, form the branching space vectors, described previously in subsection 2.4.1 (Equations 2.43, 2.44). The energy gap between two states has to be minimised in the direction of the branching space vectors x_1, x_2 and for the optimised point of the intersection the energy difference must be zero (Equation 2.51). Thus, there are two conditions to be met in a conical intersection optimisation [55].

$$1) \frac{\delta E}{\delta x_3} = \frac{\delta E}{\delta x_4} = \dots = \frac{\delta E}{\delta x_n} = 0 \quad (2.50)$$

$$2) E_j - E_i = 0 \quad (2.51)$$

The algorithm used in the Gaussian program for minimisation of energy $E_j - E_i$ (Equation 2.51) in the x_1, x_2 branching space uses the following condition:

$$\frac{\partial}{\partial q} (E_j - E_i)^2 = 2(E_j - E_i)x_1 = 0 \quad (2.52)$$

where x_1 is the gradient difference vector (Equation 2.43), of which the length is not important but the direction. The size of the step is thus dependent on the energy difference between these states and the gradient is taken along the direction where this energy difference becomes a minimum. The gradient at the point of conical intersection is non-zero because of its topology – i.e. the vertex of an inverted cone. It is calculated as a projection of the gradient of E_j along the intersection space seam (i.e., the $n-2$ dimensional hyperline) (Figure 2.9). This goes to zero when the geometry of the conical intersection is optimized. Summing up, the procedure for locating conical intersections

involves finding an initial point on the intersection seam. Then the system moves along the intersection space vectors, until it finds the minimum energy point on the intersection seam.

To characterise a point of conical intersection, i.e. to characterise the optimised point as a minima or saddle point on the seam via the Hessian, is not as straightforward as for a single surface. There are now methods being developed to do this however they will not be discussed further here [67].

2.6. List of references.

- [1] Paterson, M. J.; Bearpark, M. J.; Robb, M. A.; Blancafort, L.; Worth, G. A., Conical Intersections: A Perspective on the Computation of Spectroscopic Jahn-Teller Parameters and the Degenerate 'Intersection Space'. *Phys. Chem. Chem. Phys.* **2005**, 7, 2100-2115.
- [2] Atkins, P. W.; Friedman, R., *Molecular Quantum Mechanics*. 4th ed.; Oxford University Press: New York, 2005; p xiv, 573 p.
- [3] Jensen, F., *Introduction to Computational Chemistry*. John Wiley & Sons: 2007; p 599.
- [4] Attila Szabo, N. S. O., *Modern Quantum Chemistry*. Dover Edition ed.; Dover Publications, INC.: Mineola, New York, 1996; p 466.
- [5] Cramer, C. J., *Essentials of Computational Chemistry*. John Wiley and Sons: 2004; p 596.
- [6] Worth, G. A.; Cederbaum, L. S., Beyond Born-Oppenheimer: Molecular Dynamics Through a Conical Intersection. *Ann. Rev. Phys. Chem.* **2004**, 55, 127-158.
- [7] Sato, T.; Tokunaga, K.; Iwahara, N.; Shizu, K.; Tanaka, K., Vibronic Coupling Constant and Vibronic Coupling Density. In *The Jahn-Teller Effect: Fundamentals and Implications for Physics and Chemistry*, Köppel, H.; Yarkony, D. R.; Barentzen, H., Eds. Springer: Heidelberg, 2009; pp 99-129.
- [8] Poluyanov, L. V.; Domcke, W., Spin-Orbit Vibronic Coupling in Jahn-Teller and Renner Systems. In *The Jahn-Teller Effect: Fundamentals and Implications for Physics and Chemistry*, Köppel, H.; Yarkony, D. R.; Barentzen, H., Eds. Springer: Heidelberg, 2009; pp 77-97.
- [9] Peterson, K. A. Peterson Research Group: Correlation Consistent Basis Sets. <http://tyr0.chem.wsu.edu/~kipeters/basis.html>
- [10] Balabanov, N. B.; Peterson, K. A., Systematically Convergent Basis Sets for Transition Metals. I. All-electron Correlation Consistent Basis Sets for the 3d Elements Sc-Zn. *J. Chem. Phys.* **2005**, 123, 64107.
- [11] Klene, M.; Robb, M. A.; Blancafort, L.; Frisch, M. J., A New Efficient Approach to the Direct Restricted Active Space Self-Consistent Field Method. *J. Chem. Phys.* **2003**, 119, 713-728.

- [12] Koch, W.; Holthausen, M. C., *A Chemist's Guide to Density Functional Theory*. 2nd ed.; Wiley-VCH: Weinheim ; New York, 2001; p XIII, 300 p.
- [13] Vosko, S. H.; Wilk, L.; Nusair, M., Accurate Spin-Dependent Electron Liquid Correlation Energies for Local Spin-Density Calculations - a Critical Analysis. *Can. J. Phys.* **1980**, 58, 1200-1211.
- [14] Becke, A. D., Density-Functional Exchange-Energy Approximation with Correct Asymptotic-Behavior. *Phys. Rev. A* **1988**, 38, 3098-3100.
- [15] Perdew, J. P.; Burke, K.; Ernzerhof, M., Generalized Gradient Approximation Made Simple. *Phys. Rev. Lett.* **1996**, 77, 3865-3868.
- [16] Perdew, J. P.; Burke, K.; Ernzerhof, M., Comment on "Generalized Gradient Approximation Made Simple" - Reply. *Phys. Rev. Lett.* **1998**, 80, 891-891.
- [17] Hohenberg, P.; Kohn, W., Inhomogeneous Electron Gas. *Phys. Rev.* **1964**, 136, B864-B71.
- [18] Kohn, W.; Sham, L. J., Self-Consistent Equations Including Exchange and Correlation Effects. *Phys. Rev.* **1965**, 140, A1133-A38.
- [19] Slater, J. C., *The Self-Consistent Field for Molecular and Solids, Quantum Theory of Molecular and Solids*. McFraw-Hill: New York, 1974; Vol. 4.
- [20] Handy, N. C.; Cohen, A. J., Left-Right Correlation Energy. *Mol. Phys.* **2001**, 99, 403-412.
- [21] Handy, N. C.; Hoe, W. M.; Cohen, A. J., Assessment of a New Local Exchange Functional OPTX. *Chem. Phys. Lett.* **2001**, 341, 319-328.
- [22] Adamo, C.; Barone, V., Exchange Functionals with Improved Long-Range Behavior and Adiabatic Connection Methods without Adjustable Parameters: The mPW and mPW1PW Models. *J. Chem. Phys.* **1998**, 108, 664-675.
- [23] Gill, P. M. W., A New Gradient-Corrected Exchange Functional. *Mol. Phys.* **1996**, 89, 433-445.
- [24] Barone, V.; Adamo, C., Implementation and Validation of the Lacks-Gordon Exchange Functional in Conventional Density Functional and Adiabatic Connection Methods. *J. Comput. Chem.* **1998**, 19, 418-429.
- [25] Perdew, J. P., Density-Functional Approximation for the Correlation-Energy of the Inhomogeneous Electron-Gas. *Phys. Rev. B* **1986**, 33, 8822-8824.
- [26] Perdew, J. P.; Chevary, J. A.; Vosko, S. H.; Jackson, K. A.; Pederson, M. R.; Singh, D. J.; Fiolhais, C., Atoms, Molecules, Solids, and Surfaces - Applications

of the Generalized Gradient Approximation for Exchange and Correlation (Vol 46, Pg 6671, 1992). *Phys. Rev. B* **1993**, 48, 4978-4978.

- [27] Perdew, J. P., *Electronic Structure of Solids '91*. Akademie Verlag: Berlin, 1991.
- [28] Perdew, J. P.; Wang, Y., Accurate and Simple Analytic Representation of the Electron-Gas Correlation-Energy. *Phys. Rev. B* **1992**, 45, 13244-13249.
- [29] Lee, C. T.; Yang, W. T.; Parr, R. G., Development of the Colle-Salvetti Correlation-Energy Formula into a Functional of the Electron-Density. *Phys. Rev. B* **1988**, 37, 785-789.
- [30] Miehlich, B.; Savin, A.; Stoll, H.; Preuss, H., Results Obtained with the Correlation-Energy Density Functionals of Becke and Lee, Yang and Parr. *Chem. Phys. Lett.* **1989**, 157, 200-206.
- [31] Rogers, D., *Computational Chemistry using the PC*. 3rd ed.; Wiley-Interscience: Hoboken, N.J., 2003; p XX, 349 p.
- [32] Adamo, C.; Barone, V., Toward Reliable Density Functional Methods without Adjustable Parameters: The PBE0 Model. *J. Chem. Phys.* **1999**, 110, 6158-6170.
- [33] Truhlar, D. G.; Zhao, Y., The M06 Suite of Density Functionals for Main Group Thermochemistry, Thermochemical Kinetics, Noncovalent Interactions, Excited States, and Transition Elements: Two New Functionals and Systematic Testing of Four M06-Class Functionals and 12 other Functionals. *Theor. Chem. Acc.* **2008**, 120, 215-241.
- [34] Truhlar, D. G.; Zhao, Y., Comparative DFT Study of Van der Waals Complexes: Rare-Gas Dimers, Alkaline-Earth Dimers, Zinc Dimer, and Zinc-Rare-Gas Dimers. *J. Phys. Chem. A* **2006**, 110, 5121-5129.
- [35] Hamprecht, F. A.; Cohen, A. J.; Tozer, D. J.; Handy, N. C., Development and Assessment of New Exchange-Correlation Functionals. *J. Chem. Phys.* **1998**, 109, 6264-6271.
- [36] Boese, A. D.; Doltsinis, N. L.; Handy, N. C.; Sprik, M., New Generalized Gradient Approximation Functionals. *J. Chem. Phys.* **2000**, 112, 1670-1678.
- [37] Boese, A. D.; Handy, N. C., A New Parametrization of Exchange-Correlation Generalized Gradient Approximation Functionals. *J. Chem. Phys.* **2001**, 114, 5497-5503.
- [38] Yanai, T.; Tew, D. P.; Handy, N. C., A New Hybrid Exchange-Correlation Functional Using The Coulomb-attenuating Method (CAM-B3LYP). *Chem. Phys. Lett.* **2004**, 393, 51-57.

- [39] Tawada, Y.; Tsuneda, T.; Yanagisawa, S.; Yanai, T.; Hirao, K., A Long-Range-Corrected Time-Dependent Density Functional Theory. *J. Chem. Phys.* **2004**, 120, 8425-8433.
- [40] Vydrov, O. A.; Scuseria, G. E., Assessment of a Long-Range Corrected Hybrid Functional. *J. Chem. Phys.* **2006**, 125, 234109.
- [41] Vydrov, O. A.; Heyd, J.; Krukau, A. V.; Scuseria, G. E., Importance of Short-Range Versus Long-Range Hartree-Fock Exchange for the Performance of Hybrid Density Functionals. *J. Chem. Phys.* **2006**, 125, 074106.
- [42] Vydrov, O. A.; Scuseria, G. E.; Perdew, J. P., Tests of Functionals for Systems with Fractional Electron Number. *J. Chem. Phys.* **2007**, 126, 154109.
- [43] Head-Gordon, M.; Chai, J. D., Long-Range Corrected Hybrid Density Functionals with Damped Atom-Atom Dispersion Corrections. *Phys. Chem. Chem. Phys.* **2008**, 10, 6615-6620.
- [44] Head-Gordon, M.; Chai, J. D., Systematic Optimization of Long-Range Corrected Hybrid Density Functionals. *J. Chem. Phys.* **2008**, 128, 084106.
- [45] Casida, M. E., *Recent Advances in Density Functional Methods, Part I*. World Scientific: Singapore, 1995.
- [46] Furche, F.; Ahlrichs, R., Adiabatic Time-Dependent Density Functional Methods for Excited State Properties. *J. Chem. Phys.* **2002**, 117, 7433-7447.
- [47] Scalmani, G.; Frisch, M. J.; Mennucci, B.; Tomasi, J.; Cammi, R.; Barone, V., Geometries and Properties of Excited States in the Gas Phase and in Solution: Theory and Application of a Time-Dependent Density Functional Theory Polarizable Continuum Model. *J. Chem. Phys.* **2006**, 124.
- [48] Hollas, M., *Basic Atomic and Molecular Spectroscopy*. Royal Society of Chemistry: 2002; p 192.
- [49] Telle, H. H.; Urena, A. G., *Laser Chemistry - Spectroscopy, Dynamics and Applications*. John Wiley: 2007; p 502.
- [50] Bally, T.; Borden, W. T., Calculations on Open-Shell Molecules: A Beginner's Guide. In *Rev. Comp. Chem.*, Wiley-VCH, J. W. a. S., Inc., Ed. New York, 1999; Vol. 13.
- [51] Cohen, A. J.; Tozer, D. J.; Handy, N. C., Evaluation of $\langle S^2 \rangle$ in density functional theory. *J. Chem. Phys.* **2007**, 126, 214104.

- [52] Wang, J. H.; Becke, A. D.; Smith, V. H., Evaluation of [S-2] in Restricted, Unrestricted Hartree-Fock, and Density-Functional Based Theories. *J. Chem. Phys.* **1995**, 102, 3477-3480.
- [53] Arnbjerg, J.; Paterson, M. J.; Nielsen, C. B.; Jorgensen, M.; Christiansen, O.; Ogilby, P. R., One- and Two-Photon Photosensitized Singlet Oxygen Production: Characterization of Aromatic Ketones as Sensitizer Standards. *J. Phys. Chem. A* **2007**, 111, 5756-5767.
- [54] Paterson, M. J.; Christiansen, O.; Jensen, F.; Ogilby, P. R., Invited Review - Overview of Theoretical and Computational Methods Applied to the Oxygen-Organic Molecule Photosystem. *Photochem. Photobiol.* **2006**, 82, 1136-1160.
- [55] Robb, M. A.; Garavelli, M.; Olivucci, M.; Bernardi, F., A Computational Strategy for Organic Photochemistry. *Rev. Comp. Chem.* **2000**, 15, 87-146.
- [56] Ceulemans, A.; Lijnen, E., The Jahn-Teller Effect in Chemistry. *Bull. Chem. Soc. Jap.* **2007**, 80, 1229-1240.
- [57] Bernardi, F.; Olivucci, M.; Robb, M. A., Potential Energy Surface Crossings in Organic Photochemistry. *Chem. Soc. Rev.* **1996**, 25, 321-328.
- [58] Paterson, M. J.; Robb, M. A.; Blancafort, L.; DeBellis, A. D., Mechanism of an Exceptional Class of Photostabilizers: A Seam of Conical Intersection Parallel to Excited State Intramolecular Proton Transfer (ESIPT) in o-hydroxyphenyl-(1,3,5)-triazine. *J. Phys. Chem. A* **2005**, 109, 7527-7537.
- [59] Dylla, K. G.; Taylor, P. R.; Faegri, K.; Partridge, H., All-Electron Molecular Dirac-Hartree-Fock Calculations - The Group-IV Tetrahydrides CH₄, SiH₄, GeH₄, SnH₄, and PbH₄. *J. Chem. Phys.* **1991**, 95, 2583-2594.
- [60] Stevens, W. J.; Basch, H.; Krauss, M., Compact Effective Potentials and Efficient Shared-Exponent Basis-Sets for the 1st-Row and 2nd-Row Atoms. *J. Chem. Phys.* **1984**, 81, 6026-6033.
- [61] Hamann, D. R.; Schluter, M.; Chiang, C., Norm-Conserving Pseudopotentials. *Phys. Rev. Lett.* **1979**, 43, 1494-1497.
- [62] Vanderbilt, D., Soft Self-Consistent Pseudopotentials in a Generalized Eigenvalue Formalism. *Phys. Rev. B* **1990**, 41, 7892-7895.
- [63] Heß, B. A.; Marian, C. M.; Peyerimhoff, S. D., *Ab Initio* Calculations of Spin-Orbit Effects in Molecules Including Electron Correlation. In *Modern Electronic Structure Theory. Part 1.*, Yarkony, D. R., Ed. Word Scientific Publishing Co. Pte. Ltd.: Singapore, 1995; Vol. 2. Advanced Series in Physical Chemistry

- [64] Pearson, R. G., Concerning Jahn-Teller Effects. *Proc. Natl. Acad. Sci. USA* **1975**, 72, 2104-2106.
- [65] Garcia-Fernandez, P.; Bersuker, I. B.; Boggs, J. E., Orbital Disproportionation and Spin Crossover as a Pseudo Jahn-Teller Effect. *J. Chem. Phys.* **2006**, 125, 104102.
- [66] Bersuker, I. B., Modern Aspects of the Jahn-Teller Effect Theory and Applications to Molecular Problems. *Chem. Rev.* **2001**, 101, 1067-1114.
- [67] Paterson, M. J.; Bearpark, M. J.; Robb, M. A.; Blancafort, L., The Curvature of the Conical Intersection Seam: An Approximate Second-Order Analysis. *J. Chem. Phys.* **2004**, 121, 11562-11571.

CHAPTER 3

The Pseudo-Jahn-Teller Effect in Inorganic Photochemistry

As described in the previous chapter the pseudo-Jahn-Teller (pJT) effect is understood as a vibronic coupling between a pair of adiabatic electronic states (as obtained in the clamped nuclei Born-Oppenheimer approximation [1]). It is important to note that there is an unfortunate ambiguous terminology in the literature regarding the pseudo-Jahn-Teller effect. In the field of structural chemistry one often finds the term “second-order Jahn-Teller” used interchangeably with pseudo-Jahn-Teller [2-4]. In the field of non-adiabatic chemistry this term has the more well-defined meaning of the coupling of the components of a degenerate electronic state via vibrational motion computed at second-order, i.e., true Jahn-Teller coupling but at second order [1, 5]. The latter nomenclature will be followed below and the pseudo-Jahn-Teller coupling will be considered as the vibronic coupling between non-degenerate electronic states via non-degenerate, non-totally symmetric vibrational motion. The importance of the pJT effect in structural chemistry is that it can be thought of as a mixing of the ground state potential energy surface with that of a nearby excited state along a non-totally symmetric normal vibrational coordinate, thereby changing the curvature of the ground state surface and lowering the energy of critical points [6].

Pearson provided the first detailed study the pJT effect, and developed a perturbative expansion of the ground state adiabatic potential energy surface in terms of displacements along normal coordinates Q_i [7, 8]. The Pearson expansion is given below,

$$E(Q_i) = E_0 + Q_i \left\langle \Psi_0 \left| \frac{\partial V}{\partial Q_i} \right| \Psi_0 \right\rangle + \frac{Q_i^2}{2} \left\langle \Psi_0 \left| \frac{\partial^2 V}{\partial^2 Q_i} \right| \Psi_0 \right\rangle + Q_i^2 \sum_j \frac{\left[\left\langle \Psi_0 \left| \frac{\partial V}{\partial Q_i} \right| \Psi_j \right\rangle \right]^2}{E_0 - E_j} \dots (3.1)$$

where E is the electronic ground state energy, E_0 is the energy at the expansion point (the high symmetry structure), V is the nuclear-nuclear and nuclear-electronic terms of the potential energy in the Hamiltonian, E_j is the energy of the j -th excited electronic state, Ψ_0 is the ground state electronic wavefunction, while Ψ_j is that of excited electronic states. There is an expansion along each of the $3N-6$ normal vibrational coordinates $Q_{i \in 3N-6}$.

The 1st order term is always zero because the gradient of the optimized molecular structure is zero, i.e., in the terminology of Bersuker et al the structure is force equilibrated [9]. The relative magnitude of both quadratic terms determines if the pJT coupling lowers the symmetry of the optimized structure [10]. The first quadratic term is always positive for an optimized molecular geometry i.e., the electronic energy computed with a non-relaxed wavefunction at a distorted structure along Q_i will always be higher. The proof of this however is far from trivial and will not be discussed here (see Reference [9] and references therein). Bersuker and co-workers have proved this for Hartree-Fock and configuration interaction electronic wavefunctions [11]. The second quadratic term in the Pearson expansion is always negative since the excited state energies E_j are higher than the ground state energy (i.e., $E_0 < E_j$), which is known also as MacDonald's theorem and is related to the variational principle described in section 2.1 of chapter 2. MacDonald's theorem states that the excited state energy of a guess wavefunction is bounded from below by the energy of the true ground state energy [12]. This second quadratic term is the pJT coupling term and allows electronic states to mix via non-totally symmetric vibrations (this term accounts for relaxation of the wavefunction at distorted geometries). Thus, whether the ground state energy rises or is lowered along the direction Q_i depends upon the relative magnitude of both of these terms. Finally it should be noted that although equation 3.1 is very useful for illustrative purposes, more rigorous non-perturbative treatments of the pJT effect have been developed [9, 13], and in fact this body of work has shown that the pJT effect is the only source of configurational instability in molecules in non-degenerate electronic states.

Symmetry can predict which of these symmetry adapted normal vibrations (Q_i) give rise to zero change in the energy at second-order. For example, the matrix elements in equation 3.1 are non-zero only when the direct product of the irreducible representations (Γ) of each symmetry species contains the totally symmetric irreducible representation of the molecular point group (Γ_{TS}). In the final term,

$$\left\langle \Psi_0 \left| \frac{\partial V}{\partial Q_i} \right| \Psi_j \right\rangle \neq 0 \text{ iff } \Gamma_{\Psi_0} \otimes \Gamma_{Q_i} \otimes \Gamma_{\Psi_j} \supset \Gamma_{TS} \quad (3.2)$$

Thus, a non-totally symmetric distortion that lowers the energy in a closed shell electronic ground state (Γ_{TS}) must have the same symmetry as that of the excited electronic state involved in the vibronic coupling.

It has until recently been assumed that the energy difference denominator in the final quadratic term in equation 3.1 meant that only low-lying excited electronic states could give rise to pJT distortions, however recent work has shown that even states quite high in the electronic manifold can overcome the energetic penalty due to very large vibronic coupling matrix elements (Equation 3.2) [6, 9, 13, 14]. Previous work in assigning a pJT effect has relied upon showing that low-lying electronic states of the correct symmetry exist, and that the potential energy surface has negative curvature along vibrational coordinates of the appropriate symmetry [15].

Over the years the pJT effect has become very important in structural chemistry. It has been used to successfully explain many diverse chemical phenomena including molecular structure, molecular fluxionality, and electron delocalization in mixed valence compounds [9]. Inorganic chemistry is a rich source of such phenomena [2, 6, 9, 13], from relatively small molecules [16, 17], to many large transition metal complexes [18, 19], to the solid-state [20-22]. It gives information of why a particular system distorts and which states are involved in the vibronic mixing. For a good understanding of the nature of pJT problems they need to be treated with theoretical methods.

The theory of pJT effects was extensively examined by Bersuker. The author and his co-workers using the Pearson expansion described above, proved that the pseudo-Jahn-Teller effect is the only possible source of the instabilities of high symmetry molecular systems (inter alia planar BH_4^- , CH_4BH_3 , CH_3^- , NH_3 , octahedral metal complexes MH_6 ($M = Sc^{3+}$, V, Cr etc.) and series of octahedral hexafluoride systems) in non-degenerate states [6, 9, 11, 14]. As described in chapter 1, the pJT effect has also been successfully used by Paterson and co-workers in the explanation of Si-H-M bridging interactions in the transition metal hydrosilane complexes.

This chapter will focus on the modern computational treatment of the pseudo-Jahn-Teller effect using CASSCF force constants on two different systems: the first one, the

ammonia molecule with C_{3v} ground state symmetry rather than planar D_{3h} , and $\text{Mo}_2(\text{DXylF})_2(\text{O}_2\text{CCH}_3)_2(\mu_2\text{-O})_2$, an edge-sharing bioctahedral complex undergoing the pJT distortion of its main structural motif $\text{Mo}_2(\mu_2\text{-O})_2$ from D_{2h} to C_{2h} .

The CASSCF force constants method to treat the pJT effect was originally proposed by Bearpark and co-workers [10], and relies on analytical CASSCF Hessian calculations. The Hessian is the matrix containing the second derivatives of the electronic energy with respect to nuclear coordinates, and can be evaluated numerically or analytically. The difference between the numerical and analytical treatment of derivatives is that in the first case the energy derivatives are calculated using numerical differentiation i.e. the separate wavefunctions being optimized for different geometries and the gradients are calculated using a finite difference method:

$$\frac{dE}{dh} \approx \frac{E(h) - E(0)}{h} \quad (3.3)$$

where h is some nuclear perturbation (size of distortion in between two geometries). However, this approach is very sensitive to the step size of nuclear perturbation, if the step size is too small or too big this approach can give inaccurate results. For a large number of atoms, numerical derivative calculations are also very expensive due to the large number of energy calculations required, which makes them sometimes impractical. In the case of analytical gradients the energy derivatives are as follows:

$$\frac{dE}{dh} = \left\langle \frac{\partial \Psi}{\partial h} \left| \hat{H} \right| \Psi \right\rangle + \left\langle \Psi \left| \frac{\partial \hat{H}}{\partial h} \right| \Psi \right\rangle + \left\langle \Psi \left| \hat{H} \right| \frac{\partial \Psi}{\partial h} \right\rangle \quad (3.4)$$

The first and last term from equation 3.4 are generally the same for real wavefunctions so the equation can be rewritten as:

$$\frac{dE}{dh} = \left\langle \Psi \left| \frac{\partial \hat{H}}{\partial h} \right| \Psi \right\rangle + 2 \left\langle \Psi \left| \hat{H} \right| \frac{\partial \Psi}{\partial h} \right\rangle \quad (3.5)$$

The $\left\langle \Psi \left| \frac{\partial \hat{H}}{\partial h} \right| \Psi \right\rangle$ term is called the Hellmann-Feynman force and it is the response of the electronic Hamiltonian to a perturbation. According to the Hellman-Feynman theorem the other term i.e., the response of the wavefunction to a perturbation can be neglected if the wavefunction Ψ is the exact eigenfunction of \hat{H} operator. However, this can give a poor description of the forces acting on the nuclei if this is not the case [23]. In particular for atom-centred basis set expansions the second term (the so called Pulay forces) are very important. However, for first derivatives one can avoid expensive calculation of the response of the wavefunction parameters (i.e. molecular orbitals coefficients LCAO coefficients in HF, LCAO and configuration interaction CI coefficients in MCSCF as described in chapter 2). For second-order derivatives the response of the wavefunction to a perturbation needs to be evaluated (now additionally the response of the LCAO coefficients in MCSCF, needs to be evaluated). In CASSCF those terms contain the partial derivatives of the parameters that the wavefunction is dependent on i.e. LCAO, and CI parameters that can be expressed as [24, 25]:

$$\begin{aligned}
 E_{h\mu} &= E^{h\mu} + E^{C\mu} C_h + E^{X\mu} X_h + \dots \\
 (E^{X\mu})^{(ij)} &= \frac{\partial^2 E}{\partial X_{ij} \partial \mu} \\
 X_h^{(ij)} &= \frac{E_{ij}^{\mu X}}{\epsilon_i - \epsilon_j} \\
 (E^{X\mu} X_h)^{(ij)} &= \frac{(E_{ij}^{\mu X})^2}{\epsilon_i - \epsilon_j} \\
 C_h^{(0K)} &= \frac{E_{0K}^{\mu C}}{E_0 - E_K} \\
 (E^{C\mu} C_h)^{0K} &= \frac{(E_{0K}^{\mu C})^2}{E_0 - E_K}
 \end{aligned} \tag{3.6}$$

where h is a perturbation at first order and μ is a perturbation at second order, X and C are orbital rotation parameters and configuration interaction parameters respectively. Superscripts in the above set of equations represent the partial derivatives and the subscripts represent total derivatives evaluated at reference parameter values. These are called perturbed wavefunction parameters, and the equations themselves the coupled

perturbed CP-MCSCF equations. These equations need to be solved to determine the first-order response of the LCAO and CI coefficients, which can then be used to give the second-order derivatives. The second order derivatives with respect to orbital rotation and configuration interaction parameters correspond to the derivative coupling term from equation 3.1 [10].

If the CASSCF wavefunction is constructed by restricting the CSFs (described in Section 2.3 of the theory chapter) to functions of a particular symmetry class, then pJT coupling is automatically precluded if that symmetry class does not contain the coupled states in equation 3.1. The Hamiltonian matrix is block diagonal in a basis of symmetry adapted CSFs, so CSFs of a different symmetry do not contribute to the energy of a given state. Likewise for a non-degenerate state the gradient vector is totally symmetric, and geometry optimisation only requires CSFs with the same symmetry as the state of interest. However, at second-order CSFs of different symmetries can mix under a nuclear perturbation. In calculating CASSCF 2nd derivatives the CP-MCSCF equations are solved (Equations 3.6.), that as mentioned previously include both orbital mixing and configuration mixing (the so-called derivative coupling contributions, as described in chapter 2) [24]. The derivative coupling terms represent the real mixing of electronic states under a nuclear perturbation [10], and the presence of these terms in the CP-MCSCF equations can be controlled via symmetry constraints. If separate CASSCF calculations using different symmetry restrictions are performed (e.g., building the CASSCF wavefunction from the set of CSFs spanning all irreducible representations of the point group vs. building the CASSCF wavefunction from the set of CSFs spanning only the irreducible representation of the ground electronic state), then the pJT effect is manifest in a change of curvature for a particular non-totally symmetric normal coordinate (i.e., a change from real to imaginary vibrational frequency) when the vibronically coupled state is included in the calculation of the perturbed wavefunction.

Summing up, the desirable feature of the CASSCF symmetry-constrained Hessian method is that it conclusively demonstrates a vibronic coupling between electronic states, and therefore is capable of showing that a non-symmetric distortion is entirely electronic in origin. The coupling is thus proved to be responsible for the distorted lower symmetry structure, rather than assumed due to, for example, small energy differences between electronic states. Proving that an electronic induced distortion

exists in an isolated molecule is of importance for the solid-state also, showing that any observed distortion in the crystal structure is not (entirely) due to crystal packing as will be shown in section 3.2 of this chapter.

This method has been used successfully in several studies, and has been used to explain the structures of both closed- and open-shell organic molecules such as pentalene, cyclobutadiene, and cyclohexane [5, 10, 26]. It has also been used to explain the pseudo-rotation barrier in singlet $\text{Cr}(\text{CO})_5$ that arises from a pJT coupling (as opposed to true second-order Jahn-Teller coupling) between the component of the degenerate E' state and higher non-degenerate excited state [19]. This result presented an alternative viewpoint on the rationalisation of the pJT effect and shows the efficiency of this approach applied to transition metal photochemistry. It has also confirmed previous conclusions obtained in trying to fit a model vibronic coupling Hamiltonian for the $\text{Cr}(\text{CO})_5$ system, used to perform wavepacket dynamics simulations of the ultrafast electronic relaxation of this mechanism of this vibrationally hot photoproduct [27].

3.1. Ammonia.

3.1.1. Introduction.

Ammonia displays an interesting balance between competing internal forces and has interested the theoretical community for decades [28]. It can adopt two structures: planar with D_{3h} symmetry (NH_3^+ cation) or pyramidal with C_{3v} symmetry (NH_3 molecule). It was originally thought that the ammonia molecule is stable at the planar geometry. However this was before considering the effects of repulsive forces on the geometry of this system. Nuclear-nuclear repulsion influences the total energy of the molecule in such way that even though the energy coming from the electronic Hamiltonian of the system is lower for the planar structure of ammonia, the total energy of the pyramidal structure after inclusion of nuclear-nuclear repulsion energy contribution becomes lower thus making the pyramidal structure more stable (Figure 3.2 a)). The repulsion forces also influence the N-H bonds and cause their elongation. However, these forces do not explain exactly the mechanism of D_{3h} to C_{3v} distortion of an ammonia molecule. It is well known that the vibronic coupling between the ground

and first excited state needs to be considered as well. The excited state that couples to the ground state via a non-totally symmetric vibration and causes the pJT distortion from the planar structure is easily accessed due to those repulsion forces and is responsible for the ground state pyramidal shape of ammonia. Use of the pJT test to explain the mechanism of this distortion using the CASSCF method as described above will now be presented.

3.1.2. Computational details.

CCSD and CCSD(T) methods with cc-pVTZ and cc-pVQZ basis sets were used to characterize the critical points on the potential energy surface of ammonia along the distortion coordinate (Figure 3.2 a)). B3LYP and TD-B3LYP calculations were performed for comparison. CASSCF calculations on the planar structure of the system were performed with the cc-pVTZ basis set. The active space consisted of eight electrons in seven orbitals forming 490 singlet CSFs. All electrons of the system were included, excluding the nitrogen core $1s^2$ pair. CASSCF analysis of the planar structure is shown in figure 3.2 b. All calculations were performed using the Gaussian 03 [29] and Gaussian 09 [30] programs.

3.1.3. Results and discussion.

Figure number 3.1 presents a schematical representation of the energetics between the ground and first excited state PES along the symmetric bending vibration of a planar ammonia molecule. Table number 3.1 presents the calculated energies between different critical points on PES where E_A is the D_{3h} and C_{3v} inversion energy, E_B is the difference in energy of ground and first excited state of planar ammonia (D_{3h} symmetry – transition state on the ground state PES) and E_C is the difference in energy of the ground and first excited state of trigonal pyramid ammonia (C_{3v} symmetry – ground state minimum). Different methods have been compared including density functional methods (B3LYP for optimisations and TD-B3LYP for vertical and adiabatic excitations as described in the 2.2.4 subsection of chapter 2).

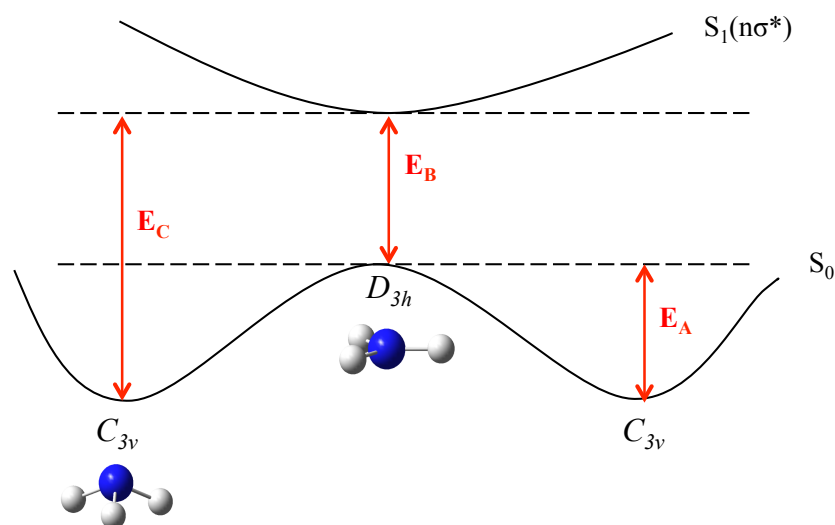


Figure 3.1. Schematic picture of the ground and first excited state PESs in the ammonia molecule.

The multiconfigurational CASSCF method, and coupled cluster methods (CCSD and CCSD(T)) were used for ground state energetics, and Equation-of-Motion CCSD (EOM-CCSD) for vertical excitation energies.

Method	Basis set	E_A /eV (kcal/mole)	E_B /eV adiabatic(vertical)	E_C /eV adiabatic(vertical)
TD-B3LYP	cc-pVTZ	0.2297 (5.30)	5.8495 (6.0551)	6.0792 (6.7168)
CCSD	cc-pVTZ	0.2685 (6.19)	- (6.5081)	6.5087 (7.3392)
CCSD(T)	cc-pVTZ	0.2775 (6.40)	-	-
CASSCF	cc-pVTZ	0.4746 (10.94)	6.0774 (6.3952)	6.6823 (7.4181)
TD-B3LYP	cc-pVQZ	0.2166 (4.99)	5.6948 (5.8518)	5.9114 (6.5136)
CCSD	cc-pVQZ	0.2443 (5.64)	- (6.3471)	6.3769 (7.1367)
CCSD(T)	cc-pVQZ	0.2506 (5.78)	-	-
Experiment	-	0.2503 (5.77) [31]	-	5.6356-7.2932 [32]

Table 3.1. Energetics of critical points on the PES of an ammonia molecule in eV and in kcal/mole (for E_A) where E_A is an inversion energy, E_B energy difference between the energy of D_{3h} structure and S_1 excited state and E_C is the excitation energy from the ground state C_{3v} to the S_1 excited state (as shown on the figure 3.1).

The PES using DFT is quite flat thus the B3LYP density functional used with cc-pVQZ basis set underestimates the inversion energy E_A , by around 1 kcal/mole comparing to experiment. The CASSCF method overestimates E_A by almost double compared to the experiment. However, this is not surprising because as mentioned previously this method does not include dynamic correlation of the electrons.

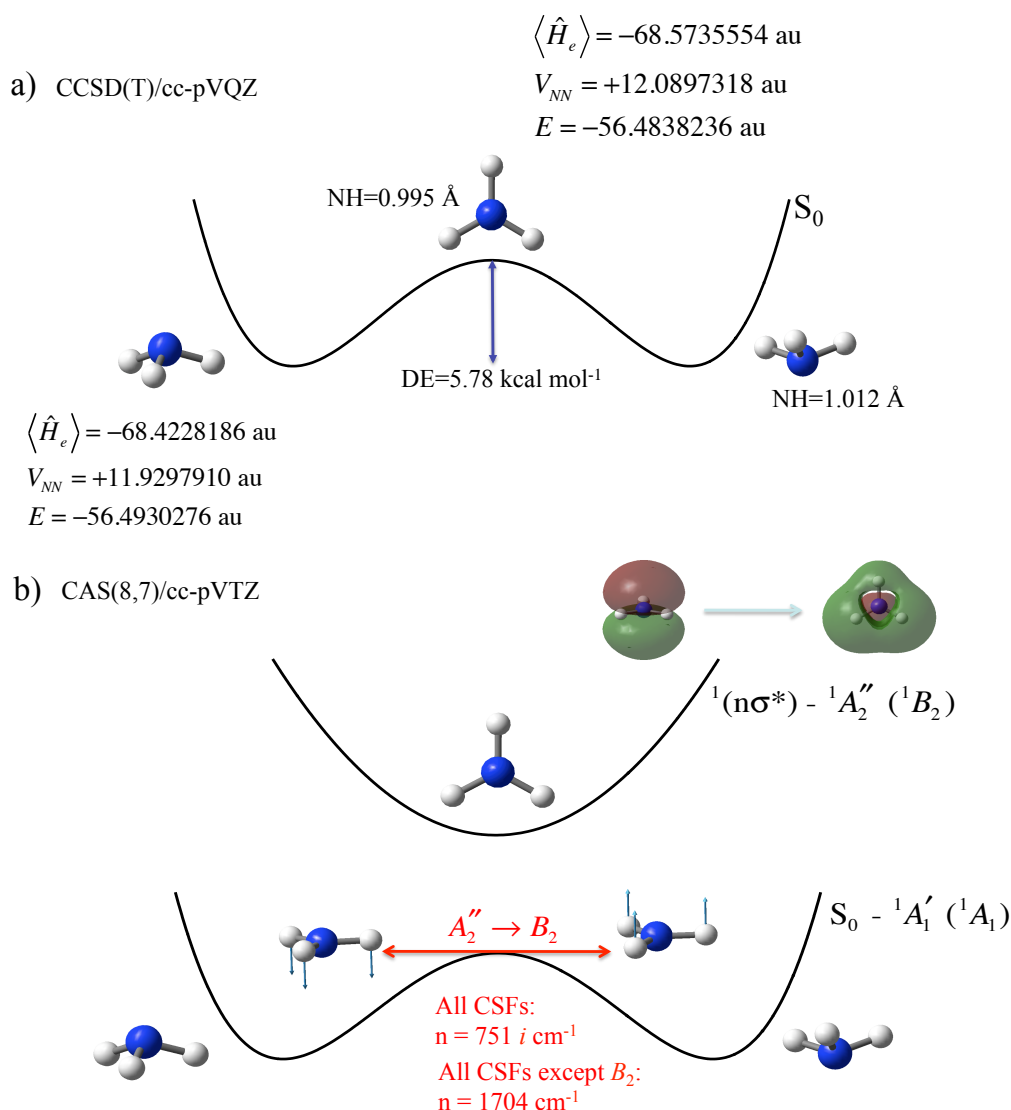


Figure 3.2. The pseudo-Jahn-Teller effect in ammonia (NH₃). (a) CCSD(T) ground state potential energy curve; breakdown of energy into expectation value of electronic Hamiltonian $\langle \hat{H}_e \rangle$, and nuclear-nuclear repulsion V_{NN} . (b) CASSCF frequency analysis of the pseudo-Jahn-Teller effect showing the effect of including CSFs of B₂ symmetry is to couple the ground and $1(n\sigma^*)$ states to give a negative curvature to the adiabatic ground state potential energy surface for inversion.

Using highly correlated CCSD and CCSD(T) methods (CCSD(T) with a cc-pVQZ basis set is essentially exact) it was found that the inversion barrier is approximately 5.8 kcal/mole which is in agreement with the experiment. E_C excitation energies were for most of the methods in the range of experimental values.

As mentioned previously the expectation value of the electronic wavefunction with the electronic Hamiltonian in ammonia is lower at planar geometries than at pyramidal ones (Figure 3.2 a)). However due to the larger nuclear repulsion at the optimal planar geometry, the pyramidal structure is favoured.

Moving to the CASSCF pJT frequency analysis test itself, the frequency calculation including all CSFs in the solution of the CP-MCSCF equations returns the value of the vibrational wavenumber of the mode that causes the inversion from D_{3h} geometry to C_{3v} . The value of this frequency is equal to $\nu=750.6i \text{ cm}^{-1}$ and suggests the D_{3h} geometry is a 1st order saddle point rather than a minimum. CP-MCSCF equations include both orbital and configurations mixing under the second-order nuclear perturbations and as mentioned before they correspond to the quadratic terms in equation 3.1. As described in the beginning of this chapter when the CASSCF frequency calculation is restricted to CSFs of only ground state symmetry (A_1 in the C_{2v} subgroup of D_{3h} in the case of ammonia molecule) the quadratic pJT coupling term contribution between states of different symmetries is switched off. Thus performing CASSCF frequency calculations including or excluding CSFs of different symmetries will indicate if a pJT mixing causes the given distortion via a vibrational coordinate. The pJT effect is demonstrated by a change from an imaginary frequency when all CSFs are included, to the real frequency when only CSFs of a particular symmetry type are excluded. Now a frequency calculation with CSFs of all symmetries except B_2 (in the C_{2v} subgroup of D_{3h} symmetry) gives no imaginary vibrational frequencies, and the vibrational wavenumber for inversion is now $\nu=1703.8 \text{ cm}^{-1}$. The lowest excited state of ammonia is a $^1(n\sigma^*)$ (HOMO to LUMO transition shown in figure 3.2 b)). This state has symmetry A_2'' in D_{3h} and symmetry B_2 in the C_{2v} subgroup. This state is located around 6.05 eV above the ground adiabatic state at the planar geometry for TD-B3LYP (Table 3.1). The CASSCF frequency results clearly show that this state pJT couples to the ground state to change the curvature of the lower adiabatic potential energy surface

and give a lower energy stable pyramidal C_{3v} minimum. Also note that since the S_1 state is nominally anti-bonding between the N and H's this pJT mixing also explains the NH bond elongation from the optimal D_{3h} to C_{3v} structures to allow for a reduction of nuclear–nuclear repulsion (Table 3.2.).

Method	Basis set	NH bond length/Å		NHN angle/deg.	
		C_{3v}	D_{3h}	C_{3v}	D_{3h}
TD-B3LYP	cc-pVTZ	1.014	0.996	106.47	120
CCSD	cc-pVTZ	1.012	0.994	105.95	120
CCSD(T)	cc-pVTZ	1.014	0.995	105.69	120
CASSCF	cc-pVTZ	1.023	1.000	104.40	120
TD-B3LYP	cc-pVQZ	1.013	0.996	106.85	120
CCSD	cc-pVQZ	1.010	0.993	106.47	120
CCSD(T)	cc-pVQZ	1.012	0.995	106.21	120
Experiment [31]	-	1.012		106.70	

Table 3.2. Experimental and calculated values of NH bond and HNH angle in the ammonia molecule.

3.2. The Pseudo-Jahn-Teller effect in $\text{Mo}_2(\text{DXylF})_2(\text{O}_2\text{CCH}_3)_2(\mu_2\text{-O})_2$.

3.2.1. Introduction.

In the following chapter the pJT effect influencing the structure of molybdenum complex $\text{Mo}_2(\text{DXylF})_2(\text{O}_2\text{CCH}_3)_2(\mu_2\text{-O})_2$ will be examined using the same pJT frequency test as described for the ammonia molecule.

The $\text{Mo}_2(\text{DXylF})_2(\text{O}_2\text{CCH}_3)_2(\mu_2\text{-O})_2$ complex belongs to the edge-sharing bioctahedral complexes (ESBO). The edge-sharing bioctahedral complexes exhibit a variety of molecular structures [33-35]. Their central motif with general formula $\text{M}_2(\mu_2\text{-X})_2$, where M is a metal and X is a bridging-ligand (Figure 3.3), displays a range of different M-M and M-X distances, and different XMX and MXM angles depending on the oxidation state of the metal atom and the type of bridging ligand [36-39].

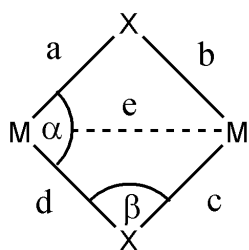


Figure 3.3. Geometrical parameters of the central $M_2(\mu_2-X)_2$ motif of an ESBO complex.

Metal-Metal bonding occurs by overlap of the d -orbitals on each metal centre. Figure 3.4 shows the σ , σ^* , π , π^* , δ and δ^* interactions between pairs of d -orbitals on each metal atom (M and M') in the $Mo_2(DXylF)_2(O_2CCH_3)_2(\mu_2-O)_2$ complex.

The energetic ordering is not straightforward with regards to the δ and δ^* orbitals. For example it has been reported that different ESBO complexes can sometimes have the anti-bonding orbital lower-lying than the bonding one [21, 34, 35]. Whether the order is $\delta < \delta^*$ or $\delta > \delta^*$ depends significantly on the identity of the bridging atoms and their interactions with the pure metal centred orbitals.

Computational studies, on the structure of the $Mo_2(DXylF)_2(O_2CCH_3)_2(\mu_2-O)_2$ ESBO complex, which was experimentally observed as having the shortest Mo-Mo double bond, and displays a rhomboidal (C_{2h}) structure rather than a square (D_{2h}) one at the central $Mo_2(\mu_2-O)_2$ motif, are presented next. Cotton et al have suggested that the distortion from the ideal D_{2h} structure is caused by the pseudo-Jahn-Teller (pJT) effect resulting in a mixing of the ground electronic state with a low-lying excited state giving rise to a lower energy structure of C_{2h} symmetry [20].

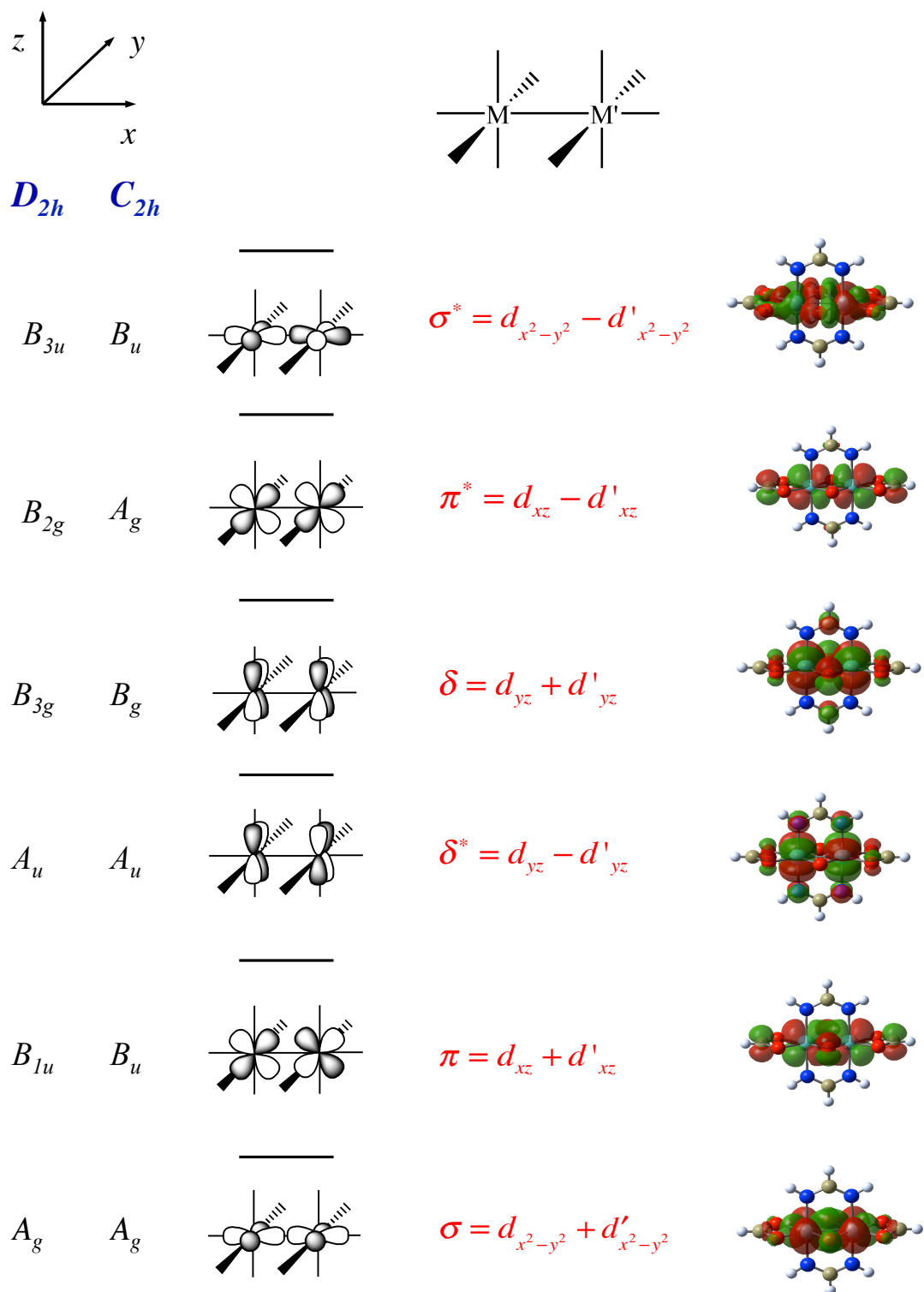


Figure 3.4. Primary orbitals involved in multiple metal-metal bonding in ESBO complexes. Schematic interactions between metal (M and M') centers shown at the left side, optimized CASSCF orbitals shown at the right side.

As discussed above the pJT effect has been of prime importance in the field of structural inorganic chemistry and this represents quite a challenge for multi-configurational wavefunction methods. The system studied here, a large transition bi-metal complex, is such a system. Thus the development of a model of the full target system was required and it is shown in figure 3.5 b) below. Although the primary objective in this paper is to explain the pJT effect in the model using CASSCF, additionally extensive density functional theory (DFT) calculations on both the target (Figure 3.5 a)), and model (Figure 3.5 b)) systems were undertaken.

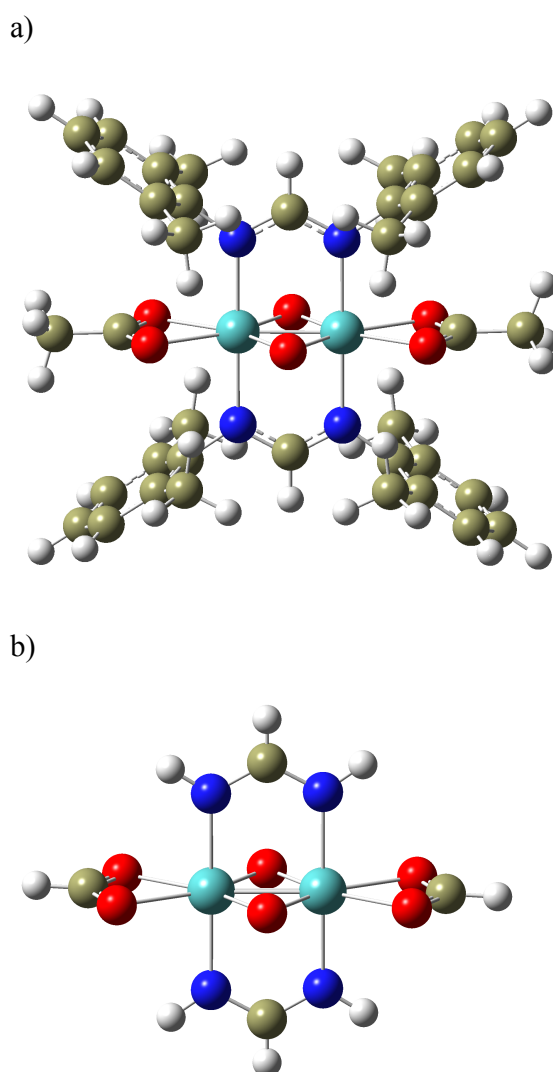


Figure 3.5. The structures of $\text{Mo}_2(\text{DXyIF})_2(\text{O}_2\text{CCH}_3)_2(\mu_2\text{-O})_2$ complex; a) optimized target system taken from the crystal structure in reference [20]; b) model complex used in multi-configuration calculations of pseudo-Jahn-Teller vibronic coupling.

3.2.2. Computational details.

DFT calculations were performed on the target system starting from the crystal structure in reference [20] and a model system (in which xylyl and methyl groups were substituted with hydrogens) using a range of standard functionals (B3LYP, PBE1PBE, B3PW91, BP86) in conjunction with the SDD effective core potential basis set on the molybdenum atoms, and the 6-311G** basis set for nitrogen, oxygen, carbon, and hydrogen atoms.

CASSCF calculations were performed using a hierarchy of active spaces: a basic active space consisted of 4 electrons distributed amongst the σ , π and δ bonding orbitals, and their correlating σ^* , π^* and δ^* anti-bonding orbitals (shown in figure 3.4). This active space was used for geometry optimization, and analytical frequency calculation. Single-point CASSCF calculations were also performed using augmented active spaces obtained by adding in-plane metal-oxygen bonding and anti-bonding orbitals: two different (6,8) active spaces and an (8,10) active space. For the CASSCF geometry optimization and frequency calculations the 3-21G* basis was used on the molybdenums, with the STO-3G basis on all other atoms, while for the single-point calculations the same basis as discussed above for DFT was used. It needs to be noted that the general features of the ground state CASSCF wavefunction were found to be insensitive to the one-electron basis set used. All computations were performed using the Gaussian 03 program [29].

3.2.3. Results and discussion.

The framework of $\text{Mo}_2(\text{DXylF})_2(\text{O}_2\text{CCH}_3)_2(\mu_2\text{-O})_2$ complex is very interesting due to the shortest metal-metal distances amongst all the Mo(IV) ESBO complexes [20]. To understand its structure a series of DFT optimizations on the target and model systems were performed. The initial geometry of the target system (with $\text{Mo}_2(\mu_2\text{-O})_2$ motif of C_{2h} symmetry) was taken as the crystal structure from reference [20]. However, results of structure optimisations using some of the chosen functionals significantly differed. For example optimisations on the C_{2h} crystal structure of the complex with the B3LYP functional determined the geometry to be a second order saddle point instead of a

minimum unlike the other functionals. This structure was then slightly distorted to follow the PES downhill and the minimum energy structure was found. Structure optimisations using other functionals on such a distorted structure were performed for completeness and the optimized geometrical parameters obtained for the central $\text{Mo}_2(\mu_2\text{-O})_2$ motif are given in table 3.3.

For the large target system the difference between non-equivalent bondlengths (a and b, c and d in figure 3.3) is quite small but nevertheless it is non-zero for all the functionals used and shows that the central motif adopts a C_{2h} geometry.

The distortion in the model system is more pronounced and closer to the experimental difference. However again there is a slight problem with the consistency of the DFT results. Optimisations on the D_{2h} geometry with the BP86 functional, show that the vibrational frequency of the rhomboidal distortion is 38.95 cm^{-1} , in total disagreement with the other three functionals, which predict this distortion frequency to be imaginary with various values. This may be due to the lack of Hartree-Fock exchange in the BP86 functional. The inconsistency in DFT methods shows that the DFT surface of the PES is very flat as was previously shown for the ammonia molecule.

Since the B3LYP functional predicts the values of the distortion parameter $\Delta_{ab} = \Delta_{cd}$ closer to the experimental values, in this work the main focus when comparing DFT with multiconfigurational CASSCF will be put on the results obtained with the B3LYP functional. The rhomboidal distortion vibrational frequency for B3LYP functional is 47.91 i cm^{-1} for geometries obtained under D_{2h} constraints, which becomes 23.34 cm^{-1} at the true C_{2h} minimum.

Moving to the CASSCF results on the model system the distortion parameter is now overestimated comparing with the experimental findings. This is due to the lack of dynamic correlation in CASSCF, however these results show the huge importance of static correlation, which unlike DFT methods, CASSCF does include. Thus CASSCF predicts the correct C_{2h} geometry of the ground state minimum that is in agreement with experiment.

Mo ₂ (μ ₂ -O) ₂ Motif Point Group	Optimized Geometrical Parameters						
	a, c / Å	b, d / Å	Δab = Δcd / Å	e / Å	α / deg.	β / deg.	ν _{Rd} / cm ⁻¹
DFT^a							
Target system							
B3LYP							
<i>C</i> _{2h}	1.961	1.964	0.003	2.329	107.2	72.8	55.06
PBE1PBE							
<i>C</i> _{2h}	1.949	1.950	0.001	2.305	107.5	72.5	60.05
B3PW91							
<i>C</i> _{2h}	1.954	1.955	0.001	2.315	107.4	72.6	57.71
BP86							
<i>C</i> _{2h}	1.977	1.978	0.001	2.344	107.3	72.7	-
Model system							
B3LYP							
<i>D</i> _{2h}	1.957	1.957	0.000	2.329	107.0	73.0	47.91 <i>i</i>
<i>C</i> _{2h}	1.974	1.941	0.033	2.330	107.0	73.0	23.34
PBE1PBE							
<i>D</i> _{2h}	1.943	1.943	0.000	2.306	107.2	72.8	33.93 <i>i</i>
<i>C</i> _{2h}	1.930	1.956	0.026	2.306	107.2	72.8	26.00
B3PW91							
<i>D</i> _{2h}	1.972	1.972	0.000	2.314	107.1	72.9	36.70 <i>i</i>
<i>C</i> _{2h}	1.935	1.962	0.027	2.315	107.1	72.9	24.49
BP86							
<i>D</i> _{2h}	1.972	1.972	0.000	2.344	107.1	72.9	38.95
<i>C</i> _{2h}	1.960	1.984	0.024	2.344	107.1	72.9	50.29
CAS(4,6) ^a							
<i>D</i> _{2h}	1.933	1.933	0.000	2.553	97.35	82.65	-
<i>C</i> _{2h}	1.860	2.004	0.144	2.765	88.70	91.30	-
CAS(4,6) ^b							
<i>D</i> _{2h}	1.910	1.910	0.000	2.527	97.17	82.83	452.91 <i>i</i>
<i>C</i> _{2h}	1.760	2.087	0.327	2.542	97.72	82.28	156.61
Experiment ^c							
<i>C</i> _{2h}	1.960	1.913	0.047	2.306	107.00	73.00	-

Table 3.3. Optimized geometrical parameters of the Mo₂(μ₂-O)₂ motif: bond-lengths (a-e), angles (α, β) and rhomboidal vibrational frequency (corresponding to *D*_{2h}-*C*_{2h} distortion). *i* = √-1 ; ^a SDD basis on Mo; 6-311G** basis on C, N, O and H; ^b 3-21G* basis on Mo; STO-3G basis on C, N, O and H; ^c Reference [20].

The ordering of the Kohn-Sham orbitals for the target system using the B3LYP functional reflects previous work in that the δ^* orbital is the lowest unoccupied molecular orbital (LUMO), and lies below the δ orbital (the LUMO + 1); the highest occupied molecular orbital (HOMO) is the π -bonding orbital. For the model system the Kohn-Sham orbital ordering has the π^* orbital as the LUMO, although it is almost degenerate with the δ^* orbital, which again lies below the δ orbital. The orbital ordering for the model system obtained with the CASSCF method is not as simple and will be described in more detail later in this chapter.

To determine the nature and energy of the lowest lying singlet electronic state, time-dependent density functional theory (TD-DFT) calculations together with CASSCF for excited states were also performed. The results of the TD-B3LYP calculations and CASSCF using different size of the active spaces are given in table 3.4.

METHOD	$\Delta E_T / \text{eV}$		$\Delta E_M / \text{eV}$	
	D_{2h}	C_{2h}	D_{2h}	C_{2h}
TD-B3LYP	-	1.251	1.266	1.280
CAS(4,6)	-	-	1.084	-
CAS(6,8)	-	-	1.544	-
CAS(8,10)	-	-	1.671	-

Table 3.4. Vertical excitation energies of the S_1 $^1(\pi\delta^*)$ state for the model (ΔE_M) and target systems (ΔE_T) using TD-DFT(B3LYP exchange correlation functional), and CASSCF. All calculations reported here used the SDD effective core potential on Mo, and the 6-311G** basis on N, O, C and H.

TD-B3LYP results for the target system the first singlet excited state (a^1B_{1g}) has a dominant particle-hole configuration involving an electron transferred from the HOMO to LUMO, i.e., from the π -bonding to the δ -anti-bonding orbital. Likewise for the model system the first excited state is $^1(\pi\delta^*)$, corresponding to HOMO \rightarrow LUMO + 1. The energy gaps for the model and target systems are quite close (1.280 vs 1.251) at the C_{2h} minima. The energy gap for the model at the constrained D_{2h} geometry is lower at 1.266 eV as is expected in a pJT situation (see for example figure 3.6.). The next state of B_{1g}

symmetry of the model is at 4.292 eV. It is important to note that the S_1 (a^1B_{1g}) state is not optically bright via a one-photon transition by virtue of symmetry selection rules.

The final point to note regarding DFT is that the pJT effect is one area where DFT has some inherent problems due to the single-configurational nature of the underlying Kohn-Sham state. As mentioned previously static correlation effects are poorly described in DFT and, as the CASSCF results below show, the model system studied here exhibits a fair degree of this. However, since the electronic state is closed-shell across the ground adiabatic potential energy surface DFT can probably be used with caution.

Turning now to the CASSCF calculations, the ground electronic state (S_0) is 1A_g and the first thing to note is the orbital occupations shown in table 3.5.

State	ORBITAL OCCUPATION									
	O sp_x	O sp_y	σ	π	δ^*	δ	π^*	σ^*	O sp_x^*	O sp_y^*
CAS(4,6)										
S_0	-	-	1.732	1.301	0.001	0.001	0.699	0.266	-	-
S_1	-	-	1.722	0.650	0.648	0.351	0.353	0.276	-	-
CAS(6,8)										
S_0	-	1.999	1.873	1.701	0.001	0.002	0.299	0.123	-	0.000
S_1	-	1.999	1.865	0.783	0.781	0.220	0.218	0.133	-	0.000
CAS(6,8)										
S_0	1.962	-	1.879	1.723	0.021	0.019	0.278	0.117	0.000	-
S_1	1.804	-	1.876	0.929	0.912	0.191	0.167	0.121	0.000	-
CAS(8,10)										
S_0	1.974	1.968	1.887	1.730	0.003	0.004	0.269	0.113	0.029	0.023
S_1	1.970	1.977	1.881	0.806	0.803	0.200	0.196	0.119	0.027	0.022

Table 3.5. Orbital occupations obtained as the diagonal elements of the CASSCF one-electron density matrix for the S_0 and S_1 states. In addition to the basic (4,6) active space shown in figure 2, augmented active spaces including bonding and anti-bonding oxygen centred orbitals were also investigated. All calculations reported here used SDD effective core potential on Mo, and the 6-311G** basis on N, O, C and H.

These are the diagonal elements of the one-electron density matrix and give an indication about the multi-configurational nature of the wavefunction. For all of the active spaces detailed in table 3.4 it is clear that the electronic structure is slightly more complicated than just $\sigma^2\pi^2$ as would be imposed in a single-configuration calculation. Significant correlation between electrons in the σ -bonding and σ -anti-bonding orbitals, and electrons in the π -bonding and π -anti-bonding orbitals, indicated by the significant

population of the anti-bonding orbitals, is observed. The larger active spaces obtained by adding in-plane M-O orbitals (denoted by the largest O centered component in table 3.5) do not qualitatively change the nature of the wavefunction. It should also be noted that the CASSCF density of S_0 in the various active spaces changes very little with the quality of basis set, giving confidence that the smaller basis used in the analytical frequency calculations generates accurate CASSCF wavefunctions.

The first excited state S_1 clearly involves the transfer of electron density from the π -system to the δ -system. S_1 can therefore be identified as the $^1(\pi\delta^*)$ state, and again there is significant correlation between electrons in the δ and δ^* orbitals. The CASSCF state based results confirm the idea of δ and δ^* ordering as in the S_1 state the occupation of the δ^* orbital is significantly greater than that of the δ orbital, i.e., the electronic structure of the S_1 state can be approximated as $\sigma^2\pi^1\delta^{*1}$, although again there is significant correlation in the σ , π , and δ systems.

We now turn to the CASSCF frequency analysis of the pJT effect causing the D_{2h} - C_{2h} distortion of the central pattern in this complex. The CAS(4,6) optimized geometrical parameters for both the D_{2h} and C_{2h} structures are given in table 3.3. Analytical frequency calculations using a CASSCF wavefunction expanded in a basis of all the CSFs (total = 105) confirms that the D_{2h} structure is a transition state. The transition vector is the rhomboidal distortion coordinate (Q_{rd}), and has b_{1g} symmetry, with a vibrational frequency of $452.91 i \text{ cm}^{-1}$. This transition vector is shown schematically in figure 3.6 for the central $\text{Mo}_2(\mu_2\text{-O})_2$ motif. When the frequency calculation is restricted to include CSFs of only the ground state symmetry A_g (total = 21), this vibrational frequency is no longer imaginary (37.70 cm^{-1}).

It can be concluded here that there is a vibronic coupling between the ground electronic state ($S_0 = ^1A_g$) and the first excited state ($S_1 = ^1B_{1g} = ^1(\pi\delta^*)$). The symmetries of the various entities are given in equation 3.7.

$$\begin{aligned} \Psi_0 &\rightarrow {}^1A_g \\ Q_{Rd} &\rightarrow b_{1g} \\ \Psi_i = {}^1(\pi\delta^*) &\rightarrow {}^1B_{1g} \\ \Gamma_{\Psi_0} \otimes \Gamma_{Q_{Rd}} \otimes \Gamma_{\Psi_i} &\supset A_g \end{aligned}$$

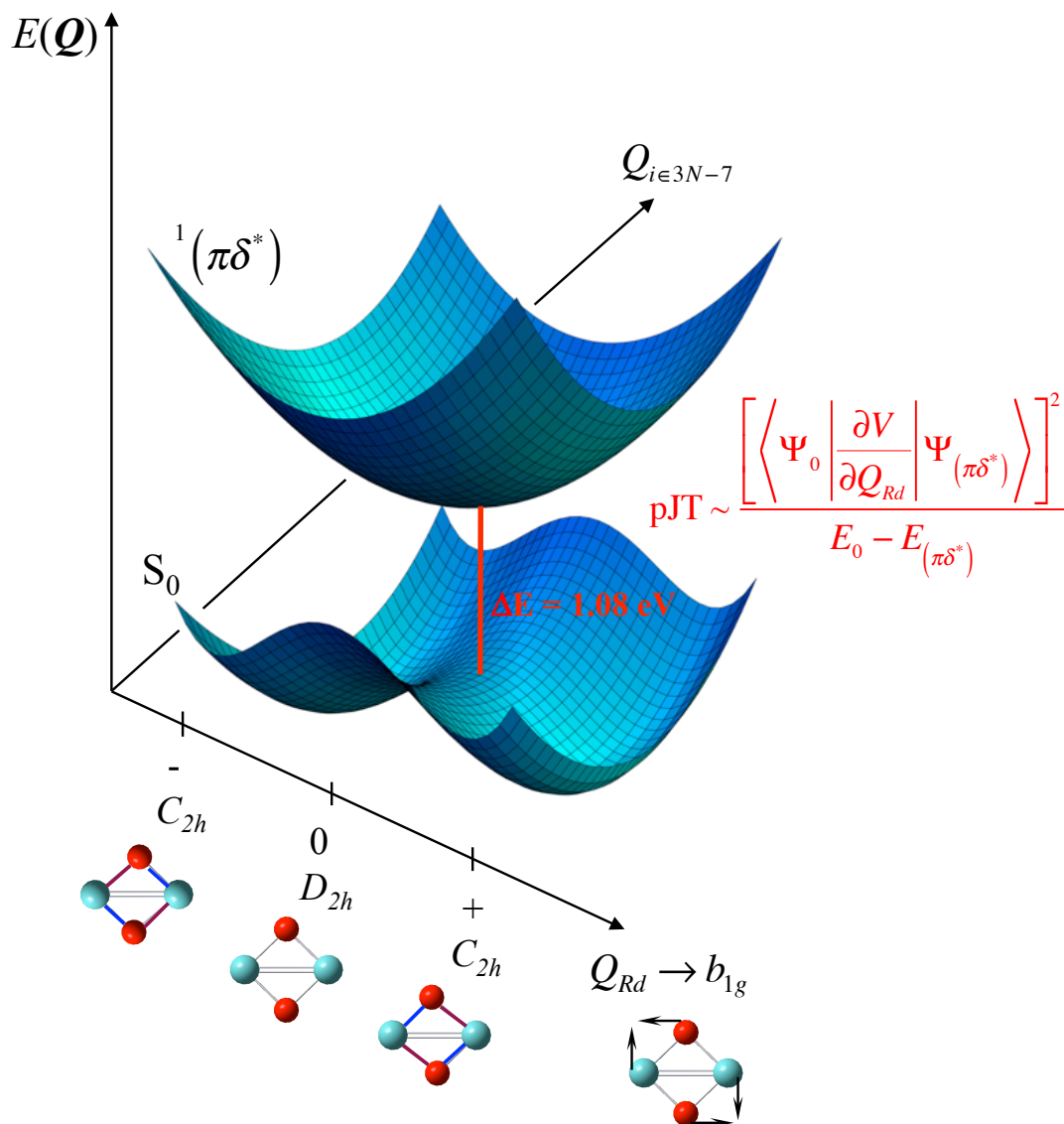


Figure 3.6. Schematic potential energy surfaces of the ground electronic state (S_0), and first excited singlet state ($S_1 - {}^1(\pi\delta^*)$) of the $\text{Mo}_2(\text{DXylF})_2(\text{O}_2\text{CCH}_3)_2(\mu_2\text{-O})_2$ complex. The rhomboidal distortion normal coordinate (Q_{Rd}) of b_{1g} symmetry is shown. Pseudo-Jahn-Teller coupling between the two electronic states gives the lower potential energy surface negative curvature along this coordinate, leading to equivalent minima of C_{2h} symmetry (equivalent Mo-O bonds are coloured blue and purple) in the positive and negative distortions along Q_{Rd} .

The CASSCF energy gap between the two electronic states is 0.947 eV (Table 3.4). Thus, the fact that the curvature along the rhomboidal distortion mode changes when CSFs of B_{1g} symmetry are included in the frequency calculation indicates a pJT coupling operates (Equation 3.2. is fulfilled). CASSCF calculations also confirm that the S_1 $^1(\pi\delta^*)$ state has its minimum energy geometry at a D_{2h} structure (Figure 3.3).

To conclude, the pseudo-Jahn-Teller effect in the edge-sharing bioctahedral complex $\text{Mo}_2(\text{DXylF})_2(\text{O}_2\text{CCH}_3)_2(\mu_2\text{-O})_2$ using a variety of computational techniques was studied. The results show that in both the large target and a smaller model system the central $\text{Mo}_2(\mu_2\text{-O})_2$ motif has a rhomboidal shape and C_{2h} symmetry. CASSCF Hessian calculations reveal that the distortion from D_{2h} to C_{2h} symmetry is caused by a vibronic coupling between the ground electronic state and the first excited singlet state, which can be characterized as a $^1(\pi\delta^*)$ state thus the pJT effect operates in this system changing the shape of main $\text{Mo}_2(\mu_2\text{-O})_2$ motif.

3.3. List of references.

- [1] Worth, G. A.; Cederbaum, L. S., Beyond Born-Oppenheimer: Molecular Dynamics Through a Conical Intersection. *Ann. Rev. Phys. Chem.* **2004**, 55, 127-158.
- [2] Burdett, J. K., Use of the Jahn-Teller Theorem in Inorganic-Chemistry. *Inorg. Chem.* **1981**, 20, 1959-1962.
- [3] Toyota, A.; Koseki, S., Energy Component Analysis of the Pseudo-Jahn-Teller Effect in the Bicyclic Nonalternant Hydrocarbons: The Pentalenoid and Heptalenoid Systems. *J. Phys. Chem.* **1996**, 100, 2100-2106.
- [4] Cotton, F. A.; Donahue, J. P.; Hall, M. B.; Murillo, C. A.; Villagran, D., Reaction Products of $W(CO)_6$ with Formamidines; Electronic Structure of a $W_2(\mu-CO)_2$ Core with Unsymmetric Bridging Carbonyls. *Inorg. Chem.* **2004**, 43, 6954-6964.
- [5] Paterson, M. J.; Bearpark, M. J.; Robb, M. A.; Blancafort, L.; Worth, G. A., Conical Intersections: A Perspective on the Computation of Spectroscopic Jahn-Teller Parameters and the Degenerate 'Intersection Space'. *Phys. Chem. Chem. Phys.* **2005**, 7, 2100-2115.
- [6] Bersuker, I. B., Modern Aspects of the Jahn-Teller Effect Theory and Applications to Molecular Problems. *Chem. Rev.* **2001**, 101, 1067-1114.
- [7] Pearson, R. G., A Symmetry Rule for Predicting Molecular Structure and Reactivity. *J. Am. Chem. Soc.* **1969**, 91, 1252-1254.
- [8] Pearson, R. G., Concerning Jahn-Teller Effects. *Proc. Natl. Acad. Sci. USA* **1975**, 72, 2104-2106.
- [9] Bersuker, I. B., *The Jahn-Teller Effect*. Cambridge: 2006; p 616.
- [10] Bearpark, M. J.; Blancafort, L.; Robb, M. A., The Pseudo-Jahn-Teller Effect: A CASSCF Diagnostic. *Mol. Phys.* **2002**, 100, 1735-1739.
- [11] Bersuker, I. B.; Balabanov, N. B.; Pekker, D.; Boggs, J. E., Pseudo Jahn-Teller Origin of Instability of Molecular High-Symmetry Configurations: Novel Numerical Method and Results. *J. Chem. Phys.* **2002**, 117, 10478-10486.
- [12] Cramer, C. J., *Essentials of Computational Chemistry*. John Wiley and Sons: 2004; p 596.
- [13] Bersuker, I. B., The Jahn-Teller Effect as a General Tool for Solving Molecular and Solid State Problems: Novel Findings. *J. Mol. Struct.* **2007**, 838, 44-52.

- [14] Garcia-Fernandez, P.; Bersuker, I. B.; Boggs, J. E., Orbital Disproportionation and Spin Crossover as a Pseudo Jahn-Teller Effect. *J. Chem. Phys.* **2006**, *125*, 104102.
- [15] Paterson, M. J.; Chatterton, N. P.; McGrady, G. S., View from the Bridge: A Pseudo-Jahn-Teller Approach to Transition Metal Hydrosilane Complexes. *New J. Chem.* **2004**, *28*, 1434-1436.
- [16] Garcia-Fernandez, P.; Bersuker, I. B.; Boggs, J. E., Why Are Some ML_2 Molecules ($M = Ca, Sr, Ba; L = H, F, Cl, Br$) Bent while Others are Linear? Implications of the Pseudo Jahn-Teller Effect. *J. Phys. Chem.* **2007**, *111*, 10409-10415.
- [17] Viel, A.; Einfeld, W.; Neumann, S.; Domcke, W.; Manthe, U., Photoionization-Induced Dynamics of Ammonia: *Ab initio* Potential Energy Surfaces and Time-Dependent Wave Packet Calculations for the Ammonia Cation. *J. Chem. Phys.* **2006**, *124*, 214306.
- [18] Borshch, S. A.; Ogurtsov, I. Y.; Bersuker, I. B., Pseudo-Jahn-Teller Effect as a Source of Tetragonal Distortions in Hexafluoride Complexes. *J. Struct. Chem.* **1982**, *23*, 825-829.
- [19] McKinlay, R. G.; Paterson, M. J., The Jahn-Teller Effect in Binary Transition Metal Carbonyl Complexes. In *The Jahn-Teller Effect: Advances and Perspectives; Springer Series in Chemical Physics*, Köppel, H.; Barentzen, H.; Yarkony, D. R., Eds. Springer: Heidelberg, 2010.
- [20] Cotton, F. A.; Daniels, L. M.; Murillo, C. A.; Slaton, J. G., A Pseudo-Jahn-Teller distortion in an $Mo_2(\mu_2-O)_2$ Ring Having the Shortest Mo-IV-Mo-IV Double Bond. *J. Am. Chem. Soc.* **2002**, *124*, 2878-2879.
- [21] Anderson, L. B.; Cotton, F. A.; DeMarco, D.; Fang, A.; Ilsley, W. H.; Kolthammer, B. W. S.; Walton, R. A., Experimental and Theoretical Evidence for Double Bonds Between Metal Atoms. Dinuclear Alkoxo-Bridged Ditungsten (IV,IV) Complexes $W_2Cl_4(OR)_4(ROH)_2$. *J. Am. Chem. Soc.* **1981**, *103*, 5078-5086.
- [22] Koppitz, J.; Schirmer, O. F.; Seal, M., Pseudo-Jahn-Teller Optical-Absorption of Isolated Nitrogen in Diamond. *J. Phys. C: Solid State Phys.* **1986**, *19*, 1123-1133.

- [23] Almlof, J.; Taylor, P. R., Molecular-Properties from Perturbation-Theory - A Unified Treatment of Energy Derivatives. *Int. J. Quantum Chem.* **1985**, *27*, 743-768.
- [24] Yamamoto, N.; Vreven, T.; Robb, M. A.; Frisch, M. J.; Schlegel, H. B., A Direct Derivative MC-SCF Procedure. *Chem. Phys. Lett.* **1996**, *250*, 373-378.
- [25] Vreven, T. PhD Thesis: The Theoretical Investigation of Photochemical Reactions: *Ab Initio* Trajectories With Surface Hopping. University of London (King's College), London, 1998.
- [26] Blancafort, L.; Bearpark, M. J.; Robb, M. A., Ring Puckering of Cyclooctatetraene and Cyclohexane is Induced by Pseudo-Jahn-Teller Coupling. *Mol. Phys.* **2006**, *104*, 2007-2010.
- [27] Worth, G. A.; Welch, G.; Paterson, M. J., Wavepacket Dynamics Study of Cr(CO)₅ after Formation by Photodissociation: Relaxation through an (E ⊕ A) ⊕ e Jahn-Teller Conical Intersection. *Mol. Phys.* **2006**, *104*, 1095-1105.
- [28] Kettle, S. F. A., *Symmetry and Structure: Readable Group Theory for Chemists*. 3 ed.; Wiley: Chichester, 2007.
- [29] Frisch, M. J. T., G. W.; Schlegel, H. B.; Scuseria, G. E.; Robb, M. A.; Cheeseman, J. R.; Montgomery, Jr., J. A.; Vreven, T.; Kudin, K. N.; Burant, J. C.; Millam, J. M.; Iyengar, S. S.; Tomasi, J.; Barone, V.; Mennucci, B.; Cossi, M.; Scalmani, G.; Rega, N.; Petersson, G. A.; Nakatsuji, H.; Hada, M.; Ehara, M.; Toyota, K.; Fukuda, R.; Hasegawa, J.; Ishida, M.; Nakajima, T.; Honda, Y.; Kitao, O.; Nakai, H.; Klene, M.; Li, X.; Knox, J. E.; Hratchian, H. P.; Cross, J. B.; Bakken, V.; Adamo, C.; Jaramillo, J.; Gomperts, R.; Stratmann, R. E.; Yazyev, O.; Austin, A. J.; Cammi, R.; Pomelli, C.; Ochterski, J. W.; Ayala, P. Y.; Morokuma, K.; Voth, G. A.; Salvador, P.; Dannenberg, J. J.; Zakrzewski, V. G.; Dapprich, S.; Daniels, A. D.; Strain, M. C.; Farkas, O.; Malick, D. K.; Rabuck, A. D.; Raghavachari, K.; Foresman, J. B.; Ortiz, J. V.; Cui, Q.; Baboul, A. G.; Clifford, S.; Cioslowski, J.; Stefanov, B. B.; Liu, G.; Liashenko, A.; Piskorz, P.; Komaromi, I.; Martin, R. L.; Fox, D. J.; Keith, T.; Al-Laham, M. A.; Peng, C. Y.; Nanayakkara, A.; Challacombe, M.; Gill, P. M. W.; Johnson, B.; Chen, W.; Wong, M. W.; Gonzalez, C.; and Pople, J. A. *Gaussian 03, Revision C.02*, Gaussian, Inc.: Wallingford CT, 2004.
- [30] Frisch, M. J. T., G. W.; Schlegel, H. B.; Scuseria, G. E.; Robb, M. A.; Cheeseman, J. R.; Scalmani, G.; Barone, V.; Mennucci, B.; Petersson, G. A.;

Nakatsuji, H.; Caricato, M.; Li, X.; Hratchian, H. P.; Izmaylov, A. F.; Bloino, J.; Zheng, G.; Sonnenberg, J. L.; Hada, M.; Ehara, M.; Toyota, K.; Fukuda, R.; Hasegawa, J.; Ishida, M.; Nakajima, T.; Honda, Y.; Kitao, O.; Nakai, H.; Vreven, T.; Montgomery, Jr., J. A.; Peralta, J. E.; Ogliaro, F.; Bearpark, M.; Heyd, J. J.; Brothers, E.; Kudin, K. N.; Staroverov, V. N.; Kobayashi, R.; Normand, J.; Raghavachari, K.; Rendell, A.; Burant, J. C.; Iyengar, S. S.; Tomasi, J.; Cossi, M.; Rega, N.; Millam, N. J.; Klene, M.; Knox, J. E.; Cross, J. B.; Bakken, V.; Adamo, C.; Jaramillo, J.; Gomperts, R.; Stratmann, R. E.; Yazyev, O.; Austin, A. J.; Cammi, R.; Pomelli, C.; Ochterski, J. W.; Martin, R. L.; Morokuma, K.; Zakrzewski, V. G.; Voth, G. A.; Salvador, P.; Dannenberg, J. J.; Dapprich, S.; Daniels, A. D.; Farkas, Ö.; Foresman, J. B.; Ortiz, J. V.; Cioslowski, J.; Fox, D. J., Gaussian 09, Revision A.02. **2009**.

- [31] Rauk, A.; Allen, L. C.; Clementi, E., Electronic Structure and Inversion Barrier of Ammonia. *J. Chem. Phys.* **1970**, *52*, 4133-4144.
- [32] Okabe, H., *Photochemistry of Small Molecules*. Wiley: New York, 1978; p 431.
- [33] Cotton, F. A.; Walton, R. A., *Multiple Bonds Between Metal Atoms*. Second ed.; Clarendon Press; Oxford University Press: Oxford; New York, 1993; p 787.
- [34] Cotton, F. A.; Wilkinson, G.; Murillo, C. A.; Bochmann, M., *Advanced Inorganic Chemistry*. Sixth ed.; Wiley-Interscience: 1999.
- [35] Shaik, S.; Hoffmann, R.; Fisel, C. R.; Summerville, R. H., Bridged and Unbridged M_2L_{10} Complexes. *J. Am. Chem. Soc.* **1980**, *102*, 4555-4572.
- [36] Cotton, F. A., The structures of Metal-Metal-Bonded Edge-Sharing Bioctahedral Complexes. *Polyhedron* **1987**, *6*, 667-677.
- [37] Palacios, A. A.; Aullon, G.; Alemany, P.; Alvarez, S., Through-Ring Bonding in Edge Sharing Dimers of Octahedral Complexes. *Inorg. Chem.* **2000**, *39*, 3166-3175.
- [38] McGrady, J. E.; Stranger, R.; Lovell, T., Electronic Structure of Face- and Edge-Shared Bioctahedral Systems: A Comparison of $M_2Cl_9^{3-}$ and $M_2Cl_{10}^{4-}$, $M = Cr, Mo, W$. *Inorg. Chem.* **1998**, *37*, 3802-3808.
- [39] Canich, J. A. M.; Cotton, F. A.; Daniels, L. M.; Lewis, D. B., Further Study of Metal Metal Bond Lengths in Homologous Edge-Sharing Bioctahedral Complexes. *Inorg. Chem.* **1987**, *26*, 4046-4050.

CHAPTER 4

Meridial to facial photoisomerisation of the closed-shell Platinum-bis(8-quinolinyl)amido complex

This chapter presents computational investigations of a recent intriguing experimental result from Harkins and Peters [1]. These authors found that light irradiation of the (bis(8-quinoliny)amido)PtMe₂I (bis(8-quinoliny)amido=BQA) complex results in an unexpected stereochemical transformation from the meridional (*mer*) form to the facial (*fac*) form (Figure 4.1)

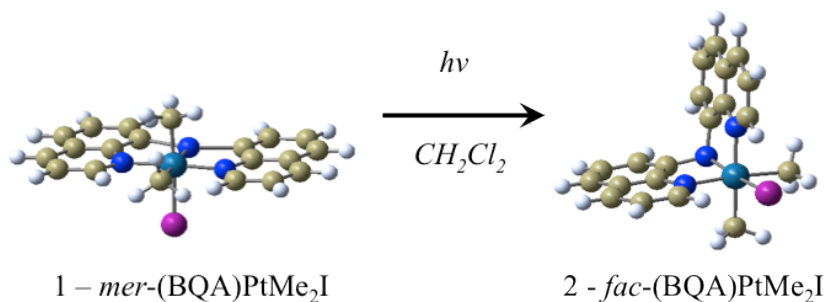


Figure 4.1. *Meridial* to the *facial* isomerisation of (BQA)PTME₂I complex

Density functional methods (DFT, TD-DFT) together with electron correlation methods (CIS, CASSCF) were used to find the possible route for photochemical pathway of this isomerisation.

4.1. Introduction.

The BQA ligand belongs to the group of robust “pincer-type” amide ligands (Figure 4.2) that display a rich variety of chemistry [2-4] and can be characterised as having one of the highest thermal stabilities amongst other pincer ligands.

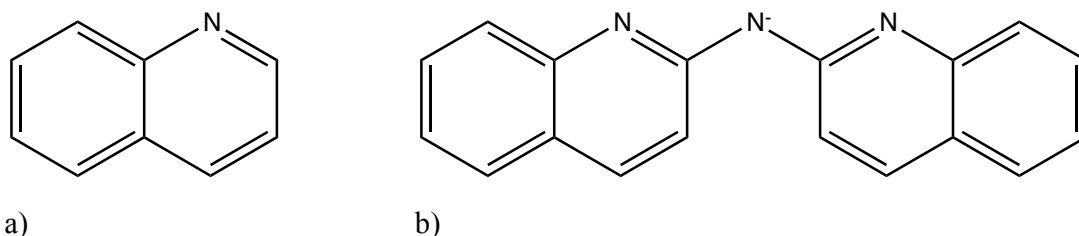


Figure 4.2. The structure of a) single quinoline ligand b) bis-quinoliny amide ligand.

Pincer type ligands were first synthesized in the end of 1970s, however this area was very long unexplored and only over the past few years, investigations on the chemistry

of these ligands started to increase radically, especially in the field of transition metal chemistry. Transition metal complexes with these ligands are very popular in organometallic and inorganic chemistry due to their potential applications in catalysis [5-7], electrochemical devices [8], or in the activation of small molecules [4, 9]. They can adopt a variety of geometries, from square planar structures to more distorted ones [6, 8, 10-13]. The common bonding feature of such complexes is that the metal is bonded to the quinolinyl arms via the nitrogen donor atoms, and that the amide nitrogen is sp^2 hybridized, thus leading to significant conjugation through the π -system. Quinoline and related ligands showing ligand-localised photochemistry have been studied recently [14, 15], with important consequences for use as organic light emitting diodes (OLEDs) due to their great fluorescence emission properties. One of such systems is tris(8-hydroxyquinoline) aluminum (Alq_3) which when incorporated into a multilayer structure improves significantly the fluorescent emission, stability, sensitivity and the brightness of the OLED [16].

4.2. Computational Details

The ground state isomeric forms of (BQA)PTME₂I were studied using density functional theory (DFT). For the DFT calculations the one-electron basis set used was as follows: the Stuttgart Dresden effective core potential (SDD) on the platinum (60 core electrons), and iodine (46 core electrons), in conjunction with the standard SDD valence basis; and the 6-31G(d,p) basis on carbon, nitrogen, and hydrogen. Electronic spectroscopy was studied using time-dependent DFT. The lowest 60 electronic eigenstates were used to construct the spectrum by convoluting each transition with a Gaussian function (FWHM = 15 nm) to account for homogenous line broadening. Using analytical TD-DFT gradients [17, 18], a geometry optimisation in the excited manifold was performed. These were used to study the relaxed excited state geometries. Ground and excited state solvent effects were investigated using the B3LYP functional in conjunction with the polarizable continuum model (PCM) [19, 20] with all the defaults settings as implemented in Gaussian 09 [20]. It should be noted that optimised geometries in both the ground and excited states were found to be insensitive to the functional used. In order to investigate non-adiabatic relaxation pathways complete active space self-consistent field (CASSCF) theory was used. Obviously such a large

system presents some difficulties in choosing an appropriate active space. Qualitatively, TD-DFT orbitals involved in the photochemistry on both the reactant and product sides of the photoreaction were looked at, which involved ligand-centered π -orbitals. Initial guess orbitals were natural orbitals from an unrestricted Hartree-Fock calculation. As described in the chapter 2, these are the orbitals which diagonalise the one-electron density matrix and whose eigenvalues are occupation numbers that give a measure of the importance of that orbital in a multi-configurational wavefunction. These orbitals were used to generate active spaces consisting of 14 electrons distributed in 12 orbitals, generating 314028 singlet configurations. These CASSCF wavefunctions were checked for stability by switching some of the initial valence orbitals for alternative core or virtual orbitals and observing convergence to the same state. For the CASSCF calculations the one electron basis on platinum and iodine was as above, while for carbon, nitrogen, and hydrogen the 3-21G(d,p) basis was used. For the conical intersection optimisation with CASSCF, the orbital derivative terms were neglected in the solution of the coupled perturbed multi-configuration self-consistent field (CP-MCSCF) equations. All DFT computations were performed with the Gaussian 09 program [20], while the CASSCF calculations were performed with the Gaussian 03 program [21].

4.3. Results and Discussion

The (BQA)PtMe₂I complex shows an unexpected coordination with a planar tri-dentate BQA in a *mer* geometry at the octahedrally coordinated Pt (IV) [1]. Harkins and Peters found this complex to be stable in acetone when stored in the dark, but that it is unexpectedly transformed to the *fac* geometry under irradiation of light.

Computationally optimised geometries, of the ground state *mer* and *fac* structures using DFT and CASSCF methods, are shown in figure 4.7. These compare favourably with experimental X-ray structures. Table 4.1 presents the inter-conversion energies between *mer* and *fac* conformers using different density functionals.

Functional	<i>fac/mer</i> inter-conversion ΔE energy – gas phase (kcal/mol)	<i>fac/mer</i> inter-conversion ΔE energy – solution (kcal/mol)
B3LYP	-0.9	2.9
B3PW91	-0.6	-
X3LYP	-0.9	2.9
PBE1PBE	-0.6	3.1
M06	-5.0	0.5
HCTH147	-0.3	-
wB97	-4.9	-0.9
mPW2PLYP	-3.3	-3.8
B2PLYP	-3.4	-3.9
LCBLYP	-17.0	2.3
LCwPBE	-2.5	1.0
CAMB3LYP	-1.8	2.2

Table 4.1. Density functional dependence on the ΔE optimised S_0 energy (inter-conversion energy) between *mer* and *fac* isomers. Basis set used: SDD on the Pt (60 core electrons), and I (46 core electrons), the 6-31G(d,p) basis on C, N, and H.

For the B3LYP functional the *mer* isomer is $2.9 \text{ kcal mol}^{-1}$ lower in energy than the *fac* using the PCM model, while for the gas phase structures the *fac* is $0.9 \text{ kcal mol}^{-1}$ more stable. Other hybrid functionals such as B3PW91, X3LYP, PBE1PBE and M06 show a similar trend. B2PLYP and mPW2PLYP double hybrid functionals both combining 100% HF exchange and a second order perturbative correction to electron correlation contribution to the DFT calculation, are consistent with each other and show the *fac* isomer as the more stable structure, having a minimum energy lower than the *mer* structure by approximately $3\text{-}4 \text{ kcal mol}^{-1}$ in the gas phase and in solution. Functionals with long-range exchange corrections such as LCBLYP, LCwPBE, and CAMB3LYP show that in the gas phase the *fac* isomer has a lower ground state minimum energy but in solution the *mer* isomer is more stable. This is contrasted with wB97 functional, which also contains a long-range correction, however for both gas phase and calculations in the solution it determines the *fac* isomer as having lower energy and being more stable.

The results show little difference between the density functionals used, showing that both isomers of the (BQA)PtMe₂I complex have comparable ground state energies.

The excited electronic states were obtained using TD-DFT theory as described in section 2.1 of chapter 2. It should be noted that the experimental photochemistry was performed in acetone, though the spectra were recorded in CH₂Cl₂, and no difference in the computed spectra between these two using the PCM model is observed. Experimental spectra taken directly from reference [1] are presented in the figure 4.3.

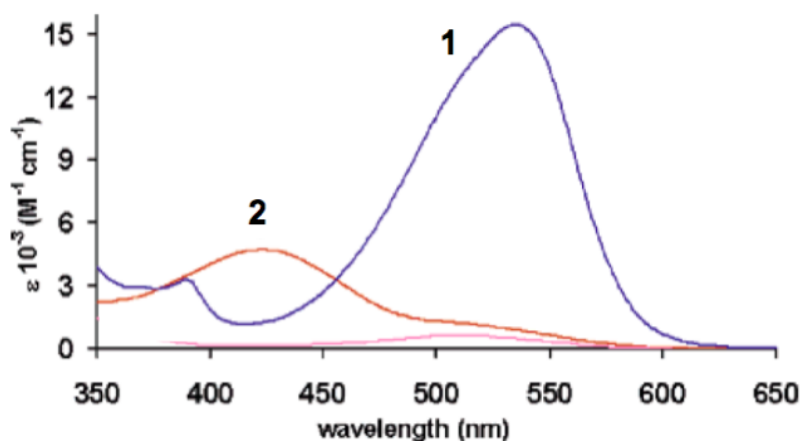


Figure 4.3. Experimental spectra of (1) mer- and (2) fac- isomers of (BQA)PtMe₂I complex in CH₂Cl₂ solvent (picture taken directly from Reference [1]).

Table 4.2 presents the influence of a solvent on the computational spectra using the chosen density functionals. Here the solvent in the PCM model is CH₂Cl₂, to match that used above [1]. The effect of solvent is minimal, with only a small blue-shift observed between the gas phase and PCM results (on average between 0 - 0.05 eV; B3LYP and X3LYP functionals with a maximum of 0.2 eV for the blue shift for *fac* isomer).

Functional	Gas phase (nm)		In solvent (CH ₂ Cl ₂) (nm)	
	<i>mer</i>	<i>fac</i>	<i>mer</i>	<i>fac</i>
B3LYP	530	460	530	430
X3LYP	530	450	520	420
CAMB3LYP	440	360	440	350
LCwPBE	380	310	390	310 ^{sh}
LCBLYP	-	290 ^{sh}	360	300 ^{sh}
M06	-	430	520	410
M062X	-	-	440	340
PBE1PBE	-	-	500	410
wB97	-	300 ^{sh}	380	300 ^{sh}
Experiment	-	-	530	420

Table 4.2. Solvent influence on main spectral features of *mer* and *fac* isomers using Hartree-Fock exchange functionals and functionals involving long range correction.
^{sh} - shoulder band

The computed spectra in solvent using B3LYP, X3LYP and M06 hybrid functionals compare favourably with the experimental ones. There is a small blue shift for the PBE1PBE functional of about 0.2 eV for the *mer* isomer compared with experiment. The hybrid M062X functional and long-range corrected CAMB3LYP show a blue shift of about 0.5 eV. wB97, LCwPBE and LCBLYP long range corrected functionals show a significant blue shift of approximately 1 eV for both isomers. The B3LYP spectra are shown in figure 4.4.

The *mer* form has an intense absorption at 534 nm, which is at 530 nm from TD-B3LYP. The *fac* form has a broad band centered at 422 nm, with a small shoulder at 510 nm. The TD-B3LYP gives this band maximum at 425 nm. The nature of the transitions that give rise to these bands can be determined by examination of the dominant particle-hole configurations of the response eigenvectors, or similarly by determining the natural transition orbitals [22]. There is very little difference between analysis of the excitation using canonical Kohn-Sham orbitals compared to natural transition orbitals.

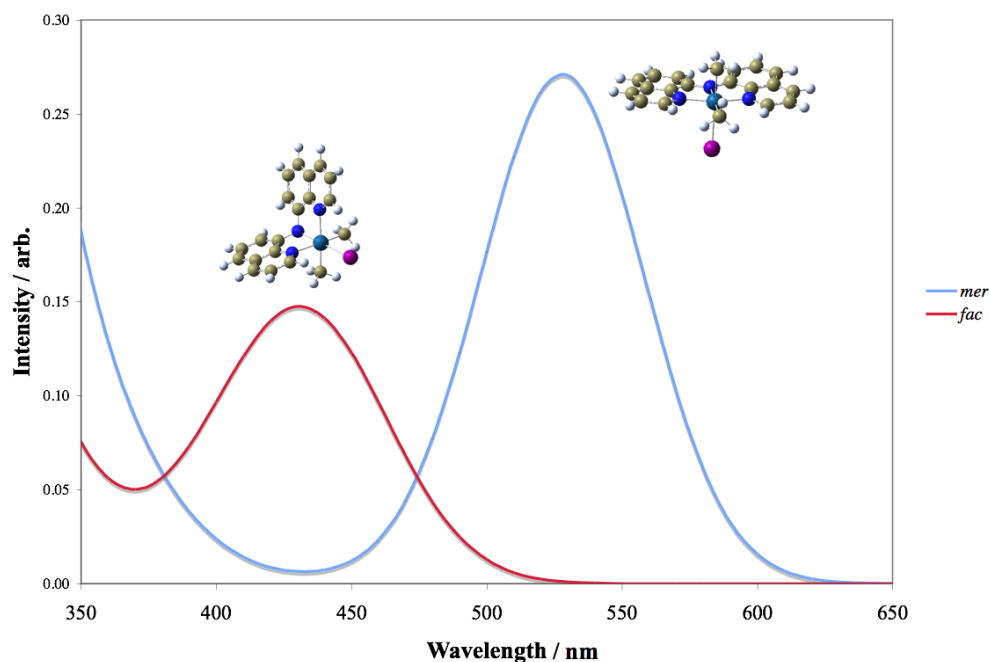


Figure 4.4. Simulated electronic spectra for the *mer* (blue), and *fac* (red) isomers of (BQA)PtMe₂I complex in CH₂Cl₂, obtained from PCM TD-B3LYP by applying a homogenous Gaussian broadening (as described in theory section) to the lowest sixty electronic excited states.

The data given in table 4.3 lists the TD-B3LYP dominant particle-hole configurations (using canonical orbitals) for the *mer* and *fac* isomers.

<i>mer</i>			<i>fac</i>		
State	<i>f</i>	Character	State	<i>f</i>	Character
S ₁ = 2.29 eV	0.0136	(H)(L) 0.121 (H)(L+1) 0.690	S ₁ = 2.78 eV	0.0033	(H)(L+1) 0.534 (H)(L+2) 0.443
S ₂ = 2.35 eV	0.2590	(H)(L) 0.693 (H)(L+1) -0.121	S ₂ = 2.85 eV	0.1178	(H)(L) 0.701
S ₃ = 2.79 eV	0.0023	(H)(L+2) 0.684	S ₃ = 3.03 eV	0.0366	(H)(L+1) -0.449 (H)(L+2) 0.537

Table 4.3. TD-B3LYP (PCM=CH₂Cl₂) excitation energies and oscillator strengths for vertical excitation of *mer* and *fac* isomers. Coefficients of principle particle-hole configurations in response eigenvectors relative to HOMO (H) and LUMO (L) are also given.

The important point with regards to the *mer* form is that the band at 530 nm (predominantly excitation to the S₂ state) involves essentially intra-ligand excitation of π π^* type, and not ligand to metal charge transfer (LMCT) as postulated previously [1]. The π^* orbital contains a very small component that is antibonding with respect to the t_{2g} metal d-orbitals (Figure 4.6). The dominant feature of this state is charge redistribution on the BQA. The main particle-hole configuration of the state involves a donation of electron density from the central amide nitrogen to each π -system on both adjacent quinoline rings. It is also worth noting that the lower dark state (S₁), and all higher dark states in the spectral range up to 400 nm involve this qualitative feature of localised ligand excitation, with charge redistribution across the BQA “backbone”.

In the S₂ state of the complex relaxation involves the BQA ligand “folding” in and the molecule relaxes to a quasi-*fac* form of the complex in the first singlet excited state (S₁) (Figure 4.7). The bright and dark states are very close and may switch in energetic order with different DFT functionals. If the ordering is correct and the bright state is S₂ then obviously there must be a crossing between the S₁ and S₂ states. There is a minimum on the *mer* side of the reaction with BQA slightly non-planar that is reached from the dark state. The S₁ transition state was unable to be located due to the limitation of not having excited Hessian computation in TD-DFT as of yet. Constrained geometry calculations indicate that any barrier will be relatively low. While the driving force in the populated S₂ state forces the system to relax toward *fac*-like geometries, obviously more accurate photochemical dynamics simulations would be required to determine if there is any population transfer to the dark state. However, whether via direct relaxation to the excited *fac* side of the reaction, or transformation over a barrier on a longer timescale, the system ends up at the same point, namely the S₁ *fac* minimum (Figure 4.7). This fact is further emphasised if the bright and dark states are switched in order.

Quadratic Synchronous Transit (QST) calculations for locating a transition state on the ground state potential energy surface were performed. After many searches no direct transition structure linking *mer* and *fac* geometries on the S₀ potential surface was found. However, results obtained show that there is a possible transition state involving dissociation of both methyl groups to create an ethane molecule. This is a standard role for Pt as a catalyst [23] in creating longer chain hydrocarbons from smaller hydrocarbon fragments. For this system the barrier for this reaction path is quite high (57 kcal mol⁻¹),

explaining why it has not been experimentally investigated for this particular complex. It is suspected that any thermal process would have to go through (at least one) reactive intermediate, via the dissociation of the iodine to give a 5-coordinate species. The thermal isomerization is not seen experimentally.

As mentioned previously conical intersections (seams) are regions of strong non-adiabatic coupling that allow for ultrafast sub-picosecond radiationless decay, and the topology around conical intersections affects the internal conversion dynamics of polyatomic molecules. They are very important in modelling not only organic photochemical reactions [24-27] but also in inorganic photochemistry. They appear naturally in coordination complexes via the Jahn-Teller effect, where the two components of an electronically degenerate state give rise to the double cone potential energy surfaces in the space of the Jahn-Teller symmetry breaking modes [28-31]. Indeed in recent years it has become apparent that inorganic photochemistry involving the creation of coordinatively unsaturated species (e.g., metal carbonyl photodissociation [30] provides a natural link between the photochemical and Jahn-Teller fields [29, 31]). General (non-symmetry imposed) intersections have been much less studied in inorganic photochemistry. A conical intersection search using CASSCF has been performed on (BQA)PtMe₂I complex and this type of non-symmetry imposed crossing has been found between the ground and first excited state PESs.

As described above the initial excitation is of $\pi\pi^*$ type and involves a reduction in the conjugation across the planar amido linkage in the BQA ligand. The system then relaxes in this state with the ligand sphere undergoing rearrangement towards a folded BQA conformation. This leads to an excited *fac* minimum. TD-DFT and CASSCF excited geometry optimisations of the S₁ minimum are in good agreement. From this S₁ *fac* minimum the excited molecule could access a conical intersection that connects the S₁ state to the ground state (shown schematically in figure 4.6). A conical intersection search between the ground state and excited S₁ was performed. The S₀/S₁ crossing has been located which allows for efficient radiationless deactivation to the ground state *fac* geometry. The CASSCF energy difference between the S₁ minimum and the minimum energy crossing point is around 10 kcal mol⁻¹, although obviously this value should be treated with caution due to incomplete accounting for dynamic correlation.

This is a naturally occurring photochemical feature of the BQA ligand itself. This type of pathway may be potentially important for other complexes that involve the interesting family of flexible chelating pincer type ligands [11, 12, 14, 15, 18, 32].

Interestingly the same conical intersection seam was found in the bare BQA ligand, and the excited relaxation and subsequent decay is essentially driven by the ligand's photochemistry. CASSCF computations with an active space consisting of 12 electrons in 12 orbitals (427350 CSFs) on the pure ligand indicate that at folded geometries there is an extensive seam of intersection that connects the ground state with a $\pi\pi^*$ state. The orbitals used for CASSCF calculations on the pure ligand were based as those in the full metal complex, on natural orbital occupations. The global minimum energy crossing point on this seam occurs at a CNC angle of 120° , but with the two quinoline groups twisted almost 90° .

Constrained conical intersection searches were performed and it was observed that the intersection seam includes an energetically accessible portion with a small dihedral angle between quinoline groups. This constrained crossing point has a very similar geometry to the intersection in the full metal complex. From the geometries in figure 4.7 it can be seen that the S_1 *fac* minimum occurs with an NPtN angle of 100° , which is more open than at the conical intersection (92°), and at the S_0 minimum (90°). Thus molecular motion moves the system through the S_1 *fac* minimum, crosses from S_1 to S_0 via a radiationless transition in the conical intersection region and finally relaxes to the stable S_0 *fac* minimum. The branching space for the conical intersection in the pure ligand is shown in figure 4.5 and for the full complex in figure 4.6. This is the space (a 2D plane containing the derivative coupling (dc) and gradient difference (gd) vectors) in which the electronic degeneracy is lifted at first-order in vibrational motion. The motion is seen to mainly involve the amido-link in the BQA ligand. Thus, one can see that when the locally excited ligand is driven towards such geometries, the crossing to the ground state becomes favourable.

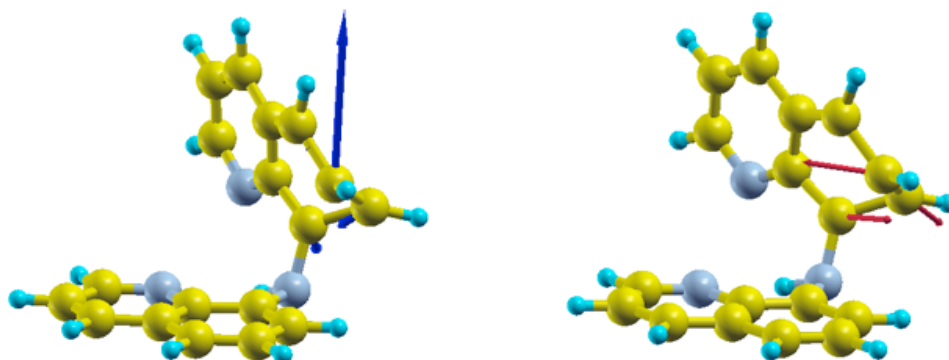


Figure 4.5. Gradient difference and derivative coupling vectors at a point of conical intersection in organic BQA system.

The reaction path linking the conical intersection and the S_0 and S_1 *fac* minima (Figure 4.6), can be determined unambiguously by computing an intrinsic reaction coordinate (IRC). For this system an IRC is computationally expensive but an idea of the downhill path from the conical intersection can be gained from examination of geometry optimisation on the ground and excited state surfaces (using both CASSCF and TD-B3LYP). It is observed that the downhill direction from the conical intersection on S_1 leads directly to the S_1 *fac* minimum, while downhill on S_0 leads to the S_0 *fac* minimum. The topology of conical intersection seam is depicted in figure 4.6, with the angles between gradients of the crossing PESs equal to 75 degrees.

The photoexcited *mer* form involves essentially a redistribution of the π -system on the organic BQA ligand, which “loosens” the conjugation across the amide linkage (the amide nitrogen changes its hybridization from sp^2 to sp^3), and weakens the metal-BQA bonds, via population of orbitals with nominal $M-\pi$ antibonding character.

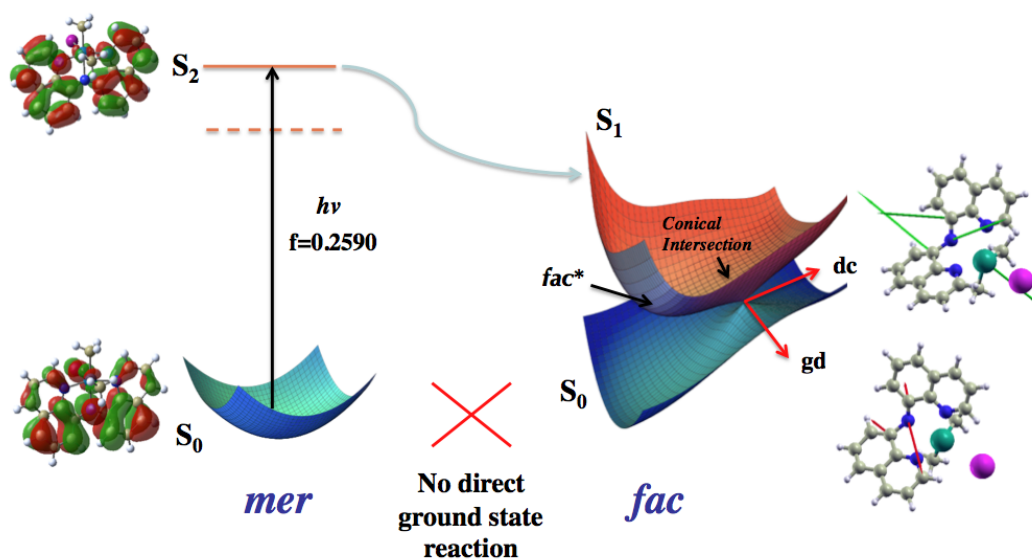
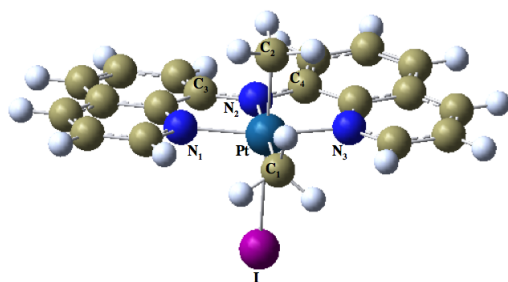


Figure 4.6. Schematic of *mer-fac* photoisomerisation in (BQA)PtMe₂I involving localised $\pi\pi^*$ excitation on the BQA ligand, followed by relaxation to S₁ *fac* minimum. Radiationless deactivation through a sloped conical intersection connecting the S₀ and S₁ states can then occur, to lead to the stable *fac* photoproduct.

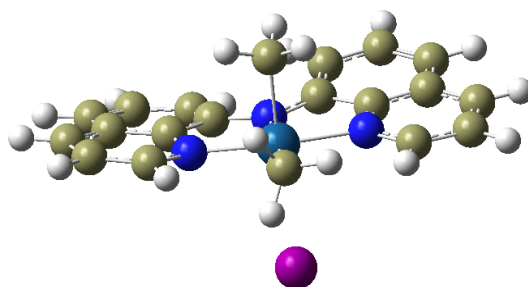
In summary, the metal complex acts as a scaffold for the pincer ligand, and localised excitation on the conjugated ligand drives the intra-ligand folding, which takes the system downhill to the *fac* geometry. At such excited geometries a conical intersection seam is accessible which allows for radiationless decay to the stable *fac* photoproduct observed experimentally. TD-DFT, in conjunction with the polarisable continuum (PCM) solvent model, reproduce the experimental spectra for the *mer* and *fac* isomers well. The nature of the initially populated states for the *mer* isomer as mentioned previously is $\pi\pi^*$ in nature and localised on the BQA ligand. Geometry optimisation shows that the system relaxes in the excited manifold to a *fac* like geometry in the S₁ electronic state. CASSCF calculations show that a conical intersection connects the excited and ground state *fac* species, allowing for radiationless deactivation in *fac*-like geometries.

Figure 4.7 (continued over pages 112-114) presents the optimised geometrical parameters for the critical points involved in the *mer-fac* photoisomerisation of (BQA)PtMe₂I.



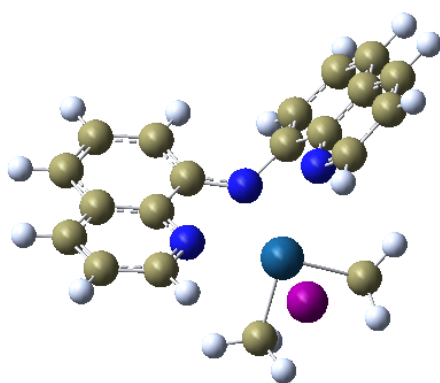
mer S₀ minimum

Pt-C ₁	Pt-C ₂	Pt-I	Pt-N ₁	Pt-N ₂	Pt-N ₃
2.099	2.099	2.871	2.054	2.093	2.059
N ₁ -Pt-N ₃		C ₃ -N ₂ -C ₄		N ₂ -Pt-I	
161.80		133.14		91.33	
<i>Solvent- CH₂Cl₂ (DFT)</i>					
Pt-C ₁	Pt-C ₂	Pt-I	Pt-N ₁	Pt-N ₂	Pt-N ₃
2.100	2.086	2.953	2.062	2.089	2.058
N ₁ -Pt-N ₃		C ₃ -N ₂ -C ₄		N ₂ -Pt-I	
161.83		133.06		90.74	



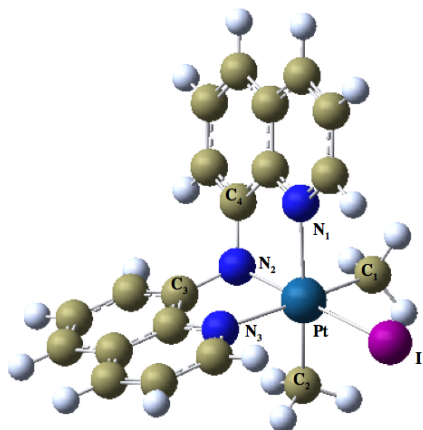
Mer - S₁ minimum TD-B3LYP

Pt-C ₁	Pt-C ₂	Pt-I	Pt-N ₁	Pt-N ₂	Pt-N ₃
2.084	2.103	2.933	2.038	2.099	2.109
N ₁ -Pt-N ₃		C ₃ -N ₂ -C ₄		N ₂ -Pt-I	
132.54		160.94		91.65	



Fac - S₁ minimum CASSCF(14,12)

Pt-C ₁	Pt-C ₂	Pt-I	Pt-N ₁	Pt-N ₂	Pt-N ₃
2.080	2.077	3.220	2.335	2.432	2.778
N ₁ -Pt-N ₃		C ₃ -N ₂ -C ₄		N ₂ -Pt-I	
99.66		127.52		150.37	



fac S₀ minimum

Gas phase (DFT)

Pt-C ₁	Pt-C ₂	Pt-I	Pt-N ₁	Pt-N ₂	Pt-N ₃
2.072	2.072	2.746	2.234	2.073	2.236
N ₁ -Pt-N ₃		C ₃ -N ₂ -C ₄		N ₂ -Pt-I	
97.21		118.15		174.89	

Solvent - CH₂Cl₂ (DFT)

Pt-C ₁	Pt-C ₂	Pt-I	Pt-N ₁	Pt-N ₂	Pt-N ₃
2.072	2.073	2.777	2.226	2.064	2.229
N ₁ -Pt-N ₃		C ₃ -N ₂ -C ₄		N ₂ -Pt-I	
95.83		116.86		176.53	

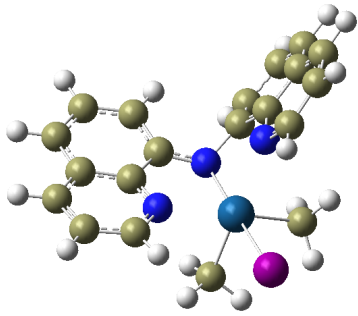
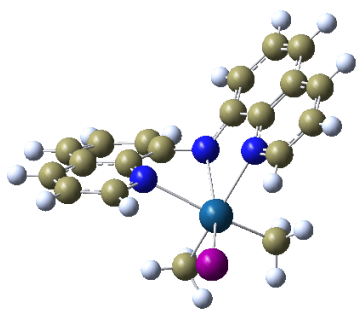
					
<i>Fac - S₁ minimum TD-B3LYP</i>					
Pt-C₁	Pt-C₂	Pt-I	Pt-N₁	Pt-N₂	Pt-N₃
2.070	2.080	2.716	2.266	2.070	2.277
N₁-Pt-N₃		C₃-N₂-C₄		N₂-Pt-I	
99.55		119.15		169.52	
					
<i>Minimum Energy Conical Intersection CASSCF (14,12)</i>					
Pt-C₁	Pt-C₂	Pt-I	Pt-N₁	Pt-N₂	Pt-N₃
2.067	2.071	3.101	2.355	2.482	2.411
N₁-Pt-N₃		C₃-N₂-C₄		N₂-Pt-I	
92.61		125.72		153.24	

Figure 4.7. Optimised geometrical parameters for critical points involved in the *mer-fac* photoisomerization of (BQA)PtMe₂I. S₀ *mer*, and S₀ *fac* optimised using B3LYP, both in gas phase and with CH₂Cl₂ using the PCM model; S₁ optimised *fac* using TD-B3LYP, and CASSCF; S₀/S₁ conical intersection optimised with CASSCF.

4.4. List of references.

- [1] Harkins, S. B.; Peters, J. C., Unexpected Photoisomerization of a Pincer-type Amido Ligand Leads to *facial* Coordination at Pt (IV). *Inorg. Chem.* **2006**, 45, 4316-4318.
- [2] Fryzuk, M. D., Excursions Around the Periodic Table: Ligand Design in Inorganic Chemistry. *Can. J. Chem.* **1992**, 70, 2839-2845.
- [3] Peters, J. C.; Harkins, S. B.; Brown, S. D.; Day, M. W., Pincer-like Amido Complexes of Platinum, Palladium, and Nickel. *Inorg. Chem.* **2001**, 40, 5083-5091.
- [4] Van Koten, G., Tuning the Reactivity of Metals Held in a Rigid Ligand Environment. *Pure Appl. Chem.* **1989**, 61, 1681-1694.
- [5] Huang, M. H.; Liang, L. C., Amido Pincer Complexes of Palladium: Synthesis, Structure, and Catalytic Heck Reaction. *Organometallics* **2004**, 23, 2813-2816.
- [6] Sun, K.; Wang, L.; Wang, Z., Synthesis and Characterization of Amido Pincer Complexes of Lithium and Nickel and Catalysis of the Nickel Complexes in the Kumada Cross-Coupling. *Organometallics* **2008**, 27, 5649-5656.
- [7] Weng, W.; Guo, C. Y.; Celenligil-Cetin, R.; Foxman, B. M.; Ozerov, O. V., Skeletal Change in the PNP Pincer Ligand Leads to a Highly Regioselective Alkyne Dimerization Catalyst. *Chem. Commun.* **2006**, 197-199.
- [8] Harkins, S. B.; Peters, J. C., A Highly Emissive Cu₂N₂ Diamond Core Complex Supported by a [PNP] ligand. *J. Am. Chem. Soc.* **2005**, 127, 2030-2031.
- [9] Harkins, S. B.; Peters, J. C., Base-promoted Benzene C-H Activation Chemistry at an Amido Pincer Complex of Platinum (II). *Organometallics* **2002**, 21, 1753-1755.
- [10] Betley, T. A.; Qian, B. A.; Peters, J. C., Group VIII Coordination Chemistry of a Pincer-Type Bis(8-quinoliny)amido Ligand. *Inorg. Chem.* **2008**, 47, 11570-11582.
- [11] Fout, A. R.; Basuli, F.; Fan, H.; Tomaszewski, J.; Huffman, J. C.; Baik, M.; Mindiola, D. J., A Co₂N₂ Diamond-Core Resting State of Cobalt (I): A Three-Coordinate CoI Synthron Invoking an Unusual Pincer-Type Rearrangement. *Angew. Chem. Int. Edit.* **2006**, 45, 3291-3295.
- [12] Harkins, S. B.; Peters, J. C., Amido-Bridged Cu₂N₂ Diamond Cores that Minimize Structural Reorganization and Facilitate Reversible Redox Behavior

between a $\text{Cu}^{\text{I}}\text{Cu}^{\text{I}}$ and a Class III Delocalized $\text{Cu}^{1.5}\text{Cu}^{1.5}$ Species. *J. Am. Chem. Soc.* **2004**, 126, 2885-2893.

- [13] Maiti, D.; Paul, H.; Chanda, N.; Chakraborty, S.; Mondal, B.; Puranik, V. G.; Lahiri, G. K., Synthesis, Structure, Spectral and Electron-Transfer Properties of Octahedral- $[\text{Co}^{\text{III}}(\text{L})_2]^+ / [\text{Zn}^{\text{II}}(\text{L})_2]$ and Square Planar- $[\text{Cu}^{\text{II}}(\text{L})\{\text{OC}(=\text{O})\text{CH}_3\}]$ Complexes Incorporating Anionic Form of Tridentate bis(8-quinoliny)amine $[(\text{N}^1\text{C}_9\text{H}_6)\text{-C}^1\text{-N}^2\text{-C}_9\text{H}_6\text{N}^3, \text{L}^-]$ Ligand. *Polyhedron* **2004**, 23, 831-840.
- [14] Van Veldhoven, E.; Zhang, H.; Glasbeek, M., (Sub)Picosecond Time-Resolved Fluorescence Depolarization of OLED Compounds Alq_3 , GaQ_3 , and Inq_3 . In *Ultrafast Phenomena XII*, Springer, Ed. New York, 2001; pp 482-484.
- [15] Glasbeek, M.; Humbs, W.; van Veldhoven, E.; Zhang, H., Sub-Picosecond Fluorescence Dynamics of Organic Light-Emitting Diode Tris(8-hydroxyquinoline) Metal Complexes. *Chem. Phys. Lett.* **1999**, 304, 10-18.
- [16] Choudhury, B. PhD Thesis: Organic Light Emitting Devices (OLEDs) and Structurally Integrated Photoluminescence Based Chemical and Biological Sensors Excited by OLEDs. Iowa State University, Ames, Iowa, 2005.
- [17] Furche, F.; Ahlrichs, R., Adiabatic Time-Dependent Density Functional Methods for Excited State Properties. *J. Chem. Phys.* **2002**, 117, 7433-7447.
- [18] Scalmani, G.; Frisch, M. J.; Mennucci, B.; Tomasi, J.; Cammi, R.; Barone, V., Geometries and Properties of Excited States in the Gas Phase and in Solution: Theory and Application of a Time-Dependent Density Functional Theory Polarizable Continuum Model. *J. Chem. Phys.* **2006**, 124, 94107.
- [19] Scalmani, G.; Frisch, M. J., Continuous Surface Charge Polarizable Continuum Models of Solvation. I. General Formalism. *J. Chem. Phys.* **2010**, 132, 114110.
- [20] Frisch, M. J. T., G. W.; Schlegel, H. B.; Scuseria, G. E.; Robb, M. A.; Cheeseman, J. R.; Scalmani, G.; Barone, V.; Mennucci, B.; Petersson, G. A.; Nakatsuji, H.; Caricato, M.; Li, X.; Hratchian, H. P.; Izmaylov, A. F.; Bloino, J.; Zheng, G.; Sonnenberg, J. L.; Hada, M.; Ehara, M.; Toyota, K.; Fukuda, R.; Hasegawa, J.; Ishida, M.; Nakajima, T.; Honda, Y.; Kitao, O.; Nakai, H.; Vreven, T.; Montgomery, Jr., J. A.; Peralta, J. E.; Ogliaro, F.; Bearpark, M.; Heyd, J. J.; Brothers, E.; Kudin, K. N.; Staroverov, V. N.; Kobayashi, R.; Normand, J.; Raghavachari, K.; Rendell, A.; Burant, J. C.; Iyengar, S. S.; Tomasi, J.; Cossi, M.; Rega, N.; Millam, N. J.; Klene, M.; Knox, J. E.; Cross, J. B.; Bakken, V.; Adamo, C.; Jaramillo, J.; Gomperts, R.; Stratmann, R. E.;

- Yazyev, O.; Austin, A. J.; Cammi, R.; Pomelli, C.; Ochterski, J. W.; Martin, R. L.; Morokuma, K.; Zakrzewski, V. G.; Voth, G. A.; Salvador, P.; Dannenberg, J. J.; Dapprich, S.; Daniels, A. D.; Farkas, Ö.; Foresman, J. B.; Ortiz, J. V.; Cioslowski, J.; Fox, D. J., Gaussian 09, Revision A.02. **2009**.
- [21] Frisch, M. J. T., G. W.; Schlegel, H. B.; Scuseria, G. E.; Robb, M. A.; Cheeseman, J. R.; Montgomery, Jr., J. A.; Vreven, T.; Kudin, K. N.; Burant, J. C.; Millam, J. M.; Iyengar, S. S.; Tomasi, J.; Barone, V.; Mennucci, B.; Cossi, M.; Scalmani, G.; Rega, N.; Petersson, G. A.; Nakatsuji, H.; Hada, M.; Ehara, M.; Toyota, K.; Fukuda, R.; Hasegawa, J.; Ishida, M.; Nakajima, T.; Honda, Y.; Kitao, O.; Nakai, H.; Klene, M.; Li, X.; Knox, J. E.; Hratchian, H. P.; Cross, J. B.; Bakken, V.; Adamo, C.; Jaramillo, J.; Gomperts, R.; Stratmann, R. E.; Yazyev, O.; Austin, A. J.; Cammi, R.; Pomelli, C.; Ochterski, J. W.; Ayala, P. Y.; Morokuma, K.; Voth, G. A.; Salvador, P.; Dannenberg, J. J.; Zakrzewski, V. G.; Dapprich, S.; Daniels, A. D.; Strain, M. C.; Farkas, O.; Malick, D. K.; Rabuck, A. D.; Raghavachari, K.; Foresman, J. B.; Ortiz, J. V.; Cui, Q.; Baboul, A. G.; Clifford, S.; Cioslowski, J.; Stefanov, B. B.; Liu, G.; Liashenko, A.; Piskorz, P.; Komaromi, I.; Martin, R. L.; Fox, D. J.; Keith, T.; Al-Laham, M. A.; Peng, C. Y.; Nanayakkara, A.; Challacombe, M.; Gill, P. M. W.; Johnson, B.; Chen, W.; Wong, M. W.; Gonzalez, C.; and Pople, J. A. *Gaussian 03, Revision C.02*, Gaussian, Inc.: Wallingford CT, 2004.
- [22] Martin, R. L., Natural Transition Orbitals. *J. Chem. Phys.* **2003**, 118, 4775-4777.
- [23] Albrecht, M.; Van Koten, G., Platinum Group Organometallics Based on "Pincer" Complexes: Sensors, Switches, and Catalysts. *Angew. Chem. Int. Edit.* **2001**, 40, 3750-3781.
- [24] Garavelli, M., Computational Organic Photochemistry: Strategy, Achievements and Perspectives. *Theor. Chem. Acc.* **2006**, 116, 87-105.
- [25] Robb, M. A.; Bernardi, F.; Olivucci, M., Conical Intersections as a Mechanistic Feature of Organic-Photochemistry. *Pure Appl. Chem.* **1995**, 67, 783-789.
- [26] Robb, M. A.; Garavelli, M.; Olivucci, M.; Bernardi, F., A Computational Strategy for Organic Photochemistry. *Rev. Comp. Chem.* **2000**, 15, 87-146.
- [27] Yarkony, D. R., Conical Intersections: The New Conventional Wisdom. *J. Phys. Chem. A* **2001**, 105, 6277-6293.

- [28] Paterson, M. J.; Hunt, P. A.; Robb, M. A.; Takahashi, O., Non-Adiabatic Direct Dynamics Study of Chromium Hexacarbonyl Photodissociation. *J. Phys. Chem. A* **2002**, 106, 10494-10504.
- [29] Paterson, M. J.; Bearpark, M. J.; Robb, M. A.; Blancafort, L.; Worth, G. A., Conical Intersections: A Perspective on the Computation of Spectroscopic Jahn-Teller Parameters and the Degenerate 'Intersection Space'. *Phys. Chem. Chem. Phys.* **2005**, 7, 2100-2115.
- [30] McKinlay, R. G.; Paterson, M. J., The Jahn-Teller Effect in Binary Transition Metal Carbonyl Complexes. In *The Jahn-Teller Effect: Advances and Perspectives; Springer Series in Chemical Physics*, Köppel, H.; Barentzen, H.; Yarkony, D. R., Eds. Springer: Heidelberg, 2010.
- [31] Bersuker, I. B., *The Jahn-Teller Effect*. Cambridge: 2006; p 616.
- [32] Doux, M.; Mezailles, N.; Ricard, L.; Le Floch, P.; Vaz, P. D.; Calhorda, M. J.; Mahabiersing, T.; Hartl, F., Syntheses, X-ray Structures, Photochemistry, Redox Properties, and DFT Calculations of Interconvertible *fac*- and *mer*-[Mn(SPS)(CO)₃] Isomers Containing a Flexible SPS-based Pincer Ligand. *Inorg. Chem.* **2005**, 44, 9213-9224.

CHAPTER 5

Photochemistry of Chromium Oxalate $[\text{Cr}(\text{C}_2\text{O}_4)_3]^{3-}$

This chapter focuses on the photochemistry of an open shell complex, chromium oxalate $[\text{Cr}(\text{C}_2\text{O}_4)_3]^{3-}$, containing a chromium Cr (III) ion. The photochemistry of systems containing Cr (III) ions has been a subject of increasing investigation over the last century [1-6]. Despite the fact that the main spectroscopic features have been described for a wide range of Cr (III) complexes, the nature of the reactive states and photochemical relaxation mechanisms is still not known for many of them. The Cr (III) complexes studied in this and the next chapter have mainly O_h or pseudo- O_h symmetry on the metal centre. The states of such Cr (III) systems are often discussed in terms of local O_h symmetry. Below we use these labels in the general introduction for this photochemistry, then for chromium oxalate $[\text{Cr}(\text{C}_2\text{O}_4)_3]^{3-}$ in particular the correct D_3 labels, this being a subgroup of O_h and appropriate to isolated $[\text{Cr}(\text{C}_2\text{O}_4)_3]^{3-}$. As described in the chapter 1, the d orbitals in such systems are split into orbitals of t_{2g} and e_g symmetry (as shown on the figure 1.1 in the chapter 1). The Cr (III) ion has 3 electrons occupying the valence 3d shell, thus its electronic configuration will be as follows: $[\text{Ar}]3d^3$. According to Hund's rule, which implies that the electrons in a given subset of orbitals will preferentially fill the empty orbitals first, before pairing with another electron. In $d^3 O_h$ complex electrons will not pair in the t_{2g} orbitals set. Thus the electron configuration of a ground state in d^3 complexes is a quartet shown on the figure 5.1:

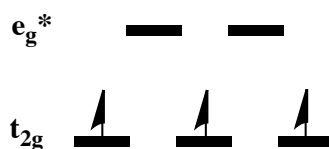


Figure 5.1. Electronic configuration of the $^4A_{2g}$ ground state in $d^3 O_h$ systems.

The possible excited LF electronic states within t_{2g} and e_g orbitals are quartet T_{2g} and T_{1g} , and doublet E_g and T_{1g} states (Figure 5.1). However, in the UV-visible absorption spectra of d^3 systems, only quartet states are populated because the doublet states are both spin and Laporte forbidden. The Laporte rule belongs to the spectroscopic selection rules and states that for molecules with an inversion centre, transitions within a given subshell (for example a single subshell of d orbitals) are electronically forbidden due to the requirement of a change in parity.

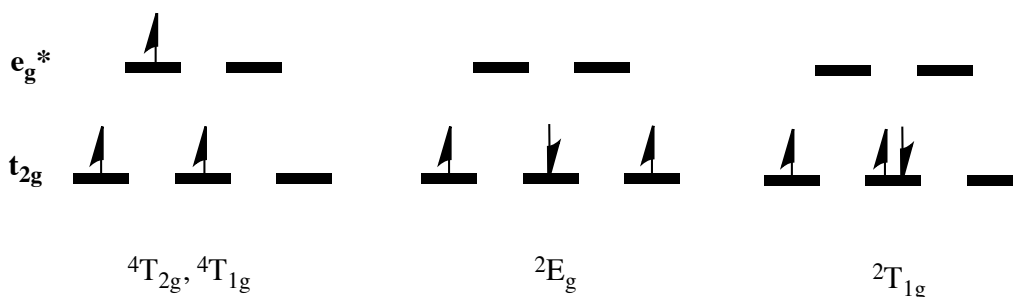


Figure 5.2. Electronic configurations of the ${}^4T_{2g}$ and ${}^4T_{1g}$ and 2E_g and ${}^2T_{1g}$ in d^3 systems.

The pictorial representation of quartet T_{2g} and T_{1g} and doublet E_g and T_{1g} states is presented above. The ordering of the excited states of a system is very important to the photochemistry occurring.

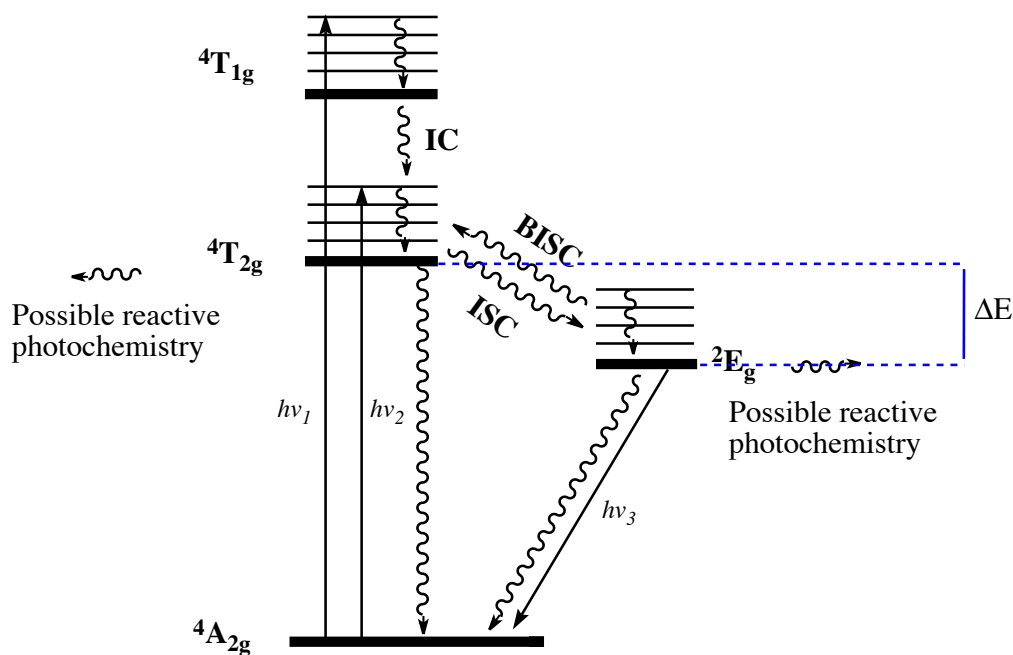


Figure 5.3. Jablonski diagram for O_h Cr(III) complexes – full lines with arrows represent the absorption or emission processes, wavy lines with arrows represent radiationless deactivation processes (intersystem crossing ISC, back intersystem crossings BISC, internal conversion IC). Adapted from the Reference [5].

In reference [5] the author adapted the Jablonski state energy level diagram, to O_h Cr (III) complexes that describes the transitions and processes occurring in these systems (Figure 5.3.). Internal conversion (IC) is a very fast process that can occur between excited states of the same multiplicity, for example ${}^4T_{2g}$ and ${}^4T_{1g}$ states (Figure 5.3). A process very common for O_h Cr (III) complexes is intersystem crossing (ISC) that occurs between states of different multiplicities i.e., between quartet and doublet states. It is usually very efficient and for most of these systems results in 2E_g - ${}^4A_{2g}$ phosphorescence. In these systems spin-orbit coupling is relatively weak (as described in subsection 2.4.2 of chapter 2) and non-radiative transitions i.e. crossing of different spin PESs are driven by small energy gaps. The small energy difference ΔE between ${}^4T_{2g}$ and 2E_g states can lead to a back intersystem crossing process, which can induce emission from ${}^4T_{2g}$ to ${}^4A_{2g}$ state. More details on these processes are presented in the Kane Maguire review [5].

The role of ${}^4T_{2g}$ and 2E_g states is crucial in determining the relaxation pathways and photochemistry of different Cr (III) complexes, however it has not been defined exactly, which states are responsible for the photochemistry observed. One of the most asked questions is how doublet states can influence the photochemistry in these systems. Those studies turned out to be very challenging, both experimentally and computationally [3, 6].

An attempt in determining the ordering of the main excited states influencing the photochemistry and relaxation pathways occurring from these states has been made for the chromium oxalate $[Cr(C_2O_4)_3]^{3-}$ system and, in the chapter 6, on the $[Cr(tn)_3]^{3+}$ and its derivatives. CASSCF and TD-DFT methods described in chapter 2 have been used for the results presented below.

5.1. Introduction

Chromium oxalate $[Cr(C_2O_4)_3]^{3-}$ belongs to the family of complexes in which a Cr (III) ion is surrounded by six oxygen atoms (CrO_6). This is very common for oxide crystals such as ruby, emerald or alexandrite. In ruby Cr (III) ions exchange their position with Al atoms from sets of Al_2O_3 units depending on the concentration of Cr (III). Ruby

proved to be a very efficient fluorescent material at low temperatures due to the presence of Cr (III), and contains approximately 0.003 to 1% of Cr₂O₃ units. Oxygen atoms are coordinated to Cr (III) ions in nearly octahedral (O_h) positions with the site symmetry of Cr as C₃, and the point group symmetry as D₃, the same as in [Cr(C₂O₄)₃]³⁻. A schematic picture of a single Cr(C₂O₄) ring is presented below:

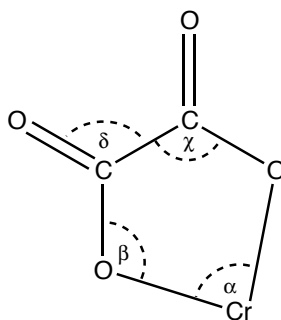


Figure 5.4. Structure of single Cr(C₂O₄) ring.

Often with transition metal complexes, electronic transitions from the ground electronic state to excited states proceed to a manifold of many electronic states that are very close in energy. Identification of the initial absorbing state is very difficult due to this density of states. A description of the initial photochemistry from the initial excited state is challenging due to the number of processes that can occur from this state such as spin-orbit coupling leading to intersystem crossing and Jahn-Teller distortions (described elsewhere). As mentioned previously the ordering of the main absorbing states has a key importance for energy transfer and energy migration processes within a molecule. The excited state characteristics and kinetics of the excited state decay of Cr (III) complexes in oxygen environments have been described in general by Foster, based on the crystal field theory [7]. The ground state for these d³ systems as described previously is an open-shell quartet with 3 electrons occupying t₂ orbital ⁴A₂(t₂³) in the D₃ representation, which is equivalent to a t_{2g} orbital in the O_h symmetry structure (as shown on the figure 5.1.). Depending on the strength of the ligand field the ordering of the first excited states populated can differ. The doublet ²E and ²T₁ states also arising from the t₂³ configuration are often populated for moderate to strong ligand fields complexes [8]. The ²T₁ state is usually higher in energy than ²E but it can go under the ²E state when the symmetry of a molecule is broken by a tetragonal field [9, 10].

For weak ligand fields (for example in borate glasses, some garnets, gallogermanates etc.) the first excited state is usually 4T_2 , which arises from the excitation of one electron from the t orbital in the 4A_2 state to one of the antibonding e orbitals giving the configuration of the 4T state as $(t_2^2e^1)$. In most CrO_6 complexes the excited quartet state 4T_2 appears above the 2E state. The difference in energy between these states ΔE and their ordering is especially important for the emission and thermal relaxation properties of given CrO_6 systems. It is very hard to determine the exact energies of 2E and 4T_2 states [7]. In most CrO_6 complexes the energy difference ΔE (Figure 5.3) between 2E and 4T_2 states is quite small. Small ΔE gaps can lead to the contribution of a thermally activated back intersystem crossing (BISC) process from 2E to 4T_2 states, which can then lead to 4T_2 to 4A_2 emission [10].

The $[Cr(C_2O_4)_3]^{3-}$ incorporated into stoichiometric compounds proved to be a good model system for energy migration investigations due to the lack of exchange interactions, unlike in ruby. Milos and co-workers described important processes occurring in coordinated $[Cr(C_2O_4)_3]^{3-}$ compounds [8]. Narrow luminescence that is common for systems with a 2E state located under the 4T_2 state, has been attributed to the 2E - 4A_2 transition in the $[Cr(C_2O_4)_3]^{3-}$ system. It can also be quenched via thermal population of the 4T_2 state due to the small energy gap. There is also intersystem crossing occurring from the 4T_2 to 2E state, and thermally activated back-intersystem crossing from the 2E to 4T_2 state (as discussed above for ruby).

This chapter will focus on computational investigation of the photochemistry of chromium oxalate $[Cr(C_2O_4)_3]^{3-}$, and mechanisms for radiationless deactivation through the quartet and doublet manifolds as such features have not been studied to date.

5.2. Computational details.

Density functional theory (DFT) was used for determination of the ground state structures of both optical isomers of $[\text{Cr}(\text{C}_2\text{O}_4)_3]^{3-}$ shown on the figure 5.5.

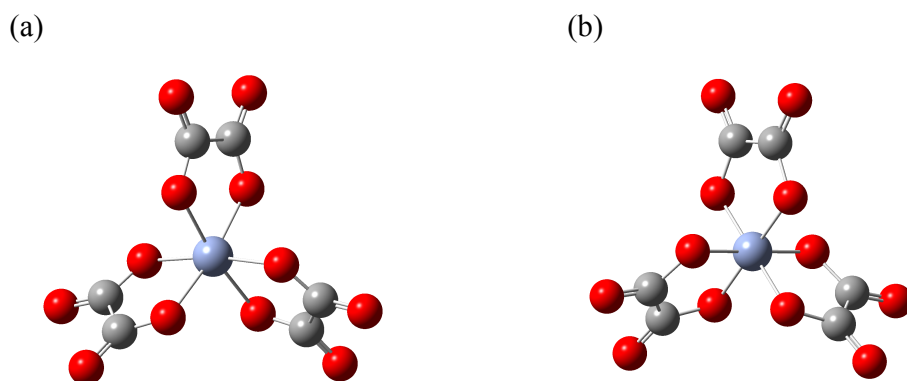


Figure 5.5. Left (a) and right (b) (L-, R-) optical isomers of the $[\text{Cr}(\text{C}_2\text{O}_4)_3]^{3-}$ system.

The B3LYP functional with different basis sets was used for structure optimisations. Structural parameters of both optical isomers were the same (Table 5.1). Polarizable Continuum model (PCM) was used to account for solvation effects. The use of water as a solvent in the optimisation had little to no effect on the geometry of the system. Only a very small shortening of Cr-O and C-C bonds was observed for optimisation in solvent (Table 5.1).

The electronic spectroscopy was studied using the Time-Dependent TD-DFT method. TD-B3LYP and Coulomb Attenuating TD-CAMB3LYP with different basis sets were used to study the UV-Vis spectroscopy of the system. A gaussian broadening factor of 10 and the first 40 vertical excited states were used to calculate the main absorption bands, as described in the chapter 2 and the results are presented in table 5.3. TD-DFT studies on both isomers showed no difference to the main spectral behaviour in the visible region. Infrared spectra using the B3LYP functional with water as a solvent were computed and compared with experimental findings (Table 5.2). Both DFT and TD-DFT calculations were performed using the Gaussian 09 program [11]. To characterise

important excited states of the system Natural Transition Orbitals (NTOs) with TD-B3LYP were used. The NTO method creates a compact orbital representation of the electronic transition density matrix. Unitary transformations are applied separately to occupied and virtual orbitals and from this the best possible representation between the excited electronic density and the hole it has created after excitation is established [12].

Basis set	Cr-O	C-C	C=O	C-O	α	β	χ	δ
R-isomer								
aug-cc-pVTZ	2.01	1.58	1.23	1.29	80	117	113	121
aug-cc-pVTZ ^{a)}	1.99	1.57	1.23	1.29	81	116	113.5	121
cc-pVTZ	2.01	1.57	1.23	1.29	80	117	113	121
SDD – Cr 6-31g(d,p) – O, C	2.01	1.57	1.24	1.30	81	116	113	121
LANL2DZ	2.00	1.58	1.26	1.32	80	118	112	122
CAS ^{b)}	2.01	1.56	1.21	1.27	79	117	113	120
CAS ^{c)}	2.01	1.56	1.21	1.27	79	117	113	120
L-isomer								
aug-cc-pVTZ	2.01	1.58	1.23	1.29	80	117	113	121
aug-cc-pVTZ ^{a)}	1.99	1.57	1.23	1.29	81	116	113.5	121
Experimental data [13]								
Experiment	1.93	1.40	1.28	1.33	90	105	120	120
Experiment	1.88	1.23	1.25	1.47	-	-	-	-
	1.93	1.27	1.17	1.42				
			1.07	1.28				
Experiment	-	1.54	1.23	1.36	-	-	115	121

Table 5.1. Main structural parameters of $[\text{Cr}(\text{C}_2\text{O}_4)_3]^{3-}$ system. DFT calculations performed using B3LYP functional. CASSCF calculations performed using SDD basis set for Cr atom and 6-31g(d,p) for O and C atoms.

^{a)} PCM model with water as a solvent.

^{b)} first variation of active space, as described in the text

^{c)} second variation of active space, as described in the text

Complete Active Space Self Consistent Field (CASSCF) calculations on DFT optimised ground state structures were performed. The SDD basis set on the chromium atom and the 6-31g(d,p) basis set on oxygen and carbon atoms were used for these calculations. Two different active spaces were chosen for comparison. The first active space consisted of 9 electrons and 11 orbitals based on the NTOs. NTOs were generated using a UHF calculation.

The second active space consisted of 9 electrons and 11 orbitals with 1 orbital of p character and 5 metal 3d orbitals and their 4d „antibonding“ counterparts, which were generated using unrestricted B3LYP. Post optimisation, the second active space orbitals were found to no longer resemble metal d orbitals but instead resembled natural orbitals. Geometry optimisations using both active spaces show the same structural parameters of the complex. These are presented in the table 5.1.

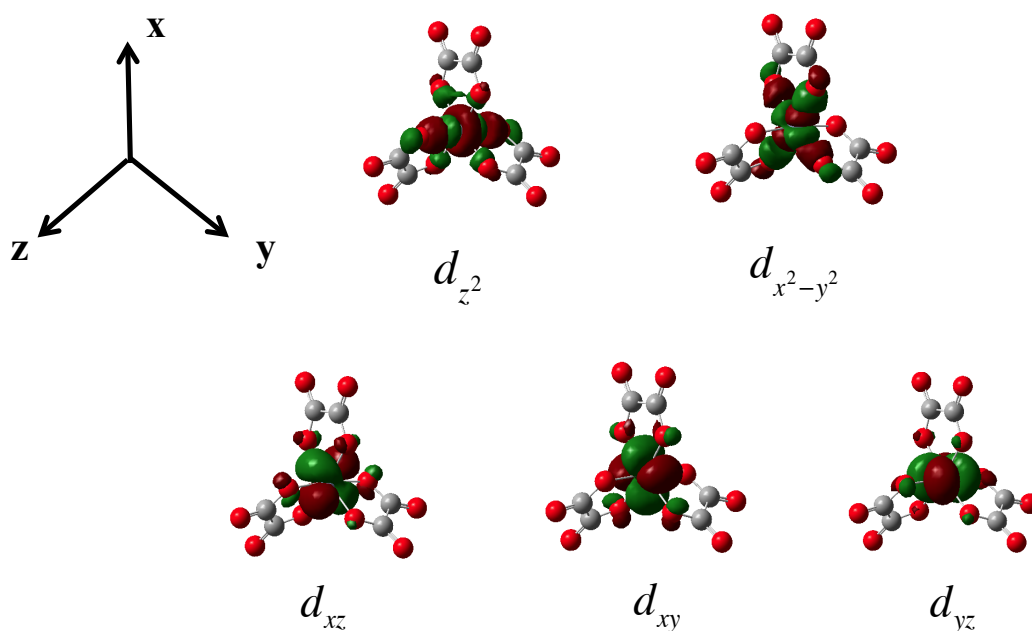


Figure 5.6. Metal orbitals included in the CASSCF active space.

Conical intersection (CI) searches, between the quartet ground state, and first quartet excited state were performed. The structures obtained were found to be insensitive between these active spaces and therefore an active space based on NTOs was used for

all subsequent calculations. The metal orbitals contained in this active space are presented in figure 5.6. The number of configuration state functions (CSFs) obtained for the CASSCF calculations setting the ground state as a quartet multiplicity was equal to 76230 and for the calculations with the ground state set as a doublet multiplicity (will be explained later) 152460 CSFs. To determine the ordering of CASSCF excited states, the 20 lowest excited states were printed and the spin of each was determined using CASSCF with IOp(5/39=1000000) in Gaussian 09.

5.3. Results and discussion.

Infrared (IR) spectroscopy is very important in the structure determination of the system. Table 5.2 presents a comparison between the experimental and calculated infrared spectra of open-shell $[\text{Cr}(\text{C}_2\text{O}_4)_3]^{3-}$ complex. The obtained computational results compared to experimental findings are in very good agreement. Calculated spectra present features between $39\text{-}288\text{ cm}^{-1}$, which experimentally cannot be seen. There are some slight differences to the nature of deformation or vibration for transitions at 891 and 1367 cm^{-1} but they are not really significant. Some of the vibrations for the calculated spectra at 1691 cm^{-1} are mixed. However, overall the performance of DFT in calculating the IR spectrum is surprisingly good for this open-shell system. It should be noted here that there is no scaling applied in the computed IR spectra. Although the studied system is an open-shell system, the DFT results show that it is a good method for the determination of the ground state properties of these transition metal systems, and can be used to investigate their IR spectroscopy.

It is known that chromium oxalate is a photo-chemically stable system. Exposure to visible light has no influence on the absorption spectra. It was experimentally found that the main transitions in $[\text{Cr}(\text{C}_2\text{O}_4)_3]^{3-}$ are as follows: a sharp band at 697 nm attributed to the spin-forbidden ${}^4\text{A}_2\text{-}{}^2\text{E}$ transition, broad spin-allowed d-d transitions at 570 nm and 420 nm attributed to ${}^4\text{A}_2\text{-}{}^4\text{T}_2$ and ${}^4\text{A}_2\text{-}{}^4\text{T}_1$ respectively, and two bands at 270 nm and 224 nm attributed to ligand to metal charge transfer transitions [14].

Computational (PCM)	Assignment	Experiment	Assignment
39	d _s C ₃ axis	-	-
61	d _a C ₃ axis	-	-
219, 222	v(M-O)+d(O-M-O)	-	-
286, 288	v(M-O)+ ring def.	-	-
-	-	313	out of plane ?
340, 347, 353	d(O-C=O)+v(C-C)	358	d(O-C=O)+v(C-C)
389, 400, 402	v _a (M-O)+ring def.	415	v(M-O)+ring def.
484, 486	ring def.+d(O-C=O)	485	ring def.+d(O-C=O)
524	v(M-O)+v(C-C)	543	v(M-O)+v(C-C)
-	-	595	crystal water(?)
796, 805	d(O-C=O)+v(M-O)	798, 810	d(O-C=O)+v(M-O)
891	v(C-C)+d(O-C=O)	893	v _s (C-O)+d(O-C=O)
1264, 1266	v(C-O)+d(O-C=O)	1253	v _s (C-O)+d(O-C=O)
1367	d(O-C=O)+v(C-C)	1387	v _s (C-O)+v(C-C)
1691, 1694	v _a (C=O)+ring def.+d(O-C=O)	1684, 1660	v _a (C=O)
-	-	1708	v _a (C=O)

Table 5.2. Comparison of infrared spectra in cm⁻¹ for calculation with B3LYP (PCM, solvent water) method using cc-pVTZ basis set to experiment [14].

d, d_s, d_a – deformation, symmetric/anti-symmetric deformation

v, v_s, v_a – vibration, symmetric/anti-symmetric vibration

ring def. – ring deformation

Table 5.3 presents the sensitivity of the spectral features of the [Cr(C₂O₄)₃]³⁻ complex to the chosen basis set and the functional using TD-DFT theory. Calculated positions of the visible spectral bands using TD-DFT with different basis sets are within reasonable agreement with experiment. However, the experimental band that was detected at 697 nm is an ⁴A₂-²E transition, and it is not reproduced at all with the standard TD-DFT method used here as it measures only spin-allowed transitions.

The main influence of the basis set on the calculated spectra can be noticed for bands located between 200 nm and 300 nm. The experimental band that is located at 224 nm, is predicted by these calculations to be between 240-280 nm for TD-B3LYP method and between 200-220 nm for TD-CAMB3LYP depending on the basis set used. The band at 270 nm is calculated to be between 270-340 nm for TD-B3LYP and between 250-290 nm for TD-CAMB3LYP again depending on the basis set. The CAM-B3LYP functional was implemented for Rydberg and charge transfer states, and is described in previous chapters.

In the case of this complex CAMB3LYP gives slightly better agreement with the experimental studies for the states located between 200-300 nm and the results are less sensitive to the basis set used. A ligand field (LF) band located at 420 nm and experimentally attributed to ${}^4A_2-{}^4T_1$ transitions is reproduced quite well by all the computational methods used and is slightly blue shifted of approximately 0.15 eV comparing to the experiment. The calculations for this band are less sensitive to the functional and basis set used. LF band located at 570 nm and experimentally attributed to ${}^4A_2-{}^4T_2$ transitions is calculated to be between 480-520 nm showing quite a reasonable blue shift of 0.26-0.4 eV comparing with experimental conjecture. There was no influence of the solvent on the locations of the bands using TD-DFT with all electron cc-pVTZ basis set. A little blue shift was observed for calculations with the PCM model using the aug-cc-pVTZ basis set compared to the gas phase.

It was not possible to definitively resolve the character of all spectral bands with TD-DFT, especially the ones located between 200 nm and 300 nm, due to the large number of states involved in each of them.

These states and the states involved in the other bands didn't have any dominant configuration that would describe the nature of the excitation. Using NTOs it was determined that the nature of the 400 nm and 500 nm bands have d-d character and so are in agreement with the experimental conjecture. Bands between 200 nm and 300 nm are very mixed with some ligand to metal and metal to ligand CT character. It should be noted that TD-DFT is a single-reference method and it does not describe very accurately multiconfigurational states, which are of importance in open-shell systems.

Basis set used	<i>R</i> -isomer	<i>L</i> -isomer	<i>R</i> -isomer	<i>L</i> -isomer	
cc-pVTZ	B3LYP		CAM-B3LYP		EXPERIMENT
	Gas phase				Solution
	240	240	200	200	224
	270	270	250	250	270
	410	410	400	400	420
	520	520	510	510	570
	Solution				697
	240	240	200	200	
	270	270	250	250	
	400	400	390	390	
500	500	480	480		
aug-cc-pVTZ	Gas phase				
	270	360	280	290	
	330	410	410	400	
	400	520	520	510	
	510				
	Solution				
	240	240	200	240	
	280	280	250	280	
	400	400	400	400	
	500	500	500	500	
LANL2DZ	Gas phase				
	260	260	220	220	
	310	310	290	290	
	410	410	390	390	
	510	510	490	490	
Cr – SDD C, O – 6-31g(d,p)	Gas phase				
	280	280	260	240	
	340	340	300sh	340	
	390	390	380	380	
	500	500	480	480	

Table 5.3. Main spectral bands of $[\text{Cr}(\text{C}_2\text{O}_4)_3]^{3-}$ (in nm): TD-DFT using different basis sets (in gas phase and in solution - PCM model with water as a solvent); experimental findings [14].

The drawback of this method in case of this particular system is that it fails to describe the spin-flip transitions and includes a large degree of spin contamination. Table 5.4 shows the spin expectation values of the first 11 vertical excited states using the TD-DFT method and multiconfigurational CASSCF. Note that for multiply degenerate T and E states there is one electronic state per component of the degenerate group, e.g. 3 roots in a CASSCF per one T state. As shown in this table there is a large degree of spin contamination for excited states using TD-B3LYP and TD-CAMB3LYP methods especially for the higher lying states. The CASSCF method as described in chapter 2 obtains pure spin states.

State	B3LYP $\langle \hat{S}^2 \rangle$	B3LYP $\langle \hat{S}^2 \rangle$ PCM	CAMB3LYP $\langle \hat{S}^2 \rangle$	CAMB3LYP $\langle \hat{S}^2 \rangle$ PCM	CASSCF ¹	CASSCF ²
0	3.768	3.768	3.764	3.764	3.750	3.750
1	3.775	3.776	3.767	3.766	3.750	0.750
2	3.774	3.775	3.766	3.765	3.750	0.750
3	3.774	3.775	3.766	3.765	3.750	0.750
4	3.782	3.784	3.769	3.767	3.750	0.750
5	3.782	3.784	3.769	3.767	3.750	0.750
6	3.784	3.785	3.770	3.768	3.750	0.750
7	5.545	5.568	5.662	5.666	3.750	0.750
8	5.544	5.566	5.663	5.666	3.750	0.750
9	5.548	5.570	5.660	5.664	3.750	0.750
10	3.815	3.796	3.771	3.771	3.750	0.750
11	3.819	3.797	3.771	3.771	3.750	3.750

Table 5.4. Spin states of 11 vertical excited states in $[\text{Cr}(\text{C}_2\text{O}_4)_3]^{3-}$: TD-B3LYP and TD-CAMB3LYP used with all electron cc-pVTZ basis set and water as a solvent; CASSCF used with SDD basis set on Cr atom and 6-31g(d,p) on O and C atoms. Note that states between different methods are not equivalent to each other.

¹ground state set to a quartet multiplicity

²ground state set to a doublet multiplicity

There have been two variations of CASSCF calculations performed, first setting the ground state to a quartet multiplicity and the second setting the ground state to a doublet multiplicity. Setting the ground state of a CASSCF calculation to the lower doublet spin

state (expectation value of 0.75) allows the determination of states of the same and a higher spin, in this case quartet spin states. The reasons for this, as described in the theory chapter are common M_s values, which are $\left(-\frac{1}{2}, \frac{1}{2}\right)$. So even if the ground state of a given system is a quartet state, and the calculation will be set as if it would be a doublet ground state, the CASSCF method will still find the correct spin. The population of doublet excitations will not be possible if the ground state of the system is set to a quartet which has M_s values of $\left(-\frac{3}{2}, -\frac{1}{2}, \frac{1}{2}, \frac{3}{2}\right)$ as doublet states do not possess M_s values of $\left(-\frac{3}{2}, \frac{3}{2}\right)$. States that will only be populated in this case will be quartet states and states of higher spin containing common values of M_s , for example a sextet which M_s values are $\left(-\frac{5}{2}, -\frac{3}{2}, -\frac{1}{2}, \frac{1}{2}, \frac{3}{2}, \frac{5}{2}\right)$. The ground state of $[\text{Cr}(\text{C}_2\text{O}_4)_3]^{3-}$ has a quartet spin state, and this is also the outcome of this CASSCF calculation.

There are multiple doublet states present below the first quartet-excited state and this is presented in tables 5.4 (last column - CASSCF) and 5.5. Spin Adapted TD-DFT has been developed that deals with open-shell systems and includes spin-flip transitions however these methods are in their infancy and haven't seen general use as of yet [15, 16].

There are other single-reference alternatives treating these problems such as the Equation-of-Motion Coupled Cluster method (EOM-CC) [17], or Equation-of-Motion – Spin-Flip method (EOM-SF) [18], however according to the literature the quality of the results obtained goes down if the reference ground state is multiconfigurational. This is very often the case in systems with transition metals or other systems with small HOMO-LUMO gaps [17] as in $[\text{Cr}(\text{C}_2\text{O}_4)_3]^{3-}$. Moreover a metal complex of this size is at present too large for CC methods to be routinely applied. Thus, those methods will not be used here and this chapter will focus only on the multiconfigurational approach using CASSCF to describe the nature of electronic transitions and photochemistry of the $[\text{Cr}(\text{C}_2\text{O}_4)_3]^{3-}$ system.

State	Configuration	Energy/kcalmol ⁻¹
0	${}^4A_2(t_2^3)$	0
1	${}^2T(t_2^3)$	48
2	${}^2E(t_2^3)$	58
3	${}^2T(t_2^3)$	61
4	${}^2E(t_2^2e)$	72
5	${}^4T(t_2^2e)$	77

Table 5.5. Ordering of electronically excited states in $[\text{Cr}(\text{C}_2\text{O}_4)_3]^{3-}$ ion (CASSCF: SDD for metal and 6-31g(d,p) basis set for C and O atoms). Vertical energies taken from CASSCF calculation with orbitals state averaged over 12 states.

Multiconfigurational methods are further needed in order to obtain a balanced description of the potential energy surfaces of the system away from the ground state equilibrium geometry.

Table 5.5 presents the ordering of CASSCF populated excited states, their configurations and vertical energies. The states populated are very close in energy and therefore there is a possibility for them to vibronically couple through appropriate molecular vibrations. The energies here should be treated with caution because of a lack of dynamical electron correlation in CASSCF.

There has been no fluorescence observed in systems with chromium oxalates at the temperatures in which phosphorescence is quenched, a feature whose explanation caused much debate in the past. A possible explanation includes non-radiative depopulation of 4T_2 state or relaxation pathways through 2E states [7, 10]. To determine possible PES crossings in this system, conical intersection searches using CAS(9,11) between the quartet ground state 4A_2 and first quartet excited state 4T were performed starting from

the R- optical isomer. It should be noted here that the T state in the D_3 representation is a combination of E and A_1 states, however, the labelling will remain unchanged, and the first quartet excited state will be considered as a 4T state. In our calculations away from the ground state minimum the D_3 symmetry was further broken and we only consider one component of the T state. A peaked conical intersection connecting both 4T and 4A_2 states has been found (Figure 5.8), which implies that there may be an efficient transition from the excited state to the ground state PES. The structure of $[\text{Cr}(\text{C}_2\text{O}_4)_3]^{3-}$ at the conical intersection point can be characterised by an elongation and rupture of a single Cr-O bond (Figure 5.7).

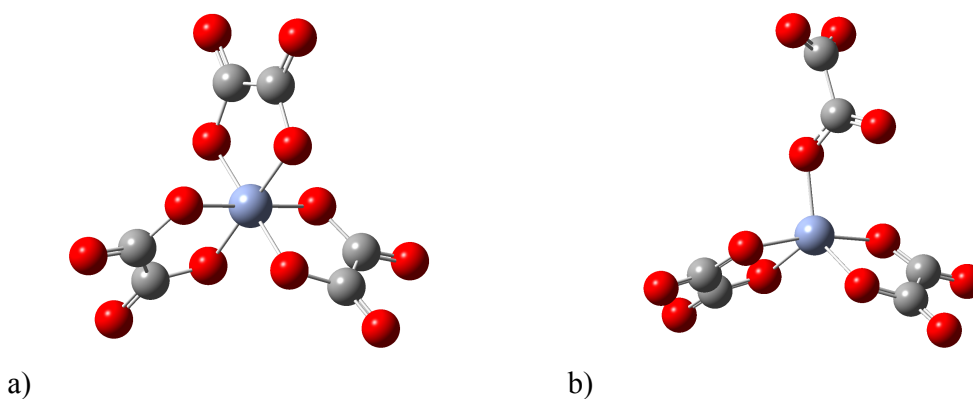
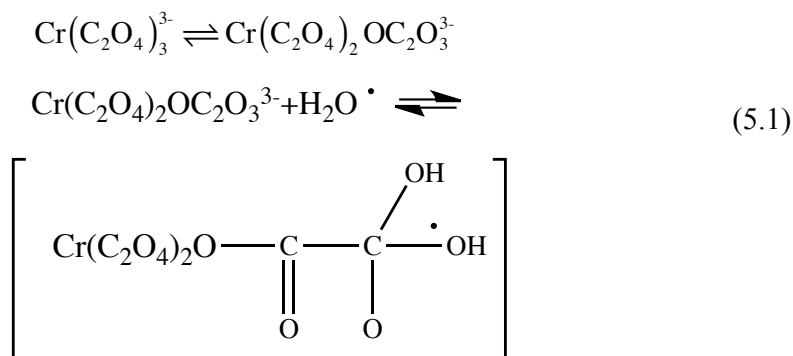


Figure 5.7. The structure of the $[\text{Cr}(\text{C}_2\text{O}_4)_3]^{3-}$ complex a) ground state, b) at the conical intersection point.

Similar behaviour i.e. dissociation of a single Cr-O bond was noted for the oxygen exchange process between $[\text{Cr}(\text{C}_2\text{O}_4)_3]^{3-}$ and a water, which can be thought of as parallel to racemization, as shown in the reaction scheme (Equation 5.1) [19].



In experimental studies it was assumed that the rupture of Cr-O bond is a result of photoactivation of $[\text{Cr}(\text{C}_2\text{O}_4)_3]^{3-}$ [19]. The above computational findings prove that indeed this is the case. The coordination at the metal center of the $[\text{Cr}(\text{C}_2\text{O}_4)_3]^{3-}$ system at the point of conical intersection is quasi-trigonal-bipyramidal (quasi-TBP) (Figure 5.8). This structure is similar to a Jahn-Teller active structure that will efficiently distort to a minimum on the ground state PES. The ruptured end of C_2O_4 ligand can clip back on to form either R-isomer or L-isomer of the complex (Figure 5.8) as can be seen by considering a linear combination of the branching space vectors shown in figure 5.8.

This mechanism could explain the racemization process of this system, which was experimentally found to be photo-induced [19, 20]. This is supported by the fact that the character of the conical intersection involved in this reaction is peaked which could lead to more than one photoproduct on the ground state PES, i.e., the original stereoisomer or its alternative form.

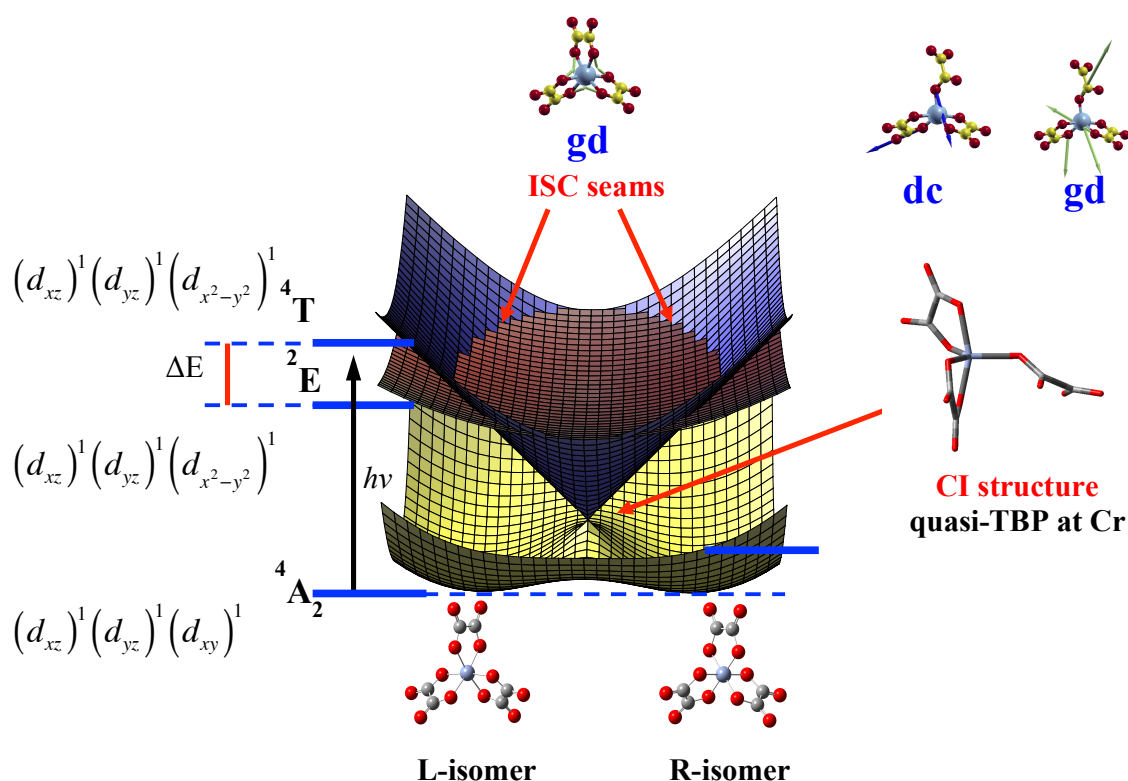


Figure 5.8. Potential energy surfaces of $[\text{Cr}(\text{C}_2\text{O}_4)_3]^{3-}$ complex.

The presence of this conical intersection between ${}^4T(d_{xz})^1(d_{yz})^1(d_{x^2-y^2})^1$ and ${}^4A_2(d_{xz})^1(d_{yz})^1(d_{xy})^1$ states is supported by the fact that at the TBP geometries of the metal centre (found at the point of conical intersection) $d_{x^2-y^2}$ and d_{xy} orbitals become degenerate with one electron spread over both. Distortion from this point removes the degeneracy in these orbitals and the system moves onto the ground state PES of the $(d_{xz})^1(d_{yz})^1(d_{xy})^1$ configuration. To be clear again, the conical intersection occurs between only one component of 4T state that has a $(d_{xz})^1(d_{yz})^1(d_{x^2-y^2})^1$ configuration. Figure 5.9 presents the orbital configurations of the ${}^4T_{2g}$ state when the molecule is distorted from O_h to TBP via breakage of a single coordination site. As described above the $d_{x^2-y^2}$ and d_{xy} orbitals become degenerate in the TBP structure.

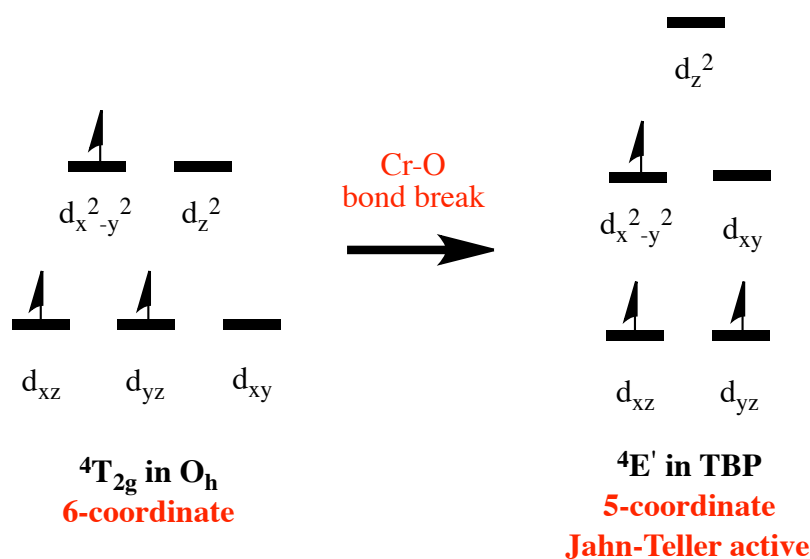


Figure 5.9. Orbital configuration of ${}^4T_{2g}$ state, ${}^4(A_1 \oplus E)$ in D_3 .

Luminescence in the Cr (III) oxalate systems has been found to be dependent on the temperature and concentration of chromium oxalate ions in these systems. Milos and co-workers reviewed the behaviour of the luminescence in such systems and noted that in concentrated oxalate systems for temperatures above 4.2 K the strength of the luminescence falls, and for the systems where Cr (III) is doped into host lattices for

temperatures above 100 K, the luminescence is quenched and the back intersystem crossing from the 2E to the 4T_2 state, which is thermally induced, becomes important [8].

CAS(9,11) calculations have been performed to determine the presence of 2E - 4T intersystem crossing seams. The intersection seams between the PESs of a quartet and doublet excited states have been located, which did not involve any dramatic change in geometrical parameters confirming the experimental findings (Figure 5.8), i.e. the minimum energy points on the seam correspond to reasonably well defined R- or L-optical isomers. This intersystem crossing is equivalent for both R- and L- isomers of $[\text{Cr}(\text{C}_2\text{O}_4)_3]^{3-}$. The presence of this ISC is not surprising because the electronic configuration of the 4T state is the same as the electronic configuration of the 2E state, namely $(d_{xz})^1(d_{yz})^1(d_{x^2-y^2})^1$. Crossing from one state to another would not require any change in orbital occupation but only flipping of the spin.

As described in the chapter 2 of this thesis, spin-orbit coupling (SOC) becomes important for heavy elements. For 1st row transition metal valence electrons the SOC is expected to be quite weak and therefore perturbs pure spin states. Indeed, experimental studies on the optical absorption spectrum of $[\text{Cr}(\text{C}_2\text{O}_4)_3]^{3-}$ system doped in $\text{NaMg}[\text{Al}(\text{C}_2\text{O}_4)_3]\cdot 8\text{H}_2\text{O}$ show splitting of about $2\text{-}3\text{ cm}^{-1}$, of doublet bands arising from ${}^2E_g(\text{O}_h)$ in the α - and π spectrum, which is quite small [21]. Thus we can assume that the spin-orbit coupling in this system is weak and the driving force for the intersystem crossing occurring in it would be a small ΔE energy difference between the states.

To computationally determine the size of spin-orbit coupling, one can use the methods as described in section 2.4.2 of chapter 2. Unfortunately, the size of system studied here, and quite large active spaces preclude the extensive calculation of spin-orbit coupling using perturbation theory. However, we again note that for the non-radiative ISC channels, the location of the crossing seams is of paramount importance. Future studies would require building a model system and possibly using a smaller CAS active space to calculate the spin-orbit contribution.

The importance of including the spin-orbit interaction can be crucial for determining the mechanisms of the ISC via dynamical simulation. Quite recently it was shown that the spin-orbit coupling can be very important for the ultrafast dynamics of some systems, even if its magnitude is relatively small [22, 23].

5.4. List of references.

- [1] Geiger, D. K., Chromium 1994. *Coord. Chem. Rev.* **1996**, 152, 359-392.
- [2] Kirk, A. D., Stereochemistry and Steric Effects in the Photosubstitutions of Chromium(III) Complexes, and Their Utility as Probes of Mechanism. *Comm. Inorg. Chem.* **1993**, 14, 89-121.
- [3] Kirk, A. D., Photochemistry and Photophysics of Chromium (III) Complexes. *Chem. Rev.* **1999**, 99, 1607-1640.
- [4] Forster, L. S., The Photophysics of Chromium (III) Complexes. *Chem. Rev.* **1990**, 90, 331-353.
- [5] Kane-Maguire, N. A. P., Photochemistry and Photophysics of Coordination Compounds: Chromium. *Top Curr Chem* **2007**, 280, 37-67.
- [6] Kirk, A. D.; Irwin, G., Intermediates in Chromium (III) Photochemistry. *Coord. Chem. Rev.* **2001**, 211, 25-43.
- [7] Forster, L. S., Excited State Relaxation of Cr (III) in Oxygen Environments *Coord. Chem. Rev.* **2003**, 248, 261-272.
- [8] Milos, M.; Kairouani, S.; Rabaste, S.; Hauser, A., Energy Migration within the 2E state of Cr^{3+} . *Coord. Chem. Rev.* **2008**, 252, 2540-2551.
- [9] Ghaith, A. M.; Forster, L. S.; Rund, J. V., Excited-State Ordering and Solvatochromic Emission in (Pyridine) Chromium (III) and (Poly(Pyridine)) Chromium (III) Complexes. *Inorg. Chem.* **1987**, 26, 2493-2498.
- [10] Forster, L. S., Thermal Relaxation in Excited Electronic States of d^3 and d^6 Metal Complexes. *Coord. Chem. Rev.* **2002**, 227, 59-92.
- [11] Frisch, M. J. T., G. W.; Schlegel, H. B.; Scuseria, G. E.; Robb, M. A.; Cheeseman, J. R.; Scalmani, G.; Barone, V.; Mennucci, B.; Petersson, G. A.; Nakatsuji, H.; Caricato, M.; Li, X.; Hratchian, H. P.; Izmaylov, A. F.; Bloino, J.; Zheng, G.; Sonnenberg, J. L.; Hada, M.; Ehara, M.; Toyota, K.; Fukuda, R.; Hasegawa, J.; Ishida, M.; Nakajima, T.; Honda, Y.; Kitao, O.; Nakai, H.; Vreven, T.; Montgomery, Jr., J. A.; Peralta, J. E.; Ogliaro, F.; Bearpark, M.; Heyd, J. J.; Brothers, E.; Kudin, K. N.; Staroverov, V. N.; Kobayashi, R.; Normand, J.; Raghavachari, K.; Rendell, A.; Burant, J. C.; Iyengar, S. S.; Tomasi, J.; Cossi, M.; Rega, N.; Millam, N. J.; Klene, M.; Knox, J. E.; Cross, J. B.; Bakken, V.; Adamo, C.; Jaramillo, J.; Gomperts, R.; Stratmann, R. E.; Yazyev, O.; Austin, A. J.; Cammi, R.; Pomelli, C.; Ochterski, J. W.; Martin, R.

- L.; Morokuma, K.; Zakrzewski, V. G.; Voth, G. A.; Salvador, P.; Dannenberg, J. J.; Dapprich, S.; Daniels, A. D.; Farkas, Ö.; Foresman, J. B.; Ortiz, J. V.; Cioslowski, J.; Fox, D. J., Gaussian 09, Revision A.02. **2009**.
- [12] Martin, R. L., Natural Transition Orbitals. *J. Chem. Phys.* **2003**, 118, 4775-4777.
- [13] Fujita, J.; Martell, A. E.; Nakamoto, K., Infrared Spectra of Metal Chelate Compounds. VI. A Normal Coordinate Treatment of Oxalato Metal Complexes. *J. Chem. Phys.* **1962**, 36, 324-331.
- [14] Condrate, R. A.; Forster, L. S., The Spectra of Chromium Oxalate Crystals. *J. Mol. Spec.* **1967**, 24, 490-499.
- [15] Li, Z. D.; Liu, W. J., Spin-Adapted Open-Shell Random Phase Approximation and Time-Dependent Density Functional Theory. I. Theory. *J. Chem. Phys.* **2010**, 133, 064106.
- [16] Li, Z. D.; Liu, W. J.; Zhang, Y.; Suo, B. B., Spin-Adapted Open-Shell Time-Dependent Density Functional Theory. II. Theory and Pilot Application. *J. Chem. Phys.* **2011**, 134, 134101.
- [17] Krylov, A. I., Equation-of-Motion Coupled-Cluster Methods for Open-Shell and Electronically Excited Species: The Hitchhiker's Guide to Fock Space. *Ann. Rev. Phys. Chem.* **2008**, 59, 433-462.
- [18] Krylov, A. I., Spin-Flip Equation-of-Motion Coupled-Cluster Electronic Structure Method for a Description of Excited States, Bond Breaking, Diradicals, and Triradicals. *Acc. Chem. Res.* **2006**, 39, 83-91.
- [19] Krishnamurty, K. V.; Harris, G. M., The Chemistry of the Metal Oxalato Complexes. *Chem. Rev.* **1961**, 61, 213-246.
- [20] Spees, S. T.; Adamson, A. W., Photochemistry of Complex Ions. II. Photoracemization. *Inorg. Chem.* **1962**, 1, 531-539.
- [21] Schönherr, T.; Spanier, J.; Schmidtke, H. H., Trigonal Level Splittings of Cr³⁺ Doped in NaMg[Al(Ox)₃]·8H₂O Single-Crystals. *J. Phys. Chem.* **1989**, 93, 5969-5972.
- [22] Penfold, T. J.; Worth, G. A., The Effect of Molecular Distortions on Spin-Orbit Coupling in Simple Hydrocarbons. *Chem. Phys.* **2010**, 375, 58-66.
- [23] Parker, D. S. N.; Minns, R. S.; Penfold, T. J.; Worth, G. A.; Fielding, H. H., Ultrafast Dynamics of the S₁ Excited State of Benzene. *Chem. Phys. Lett.* **2009**, 469, 43-47.

CHAPTER 6

**Photochemistry, spectroscopy and photoproducts
of the aquation reaction of Chromium (III) tris-1,3-diaminopropane
[Cr(tn)₃]³⁺ complex and its derivative trans-[Cr(tn)₂(CN)₂]⁺**

Chromium (III)-amine complexes have been the subject of academic study for many years [1, 2]. Their photochemistry, as well as the photochemistry of all Cr (III) complexes as described in the previous chapter caused a lot of debate in the past and even still many aspects are unknown and cause controversy [3-5]. Initially it was quite cryptic which excited states are responsible for the photochemistry of Cr (III) complexes and it proved a challenge to experimentalists to accurately probe the photochemical pathways/relaxations of these systems. It is now widely believed that the photochemistry of Cr (III) amine systems can occur from a quartet state with participation from the doublet states [5, 6]. However, extensive computational studies are needed to describe the nature of the states and mechanism of their photoreactions.

The aquation reactions of Cr (III) amine systems, which involve incorporation of water molecules to the metal centre, are found to be photoinduced, and can occur through different pathways in the quartet and doublet spin manifolds providing different photoproducts. The incorporation of a water molecule can cause the displacement of other ligands present. The common feature is that the process of photoaquation is very efficient, and certain percentages of the reaction can be quenchable via the photoactive doublet states or different reaction quenchers which are substances that absorb fluorescence emission of close lying molecules [3, 7, 8]. The type of quencher can influence the final photostereochemistries of the studied systems.

There are many reports on groups of complexes containing different amine ligand analogues such as NH_3 , cyclam (cyclam = 1,4,8,11-tetraazacyclotetradecane), en (en = 1,2-diaminoethane) or tn (tn = 1,3-diaminopropane) [2, 9, 10]. The ring size and thus the steric effects of the ligands can influence the quantum yields of the reactions [7]. Studies show that these systems possess similar spectral properties. However, their photochemistry and ligand substitution reactions may be quite different depending on the type of ligands present. There has been a general rule introduced by Kirk in accordance to ligand substitution reactions of Cr (III) amine systems (obeyed also for strong field d^6 complexes) stating that the ligand that tries to enter the coordination centre will preferentially occupy the trans position with respect to the leaving ligand. Many features of photosubstitution reactions and their stereochemical aspects are presented well by Vanquickenborne and co-workers on the photochemistry of Cr (III)

ammine complexes and this will be discussed later in accordance to the systems considered here.

This chapter will focus on the computational investigation using the TD-B3LYP and CASSCF methods on the spectroscopy and mechanisms of the photoaquation reactions of Cr(III) complexes containing tn ligands.

6.1. Photochemistry and photoaquation of $[\text{Cr}(\text{tn})_3]^{3+}$.

The tn ligand (tn = 1,3-diaminopropane) (Figure 6.1) belongs to the group of bidentate ligands described previously in the introduction of this thesis which can bond to and form a ring with a metal centre through two nitrogen atoms.

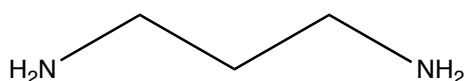


Figure 6.1. Structure of tn (1,3-diaminopropane) ligand.

Tn ligands can adopt different structures when coordinated to a metal. In $[\text{Cr}(\text{tn})_3]^{3+}$, two tn ligands exhibit a chair conformation and one tn ligand exhibits a twist boat conformation as shown in figure 6.2 [11].

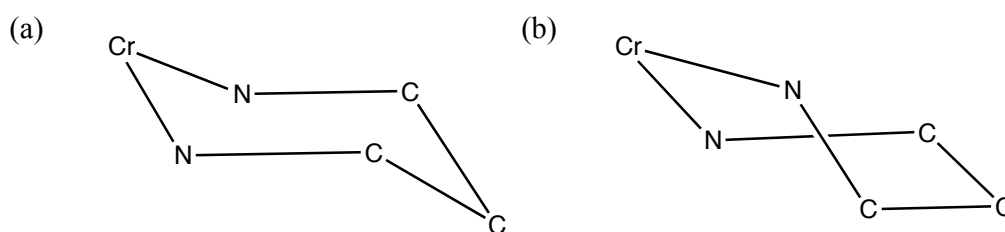


Figure 6.2. Conformations of tn ligands in $[\text{Cr}(\text{tn})_3]^{3+}$ complex (a) chair, (b) twist boat.

The full structure of this complex is presented in figure 6.3. The metal centre is almost octahedral although the full complex has minimal symmetry (C_1).

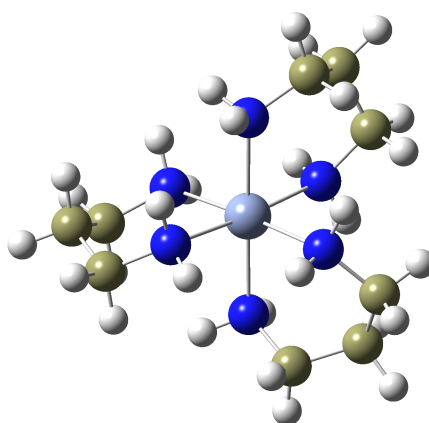
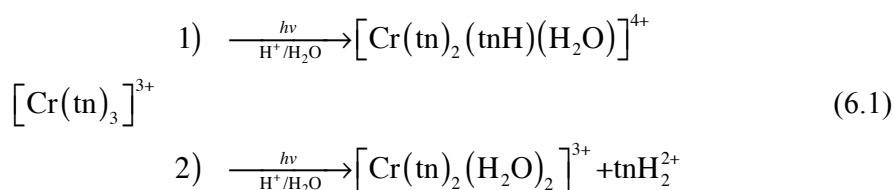


Figure 6.3. Structure of $[\text{Cr}(\text{tn})_3]^{3+}$ complex.

Early experimental studies on $[\text{Cr}(\text{tn})_3]^{3+}$ suggested two possible main products of the photoaquation reaction of this complex, one being $[\text{Cr}(\text{tn})_2(\text{tnH})(\text{H}_2\text{O})]^{4+}$ and the other the $[\text{Cr}(\text{tn})_2(\text{H}_2\text{O})_2]^{3+}$ both in their cis- and trans- forms [12]. Initially it was thought that the production of $[\text{Cr}(\text{tn})(\text{tnH})_2(\text{H}_2\text{O})_2]^{5+}$ could occur via secondary photolysis or thermal aquation of the first photoproduct, $[\text{Cr}(\text{tn})_2(\text{tnH})(\text{H}_2\text{O})]^{4+}$, however this was ruled out due to the very low conversions and great stability of irradiated samples [12]. The formation of diaquo products through thermal aquation of the first photoproduct was also excluded due to the very slow rate of the process. It was then suggested that the formation of $[\text{Cr}(\text{tn})_2(\text{H}_2\text{O})_2]^{3+}$ occurs directly from the photoaquation of $[\text{Cr}(\text{tn})_3]^{3+}$. Equation 6.1 (taken from reference [12]) shows the mechanism of this reaction is:



The formation of $[\text{Cr}(\text{tn})_2(\text{tnH})(\text{H}_2\text{O})]^{4+}$ occurred with a low quantum yield of 0.15, which the authors attempted to explain as a result of the quite high stability of tn ligand that turned out to be much more stable than other amine analoges. This was due to its conformation of a six membered chair ring, as in cyclohexane, while bonding to the metal that also made it a much poorer leaving group compared to other amine analoges [13, 14]. The quantum yield of the $[\text{Cr}(\text{tn})_2(\text{H}_2\text{O})_2]^{3+}$ product was equal to 0.04. The hydroxide ion was present in the mixture [12] and is the reaction quencher. The

percentage of the reaction that occurred via a doublet was 78% [7]. There have been other systems studied as possible quenchers of the given photoreaction such as $[\text{Cr}(\text{CN})_6]^{3-}$, $[\text{Cr}(\text{C}_2\text{O}_4)_3]^{3-}$ (looked at in previous chapter) or the $\text{Na}[\text{Cr}(\text{tn})(\text{CN})_4]$ complex [13, 14]. The photoaquation reaction of $[\text{Cr}(\text{tn})_3]^{3+}$ was then reinvestigated, together with extensive studies on reaction quenching by the $\text{Na}[\text{Cr}(\text{tn})(\text{CN})_4]$ and a comparison with the OH^- quencher. This complex turned out to be very efficient quencher of the reaction that does not absorb over the wavelength range 450-735 nm and can be used over a pH range of 2-10, unlike OH^- that causes very high pH of solutions. The product mixture of the reinvestigated complex contained the initial $[\text{Cr}(\text{tn})_3]^{3+}$, *cis*- and *trans*- isomers of $[\text{Cr}(\text{tn})_2(\text{tnH})(\text{H}_2\text{O})]^{4+}$ and $[\text{Cr}(\text{tn})(\text{tnH})_2(\text{H}_2\text{O})_2]^{5+}$ complex that was not observed before and another unidentified secondary photoproduct. The use of a quencher and the type of quencher seemed to have an influence on the *cis*- and *trans*- isomer ratios of the photoproducts. The quantum yield was the same for doublet- and quartet- state irradiation. The earlier effect of the increase in the percentage of *cis*- isomer in the red edge of the spectrum of the quartet absorption band was not reproduced at all. The authors stated that previous results may have been due to possible errors in the peak area measurements or more likely to parallel thermal reactions during photolysis [14]. The aquation reaction of $[\text{Cr}(\text{tn})_3]^{3+}$ through the transition state pathway on a ground state PES was not observed experimentally and was excluded due to a steric effect blocking the entering ligand [2].

This chapter will focus on the computational study on the explanation of some aspects of the mechanisms of photoproducts formation in the photoaquation reaction of $[\text{Cr}(\text{tn})_3]^{3+}$ and their photochemistry.

6.1.1. Computational details.

DFT structure optimisations of $[\text{Cr}(\text{tn})_3]^{3+}$ and its possible photoproducts such as *cis*- and *trans*- $[\text{Cr}(\text{tn})_2(\text{H}_2\text{O})_2]^{3+}$ and *cis*- and *trans*- $[\text{Cr}(\text{tn})_2(\text{tnH})(\text{H}_2\text{O})]^{4+}$ have been performed using the B3LYP functional with two basis sets variations: first an SDD basis set for Cr atom and 6-31g(p,d) for C, O, N and H atoms and second an all electron cc-pVTZ basis set by Peterson [15] for all the atoms present in the system. These results did not differ significantly between different basis sets used for B3LYP calculations.

Only slight elongation of the bond lengths was observed for the computational data comparing to experiment.

Method	Cr-N₁	Cr-N₂	Cr-N₃	Cr-N₄	Cr-N₅	Cr-N₆
B3LYP ^{a)}	2.170	2.172	2.153	2.174	2.139	2.149
B3LYP ^{b)}	2.167	2.171	2.148	2.169	2.134	2.142
CAS ^{b)}	2.187	2.178	2.189	2.183	2.163	2.170
Experiment	2.094	2.100	2.087	2.098	2.104	2.096
Method	N₁-C₁	N₂-C₂	N₃-C₃	N₄-C₄	N₅-C₅	N₆-C₆
B3LYP ^{a)}	1.518	1.518	1.517	1.518	1.515	2.149
B3LYP ^{b)}	1.522	1.521	1.521	2.169	1.518	1.528
CAS ^{b)}	1.509	1.509	1.507	1.508	1.506	1.517
Experiment	1.494	1.494	1.486	1.506	1.482	1.462
Method	C₁-C_{1,2}	C₂-C_{1,2}	C₃-C_{3,4}	C₄-C_{3,4}	C₅-C_{5,6}	C₆-C_{5,6}
B3LYP ^{a)}	1.519	1.518	1.519	1.518	1.519	1.530
B3LYP ^{b)}	1.524	1.524	1.524	1.523	1.525	1.540
CAS ^{b)}	1.520	1.521	1.521	1.520	1.533	1.522
Experiment	1.496	1.511	1.497	1.504	1.489	1.436
Method	N₁-Cr-N₂	N₁-Cr-N₃	N₁-Cr-N₄	N₁-Cr-N₅	N₁-Cr-N₆	N₂-Cr-N₆
B3LYP ^{a)}	88.18	89.64	91.62	89.77	177.75	90.75
B3LYP ^{b)}	87.68	89.81	91.85	89.88	177.01	91.06
CAS ^{b)}	87.85	89.45	91.68	90.06	176.98	90.80
Experiment	90.58	91.46	93.27	87.54	175.77	86.78
Method	N₃-Cr-N₅	N₄-Cr-N₆	N₃-Cr-N₂	C₁-C_{1,2}-C₂	C₄-C_{3,4}-C₃	C₅-C_{5,6}-C₆
B3LYP ^{a)}	92.28	90.35	176.87	114.98	114.76	115.47
B3LYP ^{b)}	92.06	90.84	176.47	115.03	114.45	115.59
CAS ^{b)}	92.44	91.00	175.99	114.88	114.58	115.53
Experiment	88.88	90.06	177.94	114.20	114.66	117.20

Table 6.1. Structural parameters of $[\text{Cr}(\text{tn})_3]^{3+}$ (bond lengths in Å and; angles between atoms in degrees).

^{a)} cc-pVTZ basis set used on all atoms

^{b)} SDD basis set used for Cr atom and 6-31g(d,p) for H, N and C atoms.

The structural parameters of only $[\text{Cr}(\text{tn})_3]^{3+}$ complex in these calculations together with CASSCF optimization results and their comparison with experimental studies of the crystal structure are presented in the table 6.1. The schematic representation of structural parameters present in the table 6.1 is shown on the figure 6.4.

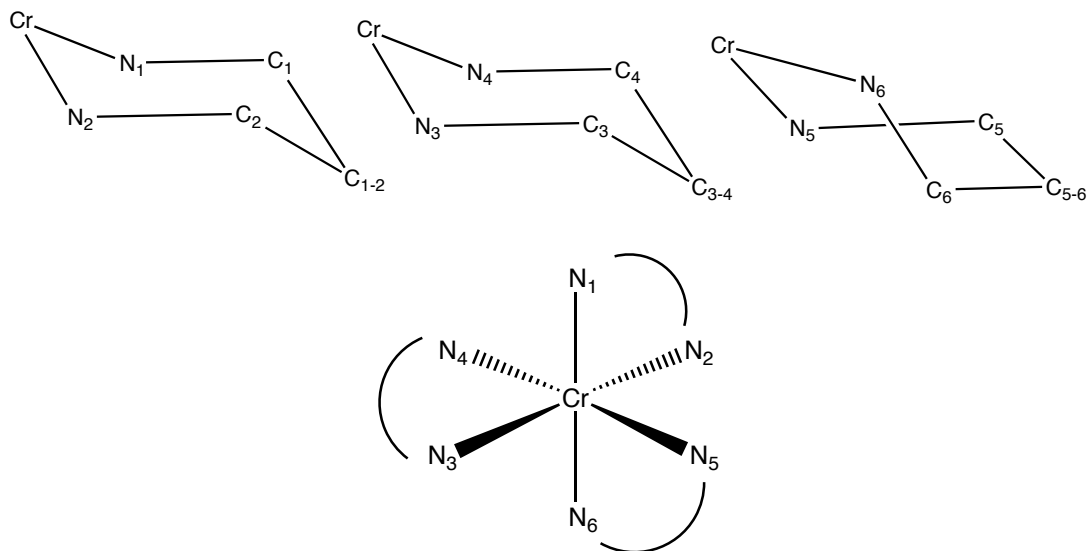


Figure 6.4. Pictorial representation of structural parameters in $[\text{Cr}(\text{tn})_3]^{3+}$.

TD-B3LYP was used to generate the spectral properties of the photoproducts of the aquation reaction of the main complex. 50 vertical states and a Gaussian broadening factor of 5 was taken into account while representing the UV-Vis spectrum of the system. An SDD basis set was chosen for Cr atom and 6-31g(p,d) for C, O, N and H atoms. For ligand field states presented in table 6.2 no Gaussian broadening was used.

To determine the character of the states the dominant component of the transition was chosen. Some of the states involved a large degree of state mixing, and so they were very hard to resolve. For those states natural transition orbitals were generated as was described in chapter 5. Table 6.2 presents the main photoproducts, their absorptions and the character of their absorptions. States higher than 330 nm are determined as of ligand field character and involve mainly the excitations within the t_{2g} and e_g set of orbitals (Figure 5.1 Chapter 5).

Complex	Wavelength/nm	Nature	Experiment ^{c)} /nm	Nature
[Cr(tn) ₃] ³⁺	420 ⁰	LF	457 351	LF LF
	345 ⁰	LF		
	250	LMCT		
<i>cis</i> -[Cr(tn) ₂ (H ₂ O) ₂] ³⁺	450 ^{vs}	LF	-	-
	360 ^{vs}	LF		
	335 ^{vs}	LF		
	265	LMCT		
<i>trans</i> - [Cr(tn) ₂ (H ₂ O) ₂] ³⁺	545 ⁰	LF	-	-
	491 ⁰	LF		
	432 ⁰	LF		
	386 ⁰	LF		
	320	LMCT		
	270	LMCT		
	205	LMCT		
<i>cis</i> - [Cr(tn) ₂ (tnH)(H ₂ O)] ⁴⁺	485 ^{vs}	LF	-	-
	435 ^{vs}	LF		
	345 ^{vs}	LF		
	270	LMCT		
	205	very mixed		
<i>trans</i> - [Cr(tn) ₂ (tnH)(H ₂ O)] ⁴⁺	512 ⁰	LF	-	-
	487 ⁰	LF		
	421 ⁰	LF		
	397 ⁰	LF		
	310	LMCT ^{a)}		
	265	LMCT ^{b)}		
	240	LMCT ^{b)}		
	205	LMCT ^{b)}		

Table 6.2. Spectral bands of main photoaquation products of [Cr(tn)₃]³⁺ complex: SDD basis set for Cr, 6-31g(p,d) basis set for C and O.

^{a)} small mixing with LF states

^{b)} mixing with IL states

^{c)} UV-Vis [12]

⁰ oscillator strength equal 0

^{vs} weak intensity state (oscillator strength between 0.0001-0.0007)

For octahedral systems that have inversion symmetry these states are electronically (Laporte) forbidden as described in the previous chapter. In cases where the system loses its symmetry, for example due to vibronic coupling induced phenomena (e.g. Jahn-Teller distortions), the Laporte rule is no longer valid and transitions within a single quantum shell become possible.

As mentioned before the studied complex has only “pseudo” O_h symmetry around the metal centre, however as a whole it does not possess any symmetry, thus no inversion centre. This could explain the presence of very weak LF transitions (oscillator strength in the range of 0.0001-0.0007) in the higher wavelength part of the spectrum in this system.

For the *trans*- isomer of $[\text{Cr}(\text{tn})_2(\text{H}_2\text{O})_2]^{3+}$ and both *cis*- and *trans*- isomers of the $[\text{Cr}(\text{tn})_2(\text{tnH})(\text{H}_2\text{O})]^{4+}$, the ligand field states calculated have an oscillator strength equal to 0 (not allowed states). The higher-energy (lower wavelength) bands of the spectrum involve mainly excitations of metal to ligand charge transfer character.

Studies on the photochemistry of $[\text{Cr}(\text{tn})_3]^{3+}$ and other photoproducts were performed using the multiconfigurational CASSCF method. An active space containing 9 electrons and 10 orbitals based on natural orbital occupations was chosen. The basis set used was the same as for TD-DFT, namely the SDD basis set on Cr atom and 6-31g(p,d) on C, O, N and H atoms. Conical intersection searches were performed in order to determine the relaxation pathways in the quartet and doublet manifolds of these systems.

6.1.2. Results and discussion.

The ground state minimum structure of $[\text{Cr}(\text{tn})_3]^{3+}$ and its photoproducts have a quartet spin state. A conical intersection search between the quartet ground state and the first quartet-excited state of $[\text{Cr}(\text{tn})_3]^{3+}$ was performed and a conical intersection seam located. The change in geometry of the system at the point of conical intersection involved a rupture of a single Cr-N bond that comes from tn ligand of twist boat conformation and the metal centre adopts a trigonal pyramidal geometry (TBP). Ground state optimizations on that structure using the B3LYP functional were performed. Two stable minima with a square pyramidal geometry at the metal centre were found, both

with a coordination hole at the axial position at the metal centre and one tn ligand „hanging” loose (Figure 6.5). If water is present in the reaction mixture it can favourably coordinate to the metal on the ground state PES. This leads to the formation of both *cis*- and *trans*- isomers of $[\text{Cr}(\text{tn})_2(\text{tnH})(\text{H}_2\text{O})]^{4+}$. Indeed its presence has been seen in experimental studies as one of the products of the photo-induced aquation reaction of $[\text{Cr}(\text{tn})_3]^{3+}$ [12, 14].

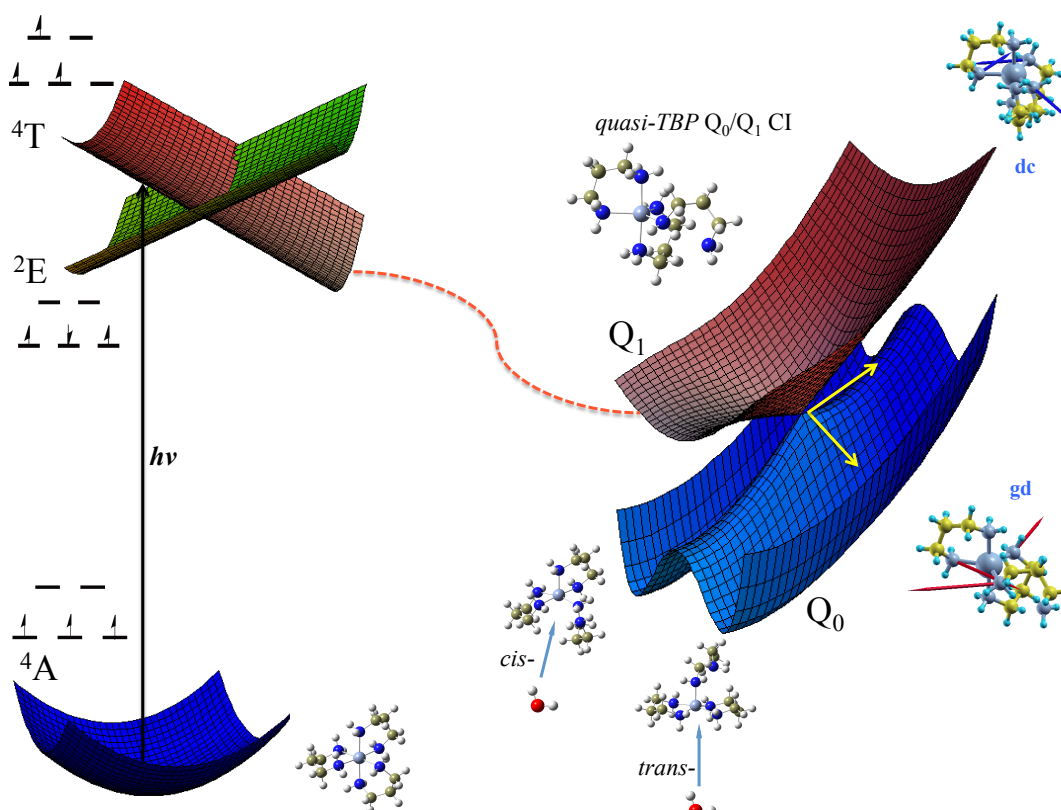


Figure 6.5. $[\text{Cr}(\text{tn})_3]^{3+}$ structures on different PESs and schematic representation of the possible aquation mechanism of this system (gd – gradient difference vector, dc – derivative coupling vector).

The presence of both stereoisomers of the $[\text{Cr}(\text{tn})_2(\text{tnH})(\text{H}_2\text{O})]^{4+}$ can be explained in a similar way as the photostereochemistry of the 5-coordinate chromium fragments described by Vanquickenborne in the case of other Cr (III) amine systems [2]. Figure 6.6 presents the schematic picture of the possible isomerisation from trigonal bipyramidal (TBP) to square pyramidal (SP) coordination of the ligands around the metal centre. Structure 1 on figure 6.6 represents the structure of $[\text{Cr}(\text{tn})_3]^{3+}$ at the point of conical intersection with a TBP geometry at the metal centre. The equatorial plane contains two nitrogen atoms coming from tn ligands of chair conformation still fully

coordinated to the metal, and a nitrogen atom from one end of the dissociated tn ligand. As described in the reference [2] the TBP structure is JT active geometry that could be accessed by rearrangement of the ligands in the equatorial plane.

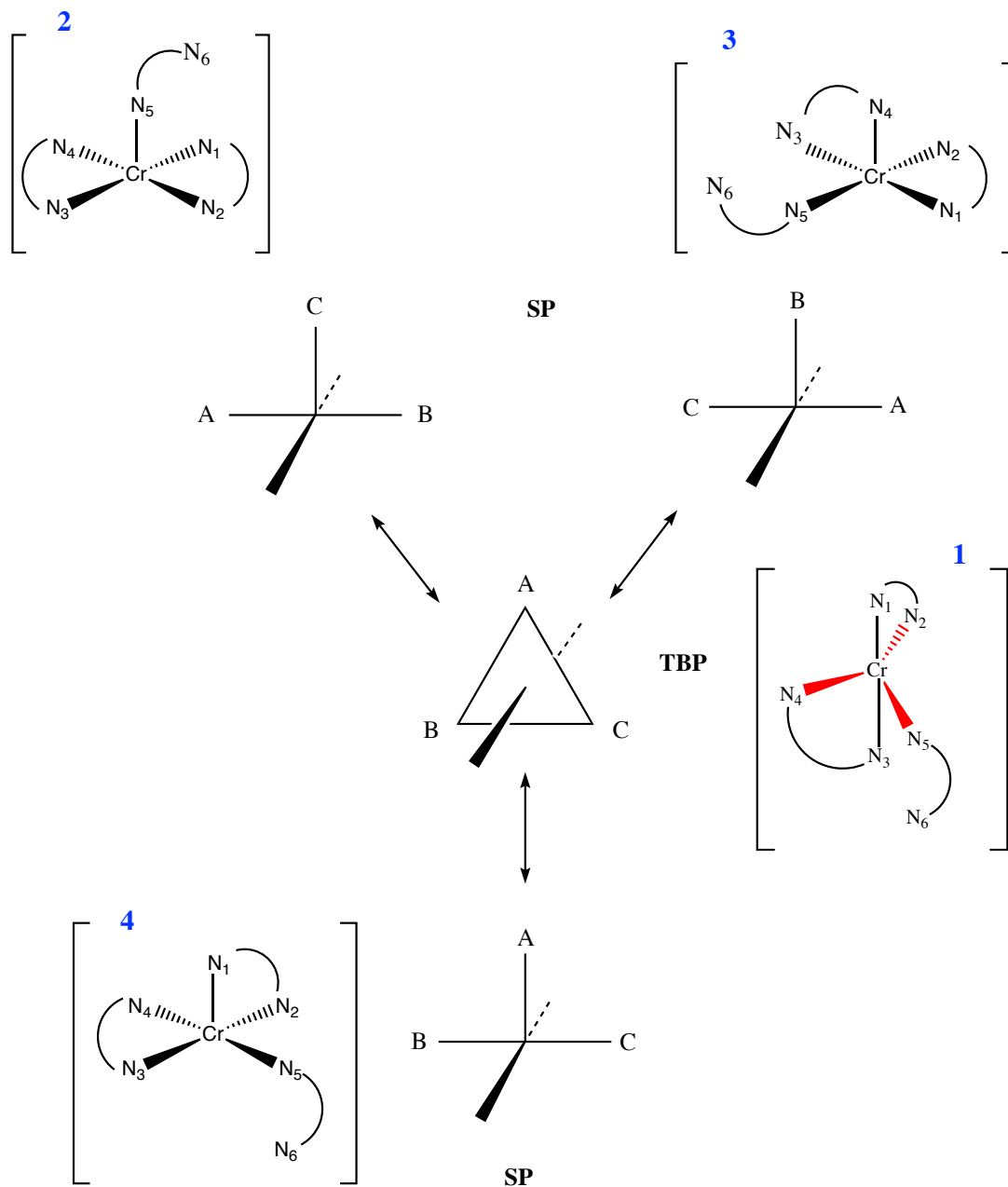


Figure 6.6. Isomerisation pathways of the trigonal-bipyramidal (TBP) fragment to form square planar structure. Red bonds represents the equatorial plane of the TBP system (adapted from the reference [2]).

The equatorial bending modes that are present at the conical intersection point of $[\text{Cr}(\text{tn})_3]^{3+}$ (look at the derivative coupling and gradient difference vectors in figure 6.5) could cause the isomerisation to SP coordination at the metal centre. Structure 2 is

formed by the equatorial bending mode of the N_4CrN_2 angle. Structures 3 and 4 are equivalent and formed due to the equatorial bending vibration of N_5CrN_2 or N_4CrN_5 angles. The ground state minima in the presence of solvent can trap the water molecules, structure 2 in the *trans* position to the part end dissociated tn ligand and structures 3 and 4 in the *cis* position to one-end dissociated tn ligand. This would explain the presence of both *cis* and *trans* isomers of the $[Cr(tn)_2tnH(H_2O)]^{4+}$ complex.

Summing up, the formation of the $[Cr(tn)_2tnH(H_2O)]^{4+}$ photoproduct occurs by the excited state pathway shown in figure 6.5. $[Cr(tn)_3]^{3+}$, after excitation to the quartet excited state, has access to a very efficient conical intersection to the ground state PES. The molecule at the point of conical intersection has TBP coordination around the Cr atom which is similar to the TBP Jahn-Teller active structure common for Cr (III) complexes, leading to the formation of SP isomers on the ground state PES (Figure 6.6.). A water molecule coordinates to the Cr atom on the ground state PES leading to a formation of *cis* and *trans* isomers of $[Cr(tn)_2tnH(H_2O)]^{4+}$.

According to experiment the photoactive doublet state can participate in the photochemistry of this system and quench the photoreaction. The intersystem crossing between the quartet ground state and lowest doublet excited state was not located computationally, however this does not preclude its presence. The intersystem crossing between the first quartet excited state and lower lying doublet state however, was found. This gives an alternative pathway for relaxation of this system. Due to the presence of an alternative pathway through the doublet excited states, the aquation reaction through the quartet excited state could be quenched. Further studies on the deactivation pathways through the doublet states may be required.

Similar studies were performed on the photoproducts of the photoaquation reaction of $[Cr(tn)_3]^{3+}$. Looking at the possible relaxation pathways on the quartet manifolds of *cis*- $[Cr(tn)_2tnH(H_2O)]^{4+}$ another conical intersection was located connecting the quartet ground state with the first quartet excited state. The characteristic feature of the structure at the conical intersection point for this system is the same as for the previous complex, a rupture of a Cr-N bond of one of the tn ligands, this time of chair conformation. The structure at the conical intersection point ($[Cr(tn)(tnH)_2(OH)]^{3+}$) is shown in figure 6.7. The chromium centre again adopts a TBP structure that can distort

possibly via the JT active surface (as described above) to form a SP symmetry at the metal centre.

As described at the beginning of this section the other photoproduct observed in the aquation reaction mixture of $[\text{Cr}(\text{tn})_3]^{3+}$ is the $[\text{Cr}(\text{tn})(\text{tnH})_2(\text{H}_2\text{O})_2]^{5+}$ system. This system would be formed through the relaxed structure of SP $[\text{Cr}(\text{tn})(\text{tnH})_2(\text{OH})]^{3+}$, on the ground state PES by coordination of water molecules to the coordination hole on the metal centre of the SP isomers of $[\text{Cr}(\text{tn})(\text{tnH})_2(\text{OH})]^{3+}$.

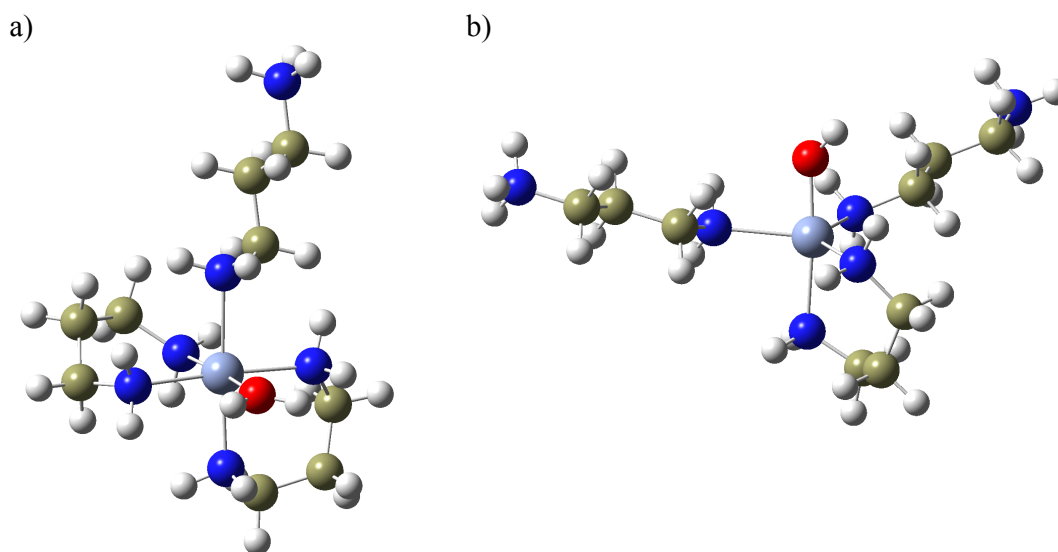


Figure 6.7. Structure of $\text{cis-}[\text{Cr}(\text{tn})_2\text{tnH}(\text{H}_2\text{O})]^{3+}$ at the point of a) the ground state minimum, b) conical intersection.

The same photoreaction in the quartet manifold of trans- isomer of $[\text{Cr}(\text{tn})_2\text{tnH}(\text{H}_2\text{O})]^{3+}$ was determined. The system at the conical intersection point adopts again a TBP geometry at the metal centre (Figure 6.7). The energy difference between the ground state minimum and the point of conical intersection is equal to around 2kcal/mole, which suggests that the conical intersection would be very accessible and population of the ground state would be very efficient. The outcome of this reaction is the $[\text{Cr}(\text{tn})(\text{tnH})_2(\text{H}_2\text{O})_2]^{5+}$ photoproduct.

Cis- and *trans-* isomers of another experimentally observed product meaning $[\text{Cr}(\text{tn})_2(\text{H}_2\text{O})_2]^{3+}$ was then examined. $\text{Cis-}[\text{Cr}(\text{tn})_2(\text{H}_2\text{O})_2]^{3+}$ when irradiated to the quartet excited state can access a point where both the quartet ground and lowest quartet

excited state PESs cross. At the point of this crossing the system seems to dissociate a water ligand. After relaxing to the ground state PES the system adopts again a SP geometry with the coordination hole at the metal centre. The water molecule dissociated from the *cis*- position could then through the mechanism described before re-coordinate to a *cis*- or *trans*- position and form the initial system *cis*-[Cr(tn)₂(H₂O)₂]³⁺ or the *trans*-[Cr(tn)₂(H₂O)₂]³⁺ isomer.

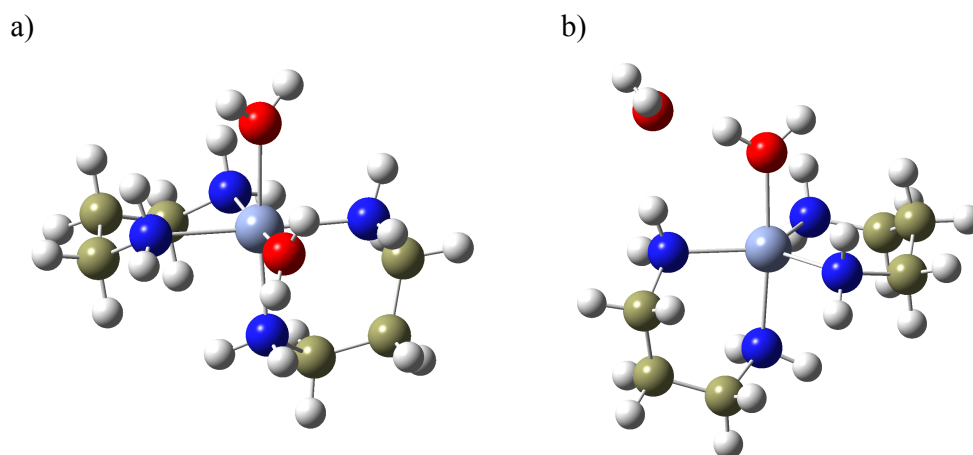


Figure 6.8. Structure of *cis*-[Cr(tn)₂(H₂O)₂]³⁺ at the point of a) ground state minimum, b) conical intersection.

Examining further the photoreaction on the side of *trans*-[Cr(tn)₂(H₂O)₂]³⁺, the sloped conical intersection in the quartet manifold of the reaction (angle between gradients of two states 40 deg.) has been located. The Cr-N bond from a tn ligand is ruptured, and there is a hydrogen transfer from one of the water molecule to one part dissociated tn ligand (Figure 6.9).

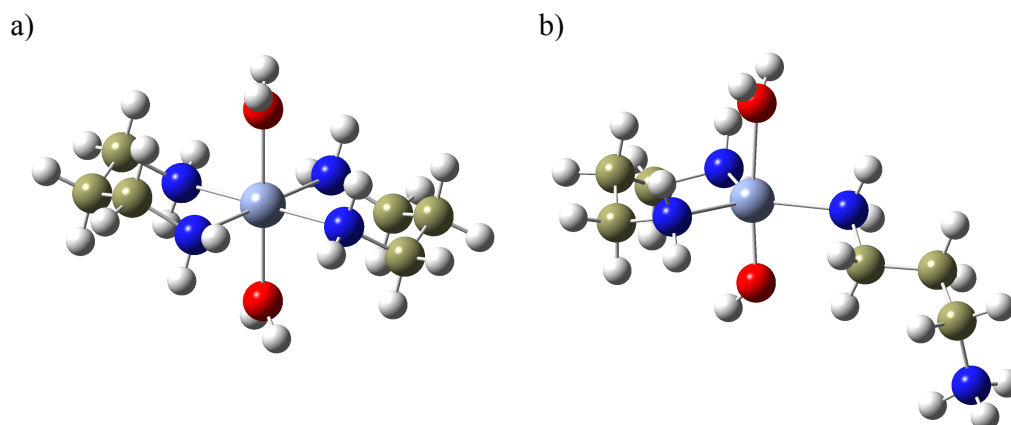


Figure 6.9. Structure of *trans*-[Cr(tn)₂(H₂O)₂]³⁺ at the point of a) ground state minimum, b) conical intersection.

Following the same scheme of reaction as for the previous system, this route would suggest formation of $[\text{Cr}(\text{tn})(\text{tnH})(\text{H}_2\text{O})_3]^{3+}$. This system was not observed experimentally, however, its presence cannot be ruled out and it may be formed in a reaction on a longer time-scale.

Summing up, the photoaquation reaction of $[\text{Cr}(\text{tn})_3]^{3+}$ and its photoproducts is a multi step process. Formation of the first photoproducts such as *cis*- and *trans*- $[\text{Cr}(\text{tn})_2(\text{tnH})(\text{H}_2\text{O})]^{4+}$ and their irradiation to light leads to successive photolysis and formation of the other photoproducts described above. The common feature of all the studied systems is the distortion of the O_h coordination at the Cr (III) centre to a TBP geometry, at the point of surface crossing between the quartet ground and first excited state. Due to the JT accessible excitation plane at the point of conical intersection all the studied systems could isomerise to form an SP geometry at the metal centre. The systems then relaxed and ended up on the ground state PES with coordination holes around the metal, which are filled by the trapping of a water molecule from the solvent.

6.2. Photochemistry and photoaquation of *trans*- $[\text{Cr}(\text{tn})_2(\text{CN})_2]^+$.

Kirk and co-workers reported the photoaquation of *trans*- $[\text{Cr}(\text{tn})_2(\text{CN})_2]^+$ [13]. The UV/Vis spectrum was measured in a weak solution of HClO_4 and is dominated by ligand field states, the position of the peaks of this complex is comparable with other $[\text{Cr}(\text{L})_x(\text{CN})_2]^{3+}$ systems, where L belongs to the group of amine ligands such as en (1,2-diaminoethane) or ammonia. The rate of CN aquation increased with the concentration of acid. From their experimental studies they have assigned the following photoproducts of this reaction: *trans*- $[\text{Cr}(\text{tn})(\text{tnH})\text{H}_2\text{O}(\text{CN})_2]^{2+}$, *cis*- $[\text{Cr}(\text{tn})(\text{tnH})\text{H}_2\text{O}(\text{CN})_2]^{2+}$, *cis*- $[\text{Cr}(\text{tn})_2(\text{H}_2\text{O})(\text{CN})]^{2+}$, *trans*- $[\text{Cr}(\text{tn})_2(\text{CN})_2]^+$ and *cis*- $[\text{Cr}(\text{tn})_2(\text{H}_2\text{O})(\text{CN})]^{2+}$ (thermal product). Similar studies as for $[\text{Cr}(\text{tn})_3]^{3+}$ were performed on *trans*- $[\text{Cr}(\text{tn})_2(\text{CN})_2]^+$ and its aquation photoproducts.

An interesting observation they made was that the doublet lifetime is very long and 75% of the reaction goes via the doublet state and also the doublet excited state of the starting *trans*- $[\text{Cr}(\text{tn})_2(\text{CN})_2]^+$ system is quenched by the thermo- and photoproducts. The authors stated that it was the first such observation ever made in the photochemistry

of inorganic systems that the photoproducts can quench the photoreaction. The following section of this chapter will present a study on this particular photoreaction using the same computational methodologies as above.

6.2.1. Computational details.

TD-DFT studies on the starting complex using a cc-pVTZ basis set were performed to determine the positions of spectroscopic transitions and their nature. 50 vertical states were chosen to obtain the spectrum. The comparison of the performance of different functionals is presented in table 6.3.

B3LYP	Nature	B3LYP ^{a)}	Nature	CAM-B3LYP	Nature	CAM-B3LYP ^{a)}	Nature
445 ⁰	LF	436 ⁰	LF	451 ⁰	LF	442 ⁰	LF
423 ⁰	LF	403 ⁰	LF	421 ⁰	LF	404 ⁰	LF
350 ⁰	LF	344 ⁰	LF	345 ⁰	LF	342 ⁰	LF
305 ⁰	LF	313 ⁰	LF	302 ⁰	LF	312 ⁰	LF
255	LMCT	230	LMCT	235	LMCT	225 ^{sh}	LMCT
230	LMCT	210	LMCT	205	LMCT	205	LMCT
215	LMCT						
BP86	Nature	BP86 ^{a)}	Nature	WB97XD ^{a)}	Nature	WB97XD ^{a)}	Nature
413 ⁰	LF	402 ⁰	LF				
367 ⁰	LF	384 ⁰	LF	444 ⁰	LF	436 ⁰	LF
350 ⁰	LF	340 ⁰	LF	451 ⁰	LF	340 ⁰	LF
323 ⁰	LF	318 ⁰	LF	343 ⁰	LF	312 ⁰	LF
315	LMCT	310	LMCT	303 ⁰	LF	220	LMCT
270	LMCT	290	LMCT	230	LMCT	200	LMCT
245	LMCT	265	LMCT	200	LMCT		
		240	LMCT				

Table 6.3. Comparison of the electronic transitions of the main spectral band in the wavelength range of 150-500 nm using different functionals of *trans*-[Cr(tn)₂(CN)₂]⁺. Calculations performed using cc-pVTZ basis set on all atoms. The Gaussian broadening factor is equal to 5 for LMCT states, and no broadening for LF states.

^{a)} PCM model, with water as a solvent

^{sh} shoulder band

⁰ oscillator strength 0.

There was not much difference in the positions of the electronic transition between B3LYP, CAM-B3LYP and WB97XD functionals in the gas phase. Only the position of

the bands for the functional that does not contain any Hartree-Fock exchange namely the BP86 functional are blue shifted around 30-40 nm.

The electronic transitions for $trans-[Cr(tn)_2(CN)_2]^+$ with 0 oscillator strength are of ligand field character. The only UV visible bands come from ligand to metal charge transfer excitations (Table 6.3). Experimental data show ligand field absorptions at 344 nm and 441 nm for $trans-[Cr(tn)_2(CN)_2]^+$ complex (Table 6.4). The calculated spectral absorptions of $trans-[Cr(tn)_2(CN)_2]^+$ and photoproducts of its aquation reaction are presented in table 6.4. The calculated locations of LF excitations for $trans-[Cr(tn)_2(CN)_2]^+$ are comparable with experimental results.

System	B3LYP	Nature ^{d)}	Experiment[13]	Nature
$trans-[Cr(tn)_2(CN)_2]^+$	445 ⁰	LF	441 344	LF LF
	423 ⁰	LF		
	350 ⁰	LF		
	305 ⁰	LF		
$trans-[Cr(tn)(tnH)(H_2O)(CN)_2]^{2+}$	495 ^{a)}	LF	-	-
	465 ^{a)}	LF		
	450 ^{a)}	LF		
	375 ^{a)}	LF		
$cis-[Cr(tn)(tnH)(H_2O)(CN)_2]^{2+}$	450 ^{b)}	LF	-	-
	415 ^{b)}	LF		
	375 ^{b)}	LF		
$cis-[Cr(tn)_2(H_2O)(CN)]^{2+}$	485 ^{c)}	LF	-	-
	465 ^{c)}	LF		
	390 ^{c)}	LF		
	340 ^{c)}	LF		

Table 6.4. Spectral properties of $trans-[Cr(tn)_2(CN)_2]^+$ and its aquation reaction photoproducts in the range of 300 – 500 nm.

^{a)} weak intensity in the range between 0.0001 - 0.0003

^{b)} weak intensity in the range between 0.0001 – 0.0002

^{c)} weak intensity in the range between 0.00001 – 0.0004

^{d)} all the given transitions include also some ligand to ligand character

⁰ oscillator strength 0.

To determine the nature of the occurring photochemistry the same type of CASSCF calculations as for the $[Cr(tn)_3]^{3+}$ system described in the previous section, on all the photoproducts of photoaquation reaction of $trans-[Cr(tn)_2(CN)_2]^+$ system, in the quartet and doublet manifold were performed. An active space of 9 electrons and 10 orbitals

was chosen. Orbitals were based on natural orbital occupations initially generated using the UHF method with an SDD basis set on the Cr atom and 6-31g(d,p) basis on other atoms.

6.2.2. Results and discussion.

There was no direct relaxation pathway in the quartet manifold of the *trans*-[Cr(tn)₂(CN)₂]⁺ starting complex or the *trans*-[Cr(tn)(tnH)(H₂O)(CN)₂]²⁺ photoproduct, determined by computational studies.

Studies in the doublet manifold of *trans*-[Cr(tn)₂(CN)₂]⁺ show an accessible ISC between the first quartet excited state and lower doublet state that occurs with little geometrical change of the molecule. The system then can relax in the doublet manifold and from the lowest lying doublet excited state undergoes another ISC with the quartet ground state. The structure of *trans*-[Cr(tn)₂(CN)₂]⁺ at the point of the ⁴A_{2g}/²E ISC adopts a 7-coordinate intermediate as shown in figure 6.10 b, and from there relaxes to the quartet ground state. On the ground state PES it can adopt either the *cis*-[Cr(tn)₂(CN)(NC)]⁺ structure (Figure 6.10 c)) or the structure of the *cis*-[Cr(tn)₂(CN)₂]⁺ isomer (Figure 6.10 d)). There is a minimum on the ground state of the *cis*-[Cr(tn)₂(CN)₂]⁺ isomer where one of the tn ligands adopts a twist boat conformation, and the other one, a chair conformation. As shown in the previous section for [Cr(tn)₃]³⁺, a tn ligand with a twist boat conformation coordinated to the metal centre is very susceptible under the influence of light to cleavage of one of its metal M-N bonds. This would lead to water trapping at the coordination hole on the metal hole, through the same mechanism as for [Cr(tn)₃]³⁺. This mechanism would explain the presence of *cis*-[Cr(tn)(tnH)(H₂O)(CN)₂]²⁺ in the reaction mixture of aquation reaction of *trans*-[Cr(tn)₂(CN)₂]⁺ complex.

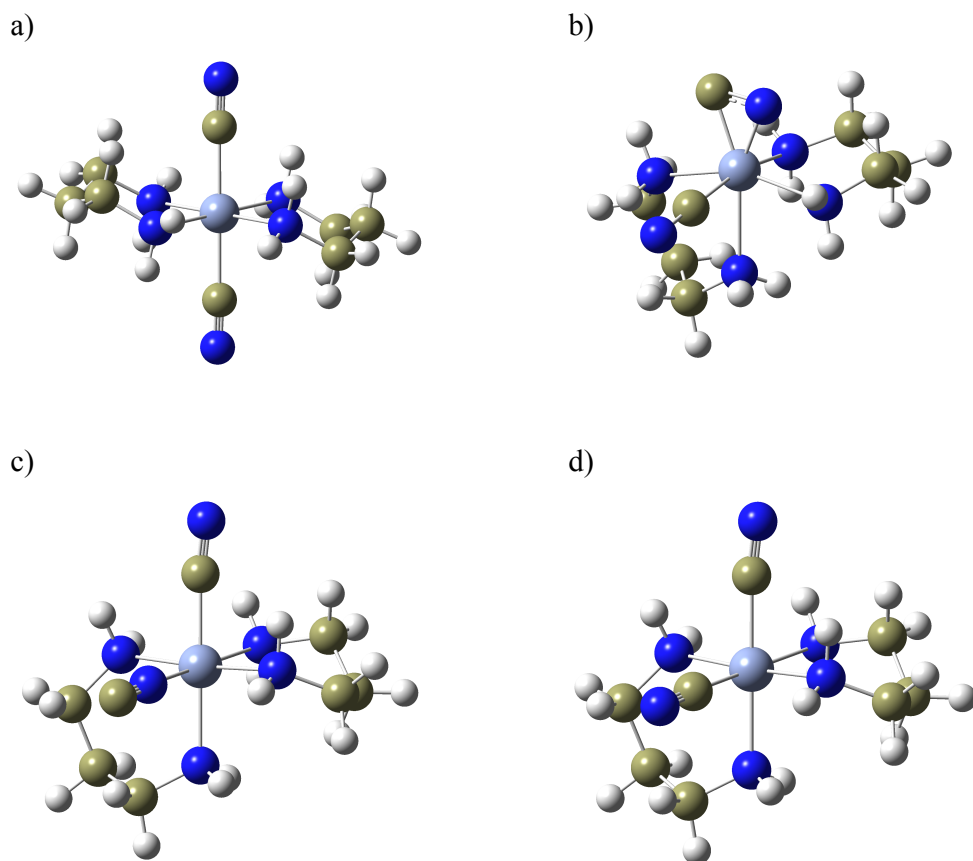


Figure 6.10. Structure of $trans\text{-}[\text{Cr}(\text{tn})_2(\text{CN})_2]^+$ at the point of a) ground state minimum, b) intersystem crossing intermediate, c) ground state structure of $cis\text{-}[\text{Cr}(\text{tn})_2(\text{CN})(\text{NC})]^+$ d) ground state structure of $cis\text{-}[\text{Cr}(\text{tn})_2(\text{CN})_2]^+$

The same studies on the quartet manifold of $cis\text{-}[\text{Cr}(\text{tn})(\text{tnH})(\text{H}_2\text{O})(\text{CN})_2]^{2+}$ show a tendency of the system to remove a tnH ligand from the metal centre, however such photoproduct, with only one tn ligand coordinated to the metal centre, has not been observed experimentally. This process may occur on a long time-scale.

Another photoproduct experimentally observed is $cis\text{-}[\text{Cr}(\text{tn})_2(\text{H}_2\text{O})(\text{CN})]^{2+}$. We have been not able to find any excited intermediate with a dissociated CN ligand. Further studies on the excited state relaxation pathways are required. This also may be a ground state reaction on a longer time-scale.

Studies in the quartet manifold of the $cis\text{-}[\text{Cr}(\text{tn})_2(\text{H}_2\text{O})(\text{CN})]^{2+}$ complex show the conical intersection connecting the quartet ground state with first excited quartet state. The O_h chromium centre at the point of conical intersection is being distorted to TBP (Figure 6.11), the same feature that appears for $[\text{Cr}(\text{tn})_3]^{3+}$. This feature is similar to

$[\text{Cr}(\text{C}_2\text{O}_4)_3]^{3-}$ and appears to be a ubiquitous feature of Cr (III) photostereochemistry. Another characteristic feature of this complex at the point of conical intersection is that the water molecule is removed from the coordination site of the metal.

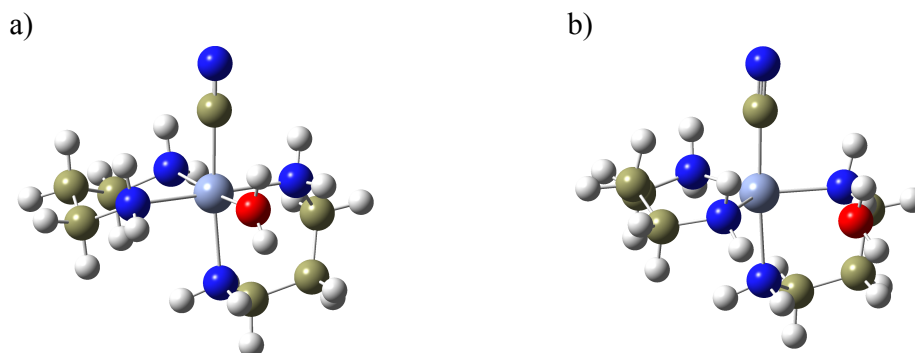


Figure 6.11. Structure of $\text{cis-}[\text{Cr}(\text{tn})_2(\text{H}_2\text{O})(\text{CN})]^{2+}$ at the point of a) ground state minimum, b) conical intersection.

Due to the TBP Jahn-Teller active geometry at the point of conical intersection, a feature, which is also common for other Cr (III) systems, described in this and previous chapter, the system distorts to the ground state PES adopting SP geometry at the metal centre. If there are any free ligands present in the reaction mixture (e.g. water in the case of studied reaction) the system reforms itself by trapping this ligand at the coordination hole on the Cr atom.

Further studies on the relaxation pathways through the doublet excited states are required to better understand the reactive excited states of the photoaquation process occurring in these systems.

6.3. List of references.

- [1] Kirk, A. D.; Ibrahim, A. M., Wavelength Dependence of Unquenchable Photoaquation in the Tris(1,3-Diaminopropane) Chromium (III) Ion. *Inorg. Chem.* **1990**, 29, 4848-4850.
- [2] Vanquickenborne, L. G.; Coussens, B.; Postelmans, D.; Ceulemans, A.; Pierloot, K., Photochemistry of Chromium (III) Ammine Compounds - an *Ab-initio* Study. *Inorg. Chem.* **1992**, 31, 539-547.
- [3] Kirk, A. D., Photochemistry and Photophysics of Chromium (III) Complexes. *Chem. Rev.* **1999**, 99, 1607-1640.
- [4] Kirk, A. D.; Irwin, G., Intermediates in Chromium (III) Photochemistry. *Coord. Chem. Rev.* **2001**, 211, 25-43.
- [5] Kane-Maguire, N. A. P., Photochemistry and Photophysics of Coordination Compounds: Chromium. *Top. Curr. Chem.* **2007**, 280, 37-67.
- [6] Cimolino, M. C.; Linck, R. G., Stereochemistry of the Photoaquation of Optically-Active Tris(Ethylenediamine) Chromium (III) as a Probe of Excited-State Pathway. *Inorg. Chem.* **1981**, 20, 3499-3503.
- [7] Kirk, A. D.; Ibrahim, A. M., Relative Labilities of 1,3-Diaminopropane and Ammonia Ligands in Photoaquation of $[\text{Cr}(\text{tn})_x(\text{NH}_3)_{6-2x}]^{3+}$ Complexes. *Inorg. Chem.* **1988**, 27, 4567-4574.
- [8] Kirk, A. D.; Frederick, L. A.; Glover, S. G., Differential Quenching of Chromium (III) Photochemistry. *J. Am. Chem. Soc.* **1980**, 102, 7120-7122.
- [9] Kane-Maguire, N. A. P.; Wallace, K. C.; Miller, D. B., Synthesis, Characterization, and Photobehavior of *Cis*-Diammine and *Trans*-Diammine(1,4,8,11-Tetraazacyclotetradecane) Chromium (III) and Some Related-Compounds. *Inorg. Chem.* **1985**, 24, 597-605.
- [10] Wong, C. F. C.; Kirk, A. D., Synthesis and Spectral Properties of $[\text{Cr}(\text{en})_2\text{NH}_2\text{X}]^{2+}$ Compounds. *Can. J. Chem.* **1975**, 53, 3388-3393.
- [11] Jurnak, F. A.; Raymond, K. N., Effect of Packing Forces on Geometry of $[\text{Ni}(\text{CN})_5]^{3-}$ Ion - Structures of $[\text{Cr}(\text{NH}_2\text{CH}_2\text{CH}_2\text{CH}_2\text{NH}_2)_3][\text{Ni}(\text{CN})_5] \cdot 2\text{H}_2\text{O}$ and $[\text{Cr}(\text{NH}_3)_6][\text{Ni}(\text{CN})_5] \cdot 2\text{H}_2\text{O}$ - Skew-Boat Conformation in a 6-Membered Metal Chelate Ring. *Inorg. Chem.* **1974**, 13, 2387-2397.

- [12] Gowin, E.; Wasgestian, F., Joint Bond Breaking in the Photolysis of the Tris(1,3-Diaminopropane) Chromium (III) Ion. *Inorg. Chem.* **1985**, *24*, 3106-3110.
- [13] Kirk, A. D.; Fernando, S. R. L., Thermoquation and Photoquation of *Trans*-[Cr(1,3-Diaminopropane)₂(CN)₂](ClO₄)⁻ Quenching of Photochemistry by Photoproducts. *Inorg. Chem.* **1992**, *31*, 656-661.
- [14] Kirk, A. D.; Fernando, S. R. L., Synthesis and Photoproperties of a Quencher, Na[Cr(1,3-Diaminopropane)(CN)₄], and Reinvestigation of [Cr(1,3-Diaminopropane)₃]³⁺ Photoproduct Quenching. *Inorg. Chem.* **1994**, *33*, 4435-4438.
- [15] Peterson, K. A. Peterson Research Group: Correlation Consistent Basis Sets. <http://tyr0.chem.wsu.edu/~kipeters/basis.html>

CHAPTER 7

Conclusions

This thesis presented computational studies on the understanding of the photo-induced stereochemistry and spectroscopy of five different inorganic systems, one of them being the ammonia molecule, and the remaining four large closed and open-shell transition metal complexes. A quantum chemical excited-state treatment is crucial in determining and rationalising photo-triggered experimental observations because only a theoretical study can accurately probe the coupled potential energy surfaces responsible for the photochemistry. Different methods of excited-state quantum chemistry have been used in this thesis, and a summary of their performance is discussed below.

Chapter 3 presented a study on the pseudo-Jahn Teller effect in the ammonia molecule and the edge-sharing bioctahedral $\text{Mo}_2(\text{DXylF})_2(\text{O}_2\text{CCH}_3)_2(\mu_2\text{-O})_2$ complex. Due to this effect, i.e., the vibronic coupling between potential energy surfaces, which in these two systems is a coupling between the ground and the first excited state, the curvature of the ground state potential energy surface is changed and the energy and symmetry of the molecule is lowered. Bearpark and co-workers presented a way to prove if the pseudo-Jahn-Teller effect indeed influences the structure of a given system. Their test is based on analytical Hessians using the multiconfigurational CASSCF method, and was successfully applied in this chapter, proving that the pseudo-Jahn-Teller effect is responsible for the distorted lower symmetry structure of both studied systems. Ammonia adopts a lower energy pyramidal C_{3v} ground state structure rather than a higher symmetry D_{3h} structure due to coupling between the ground electronic state and second excited state via a non-totally symmetric out-of-plane vibration. Due to the very high cost of CASSCF calculations in the case of the large transition bimetal complex $\text{Mo}_2(\text{DXylF})_2(\text{O}_2\text{CCH}_3)_2(\mu_2\text{-O})_2$, a model system had to be built for further CASSCF studies. Spectroscopic investigations on both the model and the full complex verified the reliability of the model system. The CASSCF symmetry-constrained Hessian method demonstrated that the central motif $\text{Mo}_2(\mu_2\text{-O})_2$ of this system has a rhomboidal shape and C_{2h} symmetry instead of the highest possible D_{2h} symmetry, which is caused by pseudo-Jahn-Teller coupling between the ground state with a spectroscopically dark $\pi\delta^*$ state. This work conclusively demonstrates that the origin of the surprising experimental observation is due to vibronic coupling.

Chapter 4 presented a computational investigation on a recent experimental observation of the *meridial* to *facial* photo-isomerisation of the platinum-bis(8-quinolinyl)amido pincer complex, (BQA)PtMe₂I. The system was stable in the dark but under the influence of light it isomerised to adopt the *facial* structure of the complex. The mechanism of this reaction was not known, thus computational studies in order to determine this mechanism were performed. Time-dependent (TD)-DFT response theory has been used to assign the nature of the main spectroscopic bands of the system. The character of these bands involves essentially intra-ligand π to π^* type excitations, and not ligand to metal charge transfer (LMCT) states as postulated in experimental studies. These excitations involve also a reduction in the conjugation across the planar amido linkage in the BQA ligand. The CASSCF method has been applied in order to study possible excited state relaxation pathways. The molecule is initially excited to a $\pi\pi^*$ state and relaxes with the ligand sphere undergoing rearrangement towards *facial*-like BQA conformations, which leads to an excited *facial* minimum. From there it accesses a conical intersection that connects the S₁ state to the ground state forming the *facial* isomer of the complex. An interesting observation is that the metal does not seem to take a major role in the photochemistry occurring. Constrained conical intersection searches on the pure BQA ligand were performed and the intersection seam was found for a structure of very similar geometry to the full complex. The branching space vectors involve motion of the amido-link in the BQA ligand. Thus, when the locally excited ligand is driven towards such folded geometries, the crossing to the ground state becomes favourable regardless of the presence of metal. This also explains why there is no back conversion to the *meridial* structure as the intersection is sloped and the photoexcited form is only connected with ground state *facial*-like structures.

Chapter 5 looked at the photochemistry of the open-shell Chromium oxalate [Cr(C₂O₄)₃]³⁻ system that is important due to its energy migration features that are similar to ruby. The infrared and UV-vis spectroscopy was examined using DFT and its TD extension respectively. The calculated infrared spectra are in good agreement with the experimental ones. This showed that DFT can be a very good, cost efficient alternative for examination of ground state properties of large transition metal complexes, also of open-shell character, and can play a role in the assignment of the IR spectra in such systems. The performance of the TD-DFT method for the UV-vis spectroscopy of open-shell transition metal systems is very poor in comparison to

closed-shell systems, due to significant spin contamination. The character of the main spectroscopic bands could not be definitively resolved due to a large degree of state mixing. Another drawback is that standard TD-DFT fails to describe spin-flip transitions, which can be of great importance for open-shell systems. Mechanisms for radiationless deactivation through the quartet and doublet manifolds were examined using the multiconfigurational CASSCF method. A conical intersection between the 4A_2 ground state and one component of the 4T excited state was located, involving a rupture of one of the Cr-O bonds and its rearrangement to an unsaturated intermediate. The coordination of the metal centre at the conical intersection point becomes trigonal bipyramidal (TBP), which is Jahn-Teller active and from there the system distorts to a minimum on the PES. Due to the peaked character of this conical intersection, the system relaxes either to the initial isomer or adopts the form of its optical isomer. This mechanism explains the experimentally observed photoinduced character of the racemisation reaction of this system. Intersystem crossing between the 2E and 4T states have been located that did not involve any major change in geometrical parameters of the system. This gives a possible pathway for energy emission from the excited 2E to the ground state 4A_2 seen experimentally.

Chapter 6 presented a study on the photoaquation reaction of chromium (III) tris(1,3-diaminopropane) $[Cr(tn)_3]^{3+}$ and its derivative $trans-[Cr(tn)_2(CN)_2]^+$ complex. The presence of the aquated photoproducts of $[Cr(tn)_3]^{3+}$ can be explained by the accessible conical intersection on the quartet manifold of the reaction involving the rupture of one of the Cr-N bonds coming from the tn ligand at a twist boat conformation. At the point of conical intersection the system adopts a Jahn-Teller like structure with TBP geometry at the unsaturated metal centre, similar to $[Cr(C_2O_4)_3]^{3-}$. From there it rearranges to form square pyramidal isomers with a coordination hole at the axial position of the chromium atom and relaxes to the ground state where it favourably traps a water molecule in the coordination hole. The photoproducts formed, *cis*- and *trans*- stereoisomers of $[Cr(tn)_2(tnH)(H_2O)]^{4+}$, under irradiation of light undergo similar reactions in the quartet manifolds and cause formation of other photoproducts. The reaction can be quenched through the alternative pathway involving an intersystem crossing from the quartet to the doublet state. This explains the experimental observations of the presence of the given photoproducts in the final reaction mixture.

The above highlights show how recently available computational methodologies can be used to describe and possibly explain experimental observations in the photochemistry of complex inorganic systems. The main difficulties encountered here were connected mainly with the size of the systems studied, for which accurate calculation can get very expensive. The presence of metal electrons/orbitals results in a greater density of low-lying electronic states compared to organic systems. These can be challenging to model and treat computationally due for example to state crossing and mixing induced by vibronic coupling, for example. Methodologies that are required to treat these problems need significant computer resources. CASSCF has been a very successful method for the qualitative treatment of a range of vibronic coupling effects such as conical intersections or the pseudo-Jahn-Teller effect, for both closed and open-shell metal systems. Its limitation is mainly the size of an active space, which for larger systems such as transition metal complexes may need to be larger than organic ones, thus increasing the cost of the calculation. The choice of a smaller active spaces for such systems, if the orbitals are chosen incorrectly, or more orbitals are needed to properly describe the occurring photochemistry, may sometimes lead to an unbalanced wavefunction. Using Configurations State Functions (CSFs) versus Slater Determinants (SD) to describe different spin states is another factor that must be considered. Because CSFs that build the CASSCF wavefunction are correct spin eigenfunctions this method is very good in describing both closed and open-shell systems and follows interactions between states of different multiplicities. Using appropriate chemical reasoning, one can often build a model system of a full molecule that will be easier to treat computationally but can also represent the essential underlying chemistry and physics with a high degree of accuracy.

To detail the photochemistry of such transition metal complexes as described in this thesis requires an array of methods to treat different aspects, e.g. spectroscopy versus reactive photochemistry. Each of these methods has practical and technical limitations but when used in conjunction and applied appropriately can give enormous insight into the underlying molecular processes. Such an understanding is vital as light induced chemistry in transition metal containing systems is of relevance in a wide range of modern science and technology.